Isotopic effect in B-like and Be-like argon ions

Dissertation
zur Erlangung des Doktorgrades
der Naturwissenschaften

vorgelegt beim Fachbereich Physik
der Johann Wolfgang Goethe - Universität
in Frankfurt am Main

von
Rosario Soria Orts
aus Valencia

Institut für Kernphysik Frankfurt
Frankfurt am Main, 2005
(DF1)

vom Fachbereich Physik der
Johann Wolfgang Goethe - Universität als Dissertation angenommen.

Dekan: Prof. Dr. Wolf Assmus
1. Gutachter: Prof. Dr. Reinhard Dörner
2. Gutachter: PD. Dr. José Ramón Crespo López-Urrutia
Datum der Disputation:

Al fin y al cabo, mañana será otro día.

Zusammenfassung:

In der vorliegenden Arbeit wurde die Elektronenstrahlionenfalle (electron beam ion trap, EBIT) des Heidelberger Max-Planck-Instituts für Kernphysik dazu benutzt, hochgeladene Argonionen zu erzeugen und zu speichern. Relativistische Effekte in Vielelektronensystemen wurden mithilfe der verbotener magnetischen Dipolübergänge (M1) untersucht. Die Bestimmung der quantenelektrodynamischen (QED) Beiträge zur Übergangsenergie ist nach wie vor eine anspruchsvolle Problemstellung. Ein interessanter Beitrag ist der sogenannte Isotopeneffekt, der von endlicher Kernmasse und dem Kernvolumen verschiedener Isotope herrührt. Der durch die endliche Kernmasse entstehende Effekt (Rückstoß-Effekt) kann in den normalen Massen-Effekt (normal mass shift, NMS), welcher durch die reduzierte Masse beschrieben werden kann, und den spezifischen Massen-Effekt (specific mass shift, SMS), auch Massen-Polarisation genannt, unterteilt werden. Die Beiträge, die durch Elektronen-Korrelation und QED entstehen, sind unabhängig vom Isotop. Daher ermöglicht der direkte Vergleich der Übergangsenergien für zwei verschiedene Isotope, die durch Volumen- und Massenkorrekturen entstehenden Unterschiede trotz ihrer sehr kleinen Beiträge äußerst präzise zu bestimmen. Erst vor kurzer Zeit wurden relativistische Beiträge in der Berechnung in der Isotopeneffekte berücksichtigt [TSC 03], welche überraschenderweise von ähnlicher GröSSenordnung wie die nichtrelativistischen Beiträge sind. Dies und die experimentelle Präzision, die in der Bestimmung der Energieen von Übergängen im sichtbaren Bereich in Vier- und Fünfelektronensystemen erreicht wurde [DCD 03] motivierten uns dazu, zum ersten mal den relativistischen RückstoSS-Effekt in hochgeladenen Ionen (highly charged ions, HCI) zu vermessen.

Kapitel 1

Dieses Kapitel gibt einen Überblick über die theoretischen Methoden, die zur Berechnung der energetischen Zustände in Ein- und Vielelektronensystemen benutzt werden, insbesondere über jene, die auf die Übergänge, die in dieser Arbeit untersucht wurden, anwendbar sind. Der Ausgangspunkt ist die relativistische Dirac Theorie, die den Elektronenspin sowie die Aufspaltung zwischen den Zuständen $^2P_{1/2}$ und $^2P_{3/2}$, welche im Spektrum des Wasserstoffatoms auftritt, beschreibt. Es folgt die Erklärung der Wechselwirkung zwischen dem gebundenen Elektron und dem quantisierten elektromagnetischen Strahlungsfeld (QED oder Strahlungskorrekturen), durch welche die Entartung der Zustände $^2P_{1/2}$ und $^2S_{1/2}$ aufgehoben wird.

Die Schrödinger- und Diracgleichungen können ausschliesslich für das Wasserstoffatom sowie wasserstoffartige Ionen analytisch gelöst werden. Im Falle von Atomen oder Ionen mit zwei oder mehr Elektronen ist dies nicht möglich, da die Coulomb-Wechselwirkung zwischen den Elektronen im Hamilton-Operator nur als Störung berücksichtigt werden kann. Die mathematischen Schwierigkeiten, die bei der genauen Beschreibung von Vielelektronensystemen unter Berücksichtigung relativistischer Effekte bestehen, werden aufgezeigt. Die hier beschriebenen Methoden, die zur Berechnung relativistischer Vielelektronensysteme und deren Zustandsenergien genutzt werden, können in zwei Klassen aufgeteilt werden [Kim97]. In der einen Klasse wird relativistischen Effekten zum Teil in der Evaluation der Wellenfunktionen Rechnung getragen. Diese basieren auf einer Verallgemeinerung der Dirac Gleichung eines Elektrons in einem Zentralfeld auf den Viel-Elektronen Fall, wie es z.B. in der relativistischen Hartee-Fock Methode gemacht wird. Auch die $1/Z$-Reihenentwicklung, in der Wasserstoff-Wellenfunktionen benutzt werden, wird dieser Kategorie zugewiesen. Die andere Klasse beinhaltet alle Ansätze, die auf nichtrelativistischen Wellenfunktionen aufbauen, und die relativistische Effekte über Störungsterme im Hamilton-Operator berücksichtigen.

Im nächsten Abschnitt wird eine Beschreibung strahlender Übergänge und ihrer *Auswahlregeln* gegeben. Diese Regeln unterteilen die Übergänge in *erlaubte* und *verbotene* Übergänge. Dabei wird gezeigt, daßdie Raten der verbotenen magnetischen Dipolübergänge (M1) eine stärkere Abhängigkeit von der Kernladungszahl Z aufweisen ($\approx Z^{10}$) als die Raten der erlaubten elektrischen Dipolübergänge ($\approx Z^4$).

Da die Ionen in dem in dieser Arbeit beschriebenen Experiment im starken Magnetfeld der EBIT gespeichert werden, müssen die Auswirkungen des externen Feldes, das zum sogenannten Zeeman-Effekt führt, berücksichtigt werden. Der Einfluß des Magnetfeldes auf die Ionen wird im nächste Abschnitt erläutert. Über eine Beschreibung dieses Effekts durch die LS-Kopplungsnäherung wird gezeigt, daß Emissionseigenschaften wie die Polarisation der ausgesandten Strahlung von den Auswahlregeln und dem Winkel zur Quantisierungsachse, unter dem die Strahlung detektiert wird, abhängen.

Am Ende des Kapitels wird auf die Wechselwirkungen eingegangen, die zu Isotopeneffekten führen, wobei besonderes Augenmerk auf die Auswirkungen der endlichen Kernmasse und des Kernvolumens gelegt werden. Zunächst werden die massenabhängigen Beiträge in den normalen Masseneffekt (NMS) und den spezifischen Masseneffekt (SMS) unterteilt. Dabei wird gezeigt, daß bei Einelektronensystemen die NMS Korrektur der Zustandsenergie durch das Ersetzen der Elektronenmasse durch die reduzierte Masse des Systems beschrieben wird. Bei Vielelektronensystemen muß die Elektronen-Korrelation berücksichtigt werden. Die theoretische

Methode, welche zur Berechnung der verschiedenen relativistischen Beiträge zum Masseneffekt (RNMS und RSMS) genutzt wird, wird erläutert. Der volumenabhängige Anteil des Isotopeneffekts hängt von der radialen Ladungsverteilung im genutzten Kernmodell ab und ist ausschließlich für schwere Ionen von Bedeutung.

Kapitel 2

Relativistische und QED Effekte treten verstärkt in Ionen mit hoher Kernladungszahl Z auf; die wesentliche Schwierigkeit bei der experimentellen Untersuchung dieser Effekte besteht darin, genügend HCI für ein Experiment bereitstellen zu können. In diesem Kapitel wird detailliert auf die EBIT, mit der in dieser Arbeit die HCI erzeugt und gespeichert wurden, eingegangen, und ein Vergleich mit Speicherringen und Tokamaks gezogen. Aufgrund ihrer vergleichsweise geringen Komplexität, Größe und Betriebskosten, ist die EBIT mittlerweile eines der wichtigsten Geräte zur Untersuchung hochgeladener Ionen.

Die Beschreibungen in den nachfolgenden Abschnitten widmen sich den verschiedenen Teilen der EBIT: der Elektronenkanone, den Fallenelektroden, dem Magneten sowie dem Elektronenkollektor. Dabei wird erläutert wie hochgeladene Ionen mit einer EBIT erzeugt und gespeichert werden, und wie sie in der Falle untersucht oder für externe Anwendungen extrahiert werden können. Einige wesentlichen Eigenschaften der Heidelberger EBIT werden im Vergleich mit anderen EBITs hervorgehoben.

Es folgt eine kurze Beschreibung der Elektronenstrahleigenschaften, nämlich des Elektronenstrahlradius sowie der radialen und axialen Raumladung, die durch seine Ladungsdichte erzeugt wird. Es wird gezeigt, daß diese Eigenschaften eine wesentliche Rolle bei der Bestimmung der Linienbreiten der von den gespeicherten Ionen ausgesandten Strahlung spielt. Die Temperatur der Ionen führt zur Dopplerverbreiterung der zu beobachtenden Linien. Im Allgemeinen verdeckt diese Verbreiterung (in Kombination mit der begrenzten Auflösung des genutzten Spektrometers) die natürliche Linienbreite vollständig. Nach einer Beschreibung der Heiz- und Kühlmechanismen, die auf die gespeicherten Ionen wirken wird gezeigt, wie die Temperatur der Ionen in unserem Experiment durch evaporatives Kühlen und Absenkung des axialen Fallenpotentials von 30 eV auf 6 eV reduziert werden konnte. Aufgrund der niedrigen Ionentemperatur und der damit einhergehenden kleineren Dopplerverbreiterung, konnte die Zeeman-Aufspaltung der emittierten Linien aufgelöst werden.

Kapitel 3

Aufgrund der kleinen Zahl gespeicherter Ionen, wird für spektroskopische Untersuchungen an einer EBIT empfindliche Messtechnik benötigt. In diesem Kapitel wird eine detaillierte Beschreibung des optischen Aufbaus und des Spektrometers, das im vorgestellten Experiment genutzt wurde, gegeben.

Der optische Aufbau besteht aus einem Spektrometer, das über verschiedene Linsen und Spiegel an die EBIT gekoppelt wird (Abb. 1). Die ersten beiden Linsen (L1 und L2) sind innerhalb des Vakuums der EBIT angebracht, um eine Abbildung der gespeicherten Ionen ausserhalb der EBIT zu erhalten. Da die Ionenwolke in der EBIT horizontal liegt, wird eine Optik bestehend aus drei Spiegeln (M1, M2 und M3) sowie zwei Linsen (L3 und L4) dazu genutzt ihr Bild zu drehen und auf den vertikal ausgerichteten Eingangsspalt des Spektrometers zu fokussieren. Dieser Aufbau ist fest auf demselben Tisch wie das Spektrometer montiert um jegliche relativen Verschiebungen zu unterdrücken. Das hier eingesetzte Czerny-Turner Spektrometer (CT) ist mit einer kryogenisch gekühlten CCD (charge coupled device) Kamera ausgestattet.

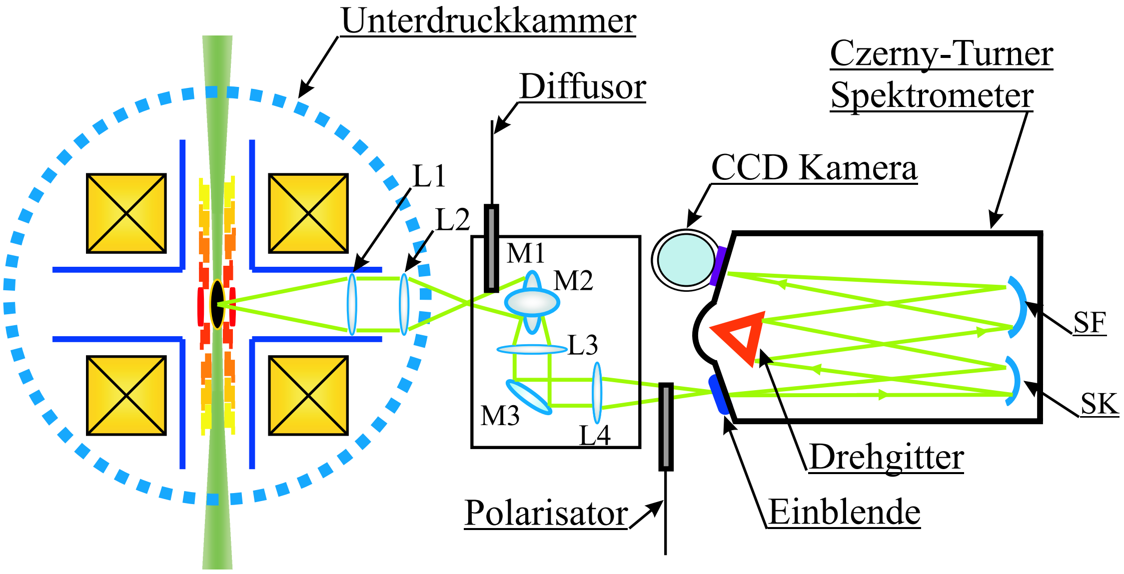

Figure 1: Skizze des in dieser Arbeit benutzten experimentellen Aufbaus. Zwei Quartzlinsen (L1, L2) sind innerhalb der EBIT Vakuumkammer angebracht. Ausserhalb der EBIT wird das Licht der Ionen durch eine Optik mit den Spiegeln M1, M2 und M3 sowie den Linsen L3 und L4 in das Czerny-Turner Spektrometer geführt.

Die exakte Ausrichtung der Optik und des Spektrometers an das EBIT Vakuumfenster wurde mithilfe eines Helium-Neon Lasers sichergestellt. Das Spektrometer wurde nach seiner lateralen und axialen Ausrichtung fixiert, und es wird lediglich eine Linse dazu genutzt, das Bild der Ionenwolke auf die CCD Kamera zu fokussieren. Die Feinjustage wird mit Linse L4 und Spiegels MC vorgenommen, die auf Schienen angebracht sind und mit Mikrometerschrauben eingestellt werden können. Die Datenaufnahme und die Spektrometerfunktionen werden mit einer Spezialsoftware (Jobin-Yvon Spectra-Max für Windows, Version 3.0) gesteuert.

Die mit der CCD Kamera aufgenommenen Spektren werden mithilfe von Referenzlinien kalibriert. Zu diesem Zweck wird eine Hohlkathodenlampe, die schmale Referenzlinien emittiert, benutzt. Das Licht dieser Lampe wird durch eine Faser in die Optik geführt und folgt dem gleichen Strahlengang wie das Licht der EBIT-Ionen, nachdem es auf einem Diffusor gestreut wird. Kalibrationsspektren dieser Lampe werden vor und nach jeder Messung aufgenommen. Dies erlaubt die Überprüfung der Stabilität der experimentellen Bedingungen. Zudem wird die Messung häufig wiederholt, wobei die Position des Gitters im Spektrometer von Aufnahme zu Aufnahme in kleinen Schritten modifiziert wird, um systematische Unsicherheiten, die durch das Sampling der schmalen Linien auf wenigen Pixeln der CCD entstehen könnten, zu vermeiden. Inklusive der Kalibarationsaufnahmen betrug die Aufnahmezeit der Spektren, die in dieser Arbeit untersucht wurden, 30 Minuten (Ar^{13+}) bzw. 60 Minuten (Ar^{14+}).

Die Emissionslinien der Lampe wurden zusätzlich dazu benutzt, die durch eine gaussförmige Apparatefunktion charakterisierte Spektrometerauflösung zu bestimmen. Mehr als zehn Kalibrationslinien wurden in jedem ($\mathrm{Ar}^{13+,14+}$) Spektrum dazu genutzt, die Dispersionsfunktion zu bestimmen: die Literaturwerte der Wellenlängen dieser Referenzlinien (in nm) werden gegen die Position der Linien (in Pixeln) aufgetragen und ein Polynom zweiter Ordnung, das diese Funktion am besten beschreibt, wird an diese Datenpunkte angepasst.

Durch die für EBIT-Bedingungen untypisch niedrigen erreichten Ionentemperaturen sowie die sorgfältige Kalibration der Spektren und die vielen aufgenommenen Datenpunkte (30 bis 40 Spektren) wurde eine sehr hohe Genauigkeit mit Unsicherheiten von weniger als 1 ppm (parts per million, hier im Bereich von 10^{-4} nm) erreicht.

Kapitel 4

In diesem letzten Kapitel werden die experimentellen Ergebnisse dieser Arbeit zum Isotopeneffekt in $^{40}\mathrm{Ar}$ und $^{36}\mathrm{Ar}$ zusammen mit der Bestimmung der Temperatur der gespeicherten Ionen, der g_J-Faktor Bestimmung und den Übergangsenergien in Be-und B-artigen Argon Ionen vorgestellt.

Aufgrund der niedrigen Temperatur der Ionen war es möglich, die Zeeman Aufspaltung der Übergänge zwischen den Zuständen $^2P_{1/2}$ und $^2P_{3/2}$ im Grundzustand $2s^22p$ in B-artigem Ar^{13+} aufzulösen. Für diese Übergänge werden sechs Komponenten erwartet und, wie in Abb. 2 gezeigt, beobachtet. Diese Komponenten sind entweder parallel (π-Komponenten) oder senkrecht (σ-Komponenten) bezüglich des Magnetfelds der EBIT unter transversaler Blickrichtung polarisiert. Aus der beobachteten Aufspaltung dieser Komponenten konnte der g_J-Faktor der oberen und unteren Feinstrukturzustände bestimmt werden. Die experimentell ermittelten Werte sind in Übereinstimmung mit "large scale configuration interaction“ (CI) Dirac-Fock-Sturm Vorhersagen. Zudem war der genutzte experimentelle Aufbau dazu geeignet, die Ionentemperatur zu vermessen. Die gefundene Temperatur beträgt lediglich 6 eV bei einem Elektronenstrom von 20 mA, einer Elektronenstrahlenergie von 865 eV und einem magnetischen Feld von 6.82 Tesla. Unter sonst üblichen Betriebsbedingungen der EBIT ist die Ionentemperatur zwei Größenordnungen höher.

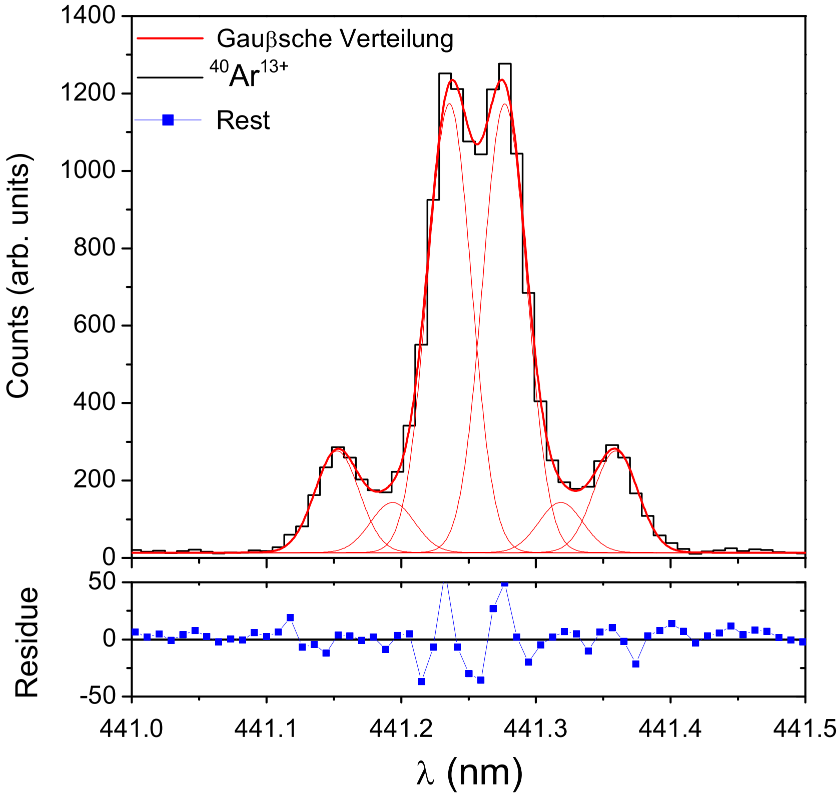

Figure 2: Ein typisches Ar^{13+} Spektrum des $^2P_{1/2} - ^2P_{3/2}$ übergangs bei E_e=875 eV, I_e=50 mA und 6.82 T magnetischer Feldstärke. Der untere Graph zeigt die Residuen des Fits.

Es ist prinzipiell möglich, daß das starke Magnetfeld in der EBIT den Schwerpunkt der beobachteten Linien verschiebt. Die mögliche Verschiebung, $\Delta E_{J,M_J}(B)$ wurde mit der zuvor genannten Methode berechnet. Der berechnete Wert ergibt vernachlässigbare Verschiebungen von -0.00000324 nm für σ- und $\pi_{1/2}$-Komponenten bzw. -0.00000162 nm für $\pi_{3/2}$-Komponenten bei einer Erhöhung der magnetischen Feldstärke von 5 T auf 8 T, da die Linien-Aufspaltung nahezu symmetrisch um den Linienschwerpunkt auftritt. Es wird daher keine bemerkbare Abhängigkeit von der magnetischen Feldstärke innerhalb der angegebenen Unsicherheit erwartet. Als Linienschwerpunkt der Zeeman-Komponenten wurde ein Wert von 441.2556(1) nm ermittelt. Dieses Ergebnis weicht leicht von einem vormals von Draganić [DCD 03] gefundenen Wert von 441.2559(1) nm ab. Die hier gefundene Wellenlänge des Übergangs in Be-artigem Argon von 594.3879(2) nm stimmt gut mit Draganićs Wert von 594.3880(3) nm überein.

Reine ^{36}Ar und ^{40}Ar Proben wurden genutzt, um den Isotopeneffekt zu vermessen. Zunächst wurde ^{36}Ar Gas in die Falle injiziert. Nachdem die Messung an diesem Isotop abgeschlossen war wurde, das Gasinjektorsystem ausgepumpt, um eine mögliche isotopische Kontamination zu vermeiden, bevor zu ^{40}Ar gewechselt wurde. Weiterhin wurden die Ionen aus der Falle extrahiert und ihre q/m Verteilung mithilfe eines Analysemagneten vermessen. Dabei wurde bestätigt, daß keine ^{36}Ar Rückstände in der Falle waren, bevor die Injektion von ^{40}Ar in die Falle begonnen wurde.

Die Ergebnisse sind in Tabelle 1 zusammengefasst und werden mit theoretischen CI Dirac-Fock (DF) Berechnungen verglichen. Der relativistische Rückstoß-Effekt ist bei den Übergängen $^2P_{3/2} -^2 P_{1/2}$ in Ar^{13+} und $^3P_1 -^3 P_2$ in Ar^{14+} deutlich ersichtlich (Tabelle 2). In Tabelle 2 sind weiterhin die Beiträge des NMS und SMS sowie ihrer relativistischen Korrekturen, RNMS bzw. RSMS, angegeben. Aus dieser Aufstellung wird deutlich, daßdie Beiträge der RNMS und RSMS, die bisher in Berechnungen vernachlässigt wurden, von ausschlaggebender Bedeutung sind. Die in dieser Arbeit experimentell ermittelten Werte des Isotopeneffekts bestätigen die neuesten Berechnungen des relativistischen Kernrückstoßeffekts, und zeigt erstmalig die erheblichen Unzulänglichkeiten früherer theoretischer Vorhersagen auf.

Table 1: Übergangsenergien in Ar$^{13+,14+}$ und Isotopeneffekte in ^{40}Ar/^{36}Ar (in nm). Die Isotopeneffekte sind nicht von den großen Unsicherheiten in der Wellenlängenberechnung beeinflußt, da sie aus der Differenz der gemessenen Wellenlängen erhalten werden

	Wellenlängen		***Isotopeneffekt***	
Ion	***Theorie***	***Experiment***	***Theorie***	***Experiment***
Ar^{13+}	441.16(27)	441.2556(1)	0.00126	0.0012(1)*
				0.00125(7)**
Ar^{14+}	594.24(30)	594.3879(2)	0.00136	0.0012(1)

* π - Komponenten. ** σ - Komponenten

Table 2: Berechnete Werte der einzelnen Beiträge zum Isotopeneffekt in ^{40}Ar/^{36}Ar der verbotenen übergänge in Ar^{13+} und Ar^{14+}. Die *rms* Kernladungsradien, die in den Berechnungen benutzt wurden, sind $<r^2>^{1/2} = 3.390$ fm und 3.427 fm für ^{36}Ar bzw. ^{40}Ar. NMS: Normaler Masseneffekt, berechnet mit Dirac Wellenfunktionen; SMS: Spezifischer Masseneffekt, berechnet mit Dirac Wellenfunktionen; RNMS: relativistischer Operator Korrektur zum NMS; RSMS: relativistischer Operator Korrektur zum SMS. FS: Feldeffekt. Die Angaben sind in cm^{-1} angegeben

Ion	***NMS***	***SMS***	***RNMS***	***RSMS***	***FS***	***Total***
Ar^{13+}	0.1053	-0.0742	-0.0822	0.1151	-0.0005	0.0635
Ar^{14+}	0.0797	-0.0698	-0.0627	0.0887	-0.0001	0.0358

Abstract:

In the present work, the Heidelberg electron beam ion trap (EBIT) at the Max-Planck-Institute für Kernphysik (MPIK) has been used to produce, trap highly charged argon ions and study their magnetic dipole (M1) forbidden transitions. These transitions are of relativistic origin and, hence, provide unique possibilities to perform precise studies of relativistic effects in many electron systems. In this way, the transitions energies of the $1s^2 2s^2 2p$ for the $^2P_{3/2}$ - $^2P_{1/2}$ transition in Ar^{13+} and the $1s^2 2s2p$ for the $^3P_1$ - $^3P_2$ transition in Ar^{14+}, for ^{36}Ar and ^{40}Ar isotopes were compared.

The observed isotopic effect has confirmed the relativistic nuclear recoil effect corrections due to the finite nuclear mass in a recent calculation made by Tupitsyn [TSC 03], in which major inconsistencies of earlier theoretical methods have been corrected for the first time. The finite mass, or recoil effect, composed of the normal mass shift (NMS), and the specific mass shift (SMS) were corrected for relativistic contributions, RNMS and RSMS. The present experimental results have shown that the recoil effects on the Breit level are indeed very important, as well as the effects of the correlated relativistic dynamics in a many electron ion.

Contents

Introduction

There is abundant evidence indicating the importance of relativistic effects in the atomic structure. The fine structure of hydrogen was the first case in which the observed spectrum was in contradiction with Schrödinger's theory; only the relativistic electron theory introduced by Dirac was able to explain the splitting observed in the spectra between the ${}^2P_{1/2}$ and ${}^2P_{3/2}$ levels. However, it was not capable of describing the non-degeneracy of the ${}^2P_{1/2}$ and ${}^2S_{1/2}$ levels. This failure was solved by introducing the interaction between the bound electron and the quantized electromagnetic radiation field, the so-called quantum electrodynamics (QED) corrections into the description of the system. Recent calculations of the isotope shift in highly charged ions (HCI) have shown, once again, the necessity and mathematical difficulties of taking accurately relativistic effects into account [TSC 03]. This shift is the effect on the electronic binding energies due to the finite mass and volume of the nucleus. Where the finite mass, also know as recoil effect, is composed by the normal mass shift (NMS), *i.e.*, the reduced mass, and the specific mass shift (SMS) or mass polarization. In order to have high precision calculations of the energy levels in high-Z few-electron atoms, relativistic nuclear recoil corrections must be included. This crucial assessment, together with the also recently achieved precision in the transition energy determination for four- and five-electron systems in argon ions [DCD 03] gave the motivation for our work to measure, for the first time, the relativistic recoil effect in HCI.

The first observations of HCI, which by then were not understood, date from the XIXth century and the beginning of the XXth century from spectroscopic investigation of the solar corona. The rareness of total solar eclipses, their short durations and the distances one has to travel to observe them made the investigation of the line spectrum of the solar corona very difficult. This problem was overcome by the development of coronagraphs providing continuous observation of the sun's corona at practically all eclipse expeditions. The first photograph of the corona spectrum without an eclipse was taken on 1930 and the wavelength of one of the first and most prominent lines, the green line of Fe XIV at 5303 Å, was already determined with 0.02 Å accuracy [Lyo39]. Many emission lines were identified later as transitions from energetically low-lying metastable levels normally forbidden to decay, and therefore able to appear only in sources of very low density. Many of them showed the particularity to be caused by emission from high ionization stages of the coronal atoms. Detailed observations of a number of features of these emission lines such as their energy (wavelength), intensity (strength), and profile (spectral shape) have led to an expanded understanding of atomic physics.

An increased curiosity on this type of transitions followed the development of laboratory devices capable of producing hot plasmas, where production and excitation of highly ionized atoms takes place. The main motivation for these studies was to control thermonuclear fusion for the energy production. In this aim, the first achievement, using the so-called *theta-pinch* effect, was made with the Scylla I machine in 1958 [JLQ 60]. It consisted of a cylindrical discharge tube enclosed by a single-turn magnet coil, in which a short discharge current was induced. The magnetic field generated squeezes the plasma inward into a small radius thus heating it [FJW61, SBH 63]. In the following years, a different approach to fusion research was the use of powerful lasers to produce hot plasmas. Laser beams can be amplified and focused to concentrate, temporally as well as spatially, their energy onto very sharp target spots to produce very high temperature plasmas [FGP 66, Faw70]. Then, a first highly developed, large-scale fusion device realized in Princeton was the Tokamak [Hin76]. Tokamaks use a combination of an external toroidal magnetic field and an internal magnetic field generated by the induced plasma current to confine and heat the plasma with energetic pulsed discharges. Their large dimensions cause a relative reduction of radiation losses and facilitate the achievement of very high temperatures and long confinement times, thus making them the currently most advanced approach to controlled thermonuclear fusion. Tokamaks can be used as photon sources to study the radiation emitted by HCI. However, the plasma parameters inside such machines are not constant, such that spectroscopy nowadays's is mostly used as an important tool to diagnose the fusion plasma, in next generation devices, like stellarators JET or the upcoming international ITER machine, just recently agreed upon to be realized in Cadarache, France. Therefore, for precise plasma diagnostics one either has to rely on simulations or on other laboratory data obtained under well-controlled conditions to analyze the experimental results.

Compared with such high-power systems, simpler and more compact ion sources were developed for small laboratories, some of them even allowing continuous operation. One widely used device is the electron cyclotron resonance ion source (ECRIS) [Xie98]. In a ECRIS, plasma electrons are heated in the presence of a magnetic field by means of microwave radiation at the electron cyclotron resonance frequency. The plasma electrons are generated initially by field and thermal emission, and their density grows rapidly due to secondary electron emission from the walls, and through the ionization of the working gas at pressures around 10^{-6} mbar. Due to the absence of a cathode, these devices are robust and long lived. However, they have some critical problems, from the spectroscopic (optical) point of view, due to so-called *satellite electrons*. These electrons are the result of the strong excitation rate, which can produce multiply-excited ions with a high probability. The presence of satellite electrons changes the energies of the electronic transitions and also their probabilities. Although, ions in charge states as high as Ar^{18+} or U^{48+} can be produced, these sources can generate only intermediate plasma temperatures and, thus, produce mostly ions in low ionization stages. To produce high ionization stages one can also make use of high energy ion beams. Since early on, at facilities such as linear accelerators, cyclotrons or synchrotrons, a technique called *beam-foil spectroscopy* (BFS) was applied [LWW80] until the present day, where fast ions are shot through a thin foil leading to further ionization due to stripping, as well as to excitation of the ions. Downstream from the foil, spectroscopic observations are possible. This method is particularly characterized by a very good time resolution which permits lifetime measurements (transition rates) of ionic excited states. In addition, often excellent accuracy in the energy determination of electronic transitions can be achieved, again, however, mostly influences by satellite electrons [ZSW 04].

A major step forward in accelerator based spectroscopy was marked by the realisation of heavy-ion cooler storage rings at the end of the 1980th to early 1990th [BGH 98, GvR03]. Here, highly charged ions, produced earlier by slipping in a foil, an stored, cooled by stochastic, laser or electron cooling methods and usually excited states are prepared in collisions with atoms of internal gas-jet targets or with electrons in a cooler. Thus, with this technology, the most precise spectroscopic data on Li- and He-like uranium [BSB 02, MSB 01] has been achieved, laser spectroscopy on hyper-fine transitions was performed [KHJ 92] for the first time and highly accurated measurements on dielectronic recombination transition were performed [GGR 03].

Mostly common to all these techniques, fusion devices, accelerators and storage rings, is that they are large and expensive to run. Trying to minimize the complexity, dimension and running costs a new device, the electron beam ion trap (EBIT), was developed in the 1980's, based upon the principles of the electron beam ion source (EBIS) [DDD 02]. Within the last 20 years it has became the main alternative tool for studying HCI [MLK 88]. In an EBIT, highly charged ions are produced and trapped by means of a high current density electron beam which is compressed with a strong magnetic field. The trapped ions can be observed or they can be extracted for external applications. Similarly to the conditions present in the solar atmosphere, in an EBIT the excitation is primarily induced by electron collisions.

In the present work, the Heidelberg EBIT has been used to produce, trap and study magnetic dipole (M1) forbidden transitions in highly charged argon ions. Over the last 50 years, these forbidden transitions had become of great interest due to their relativistic origin and hence, the unique possibility to perform precise studies of relativistic effects in one- to many-body electron systems. One intriguing contribution is the so-called isotopic effect caused by the finite nuclear mass of different isotopes. Not only the modified mass that affects the system's kinematics, but also the changes induced in the nuclear charge distribution, lead to small variations in the transition energies. By measuring the difference in the transition energy between two isotopes, the largest error contributions in comparison with theory arising from the uncertainty in the calculation of the corrections due to interelectronic correlation and the QED contributions are cancelled out because they are practically the same for the different isotopes. Hence, the remaining differences from the size and mass corrections can be extracted very precisely despite of their very small magnitude.

Traditionally, measurements of the optical isotope shifts in atomic spectra have been systematically carried out to determine changes in the mean-square nuclear charge radii $\langle r^2 \rangle$, among other nuclear properties which affect structures found in the atomic spectra. More recently, the relevance of this field has been emphasized by new applications. For instance, isotopic shift calculations in atoms and ions with one valence electron above closed shells could help to explain the spectral line shifts observed in quasar absorption spectra that had suggested a variation in the fine-structure constant [BDF03]. Laser spectroscopy has been used to determine the change distribution in the halo nuclei, $^{8}\mathrm{Li}^{+}$ and $^{9}\mathrm{Li}^{+}$ [END 04]. However, only few spectroscopic measurements with HCI have been reported with an accuracy sufficient for the resolution of isotopic shifts. The study of these effects in HCI has the potential advantage of increased sensitivity to nuclear size and relativistic effects. This enhanced sensitivity is a consequence of the stronger overlap between the electronic and the nuclear wave function, of the higher expectation value of the electron energy, and last but not least, of the simpler electronic structure of few-electron ions. This last reason is indeed very important, since theoretical uncertainties in the treatment of the electron correlations are still the prominent error source in the analysis of experiments with atoms aiming at determining physical properties of the nucleus or its constituents, as the case in parity-non-conservation experiments [BW99, BB97], among many others.

As we will see throughout this work, the combination of an EBIT, providing a stable population of trapped HCI, with accurate calibration techniques carried out in this work has allowed us to experimentally determine such isotope shifts with very high accuracy. The results confirm newest calculations of the relativistic nuclear recoil effect, in which major inconsistencies of earlier theoretical methods had been addressed and corrected for the first time.

The experimental study of the isotopic shift in B- and Be-like argon ions presented here is structured as follows. In the first chapter, a brief overview of the different theoretical descriptions which have evolved over time from the Sommerfeld quantum theory, through the relativistic formulation made by Dirac of the atomic structure to modern QED corrections is provided. The case of hydrogen is treated and extended to many-body systems, giving an overall description of the different multi-configuration methods used to study highly ionized atomic systems. It also includes an explanation of the particular theoretical method used for calculating the isotopic shift in the systems under study. In the following chapter, after a brief historical introduction to the EBIT, a detailed description of the one operational in Heidelberg is made. There, the specific parameters, for the present experiment and its particular characteristics are explained. The third chapter is dedicated to the experimental setup used for the spectroscopic observation of the emitted visible lines, the data acquisition process, as well as the data analysis and treatment of the errors. In the last chapter, after presenting results concerning the transition energies and the temperature of the trapped ions, the experimental results obtained for the isotopic shift are presented and discussed in comparison with the theoretical predictions.

Chapter 1

Theory of the atomic structure

The starting point for modern atomic structure theory was the Bohr model of the hydrogen atom, based on the Rutherford atom model and incorporating the ideas of Planck. Its main points are the concept of discrete stationary states of a given energy, and the emission and absorption of photons of frequency $\nu_{21} = E_2 - E_1/h$ in radiative transitions between states of energies E_1 and E_2, with h being Planck's constant. The development of these models layed the foundations of quantum mechanics, which successfully described the hydrogenic spectrum.

The fundamental postulates of quantum mechanics were made by Schrödinger. His wave equation for the motion of a particle in a potential $V(x, y, z)$ explained the existence of discrete atomic energy levels. But this theory could not account for the fine structure observed in some experimental spectra as all levels with the same principal quantum number n are degenerate in Schrödinger's theory. Modern fully quantum mechanics theory was born as the spin concept was introduced by Dirac in his relativistic electron theory. The fine structure of the simplest possible atomic system, hydrogen, was well described by the Dirac wave equation. However, an experiment carried out by Lamb and Retherford showed that the $2\,^2s_{1/2}$ level did not have exactly the same energy as the $2\,^2p_{1/2}$ level, in contradiction with the theoretical prediction. A qualitative explanation based on the interaction between the bound electron and the electromagnetic field was given by Welton. This resulted later in the formulation of a relativistic quantum field theory of the electromagnetic interaction, called quantum electrodynamics (QED). It describes all phenomena exhibited by charged particles emitting or absorbing photons and interacting by photon exchange. This theory includes classical electrodynamics in the limit of many photons and strong fields, and also explains quantum phenomena relevant to the atomic structure. QED is part of a wider theoretical framework called the Standard Model, which combines two foundations of particle physics: electroweak theory, describing the electromagnetic and weak interactions and quantum chromodynamics, the theory of the strong interaction.

With QED, extremely accurate explanations of physical observables like the anomalous magnetic moment of the electron and muon and the hydrogen Lamb shift could be made. This is the first quantum field theory, in which the difficulties of building a consistent fully quantal description of fields, creation and annihilation of quantum particles are solved satisfactorily. In general, it is difficult to perform experiments that test with sufficient accuracy the predictions of this theory in atoms or ions because the average energies of the atomic electrons are generally many orders of magnitude larger than the QED effects. Moreover, in atomic systems - with exception of hydrogen - it is generally impossible to calculate the QED independent parts of the electronic structure with enough precision to distinguish quantum electrodynamic effects. However, in systems with high nuclear charge Z, relativistic effects and QED are enhanced, since their contributions scale with high powers of Z. Hence, highly charged ions (HCI) make feasible to perform experiments with a precision comparable to or even better than that of calculations.

In this chapter an overview of theoretical methods used to calculate the energy levels in one- as well as many-electron systems will be presented.

1.1 Hydrogen-like systems

The hydrogen atom and its spectrum are of special interest in atomic theory because only for them the Schrödinger and Dirac equations can be solved analytically. Thus, the so-called hydrogen-like approximations are widely used.

The energy levels of the hydrogen atom exhibit the well-known fine structure splitting which is partly due to the relativistic mass increase of the electron, partly due to its spin and to its delocalisation accounted for in the so-called Darwin term. An effect of relativity on the atomic structure was already predicted by calculations evaluating relativistic corrections to the Schrödinger equation for particles without spin. Since the spin itself is of relativistic nature, the Dirac wave equation forms the basis of a fully relativistic theory.

1.1.1 Fine structure in $l \cdot s$ coupling

For the hydrogen atom and hydrogen-like ions with low Z, the relativistic effects are relatively small and can be taken appropriately into account even by using perturbation theory and applying it to the non-relativistic Schrödinger equation. These effects are treated in terms of the velocity-dependent electron mass, the electron spin angular momentum $\vec{s}$, and it's position uncertainty, called the Darwin term. The perturbation due to the relativistic mass increase effect (see Eq. (1.9)) results in a level shift of

$$\Delta E'_{nl} = -c^2 \frac{\alpha^4 Z^4}{2n^4} \left(\frac{1}{l+1/2} - \frac{3}{4n} \right) \quad , \tag{1.1}$$

where l is the orbital angular momentum, n is the principal quantum number. From now on, we adopt the use of atomic units (a.u.) for simplicity (m_o, e, $\hbar \equiv 1$).

The magnetic moment of the electron $\vec{\mu} = \mu_B \cdot \vec{s}$, connected with the electron spin $\vec{s}$, leads to an additional interaction between the electron and the nucleus, namely $\vec{\mu} \cdot \vec{B} = \mu_B \cdot \vec{s} \cdot \vec{B}$. Here, $\vec{B}$ is the magnetic field associated with the electron moving in the electric field $\vec{E}$, and can be described in terms of the angular momentum $\vec{l}$. This results in the so-called *spin-orbit interaction.*

The spin-orbit interaction depends on the mutual orientation of the angular momentum $\vec{l}$ and $\vec{s}$, *i.e.*, on the value of the total angular momentum, $\vec{j} = \vec{l} + \vec{s}$. For a given value of j, the z component m_j of the total angular momentum can take $(2j+1)$ different values j, $j-1$, ..., -j . Therefore, the level nl_j has $2j+1$ magnetic substates, differing in its quantum number m_j. The quantity $2j+1$ is called the statistical weight of the j level.

The total angular momentum of any isolated system is conserved. Therefore, the state of an atom is characterized by the value of the total angular momentum j, even in the case when the orbital and spin angular momentum are not separately conserved. Since $\vec{l} \cdot \vec{s} = (\vec{j}^2 - \vec{l}^2 - \vec{s}^2)/2$ and its mean value equal to [$j(j$+1) - $l(l$+1) - $s(s$+1)]/2, the correction to the energy due to the spin-orbit interaction is

$$\begin{aligned} \Delta E''_{nlj} &= -c^2 \frac{\alpha^4 Z^4}{4n^3} \frac{j(j+1) - l(l+1) - s(s+1)}{l(l+1)(l+1/2)} && (1.2) \\ &= [j(j+1) - l(l+1) - s(s+1)]\, \zeta(LS) \quad , && (1.3) \end{aligned}$$

where $\zeta(LS)$ denotes the fine structure splitting.

The corresponding energy correction of the Darwin term, which only contributes to the energy of the states with $l = 0$ is

$$\Delta E'''_n \;=\; c^2\frac{\alpha^4 Z^4}{2n^3} \quad . \tag{1.4}$$

Comparison of Eq. (1.1) and Eq. (1.2) shows that the effects of the electron-mass velocity dependence and the electron spin have the same order of magnitude. The total correction to the energy $\Delta E'_{nl} + \Delta E''_{nlj} + \Delta E'''_n$ is given by the expression

$$\Delta E_{nlj} = \Delta E'_{nl} + \Delta E''_{nlj} + \Delta E'''_n = -\frac{\alpha^4 Z^4}{2n^4}\left(\frac{1}{j+1/2} - \frac{3}{4n}\right) \quad . \tag{1.5}$$

This splitting of the level nl into two components is called the *fine structure* splitting. The dimensionless constant α determines the magnitude of the splitting. It is important to note that, whereas both corrections $\Delta E'$ and $\Delta E''$ separately depend on l, the total correction ΔE does not depend on l but on j.

As the fine structure splitting decreases with increasing n approximately as $1/n^3$, this splitting is particularly important for lower levels. The set of lines arising from the transitions between the fine structures of the levels nl and $n^{'}l^{'}$ (transitions $nlj{\rightarrow}n'l'j'$) is a called multiplet (see Section 1.4).

1.1.2 Dirac equation

The corrected solution can be obtained by solving the Dirac equation. With an scalar potential $\varphi(\vec{r})$ and a vector potential $\vec{A}(\vec{r})$ describing an external electromagnetic field, the Dirac wave equation for a stationary state of total energy E is given by

$$H_D\Psi(\vec{r}) = E\Psi(\vec{r}) \ , \tag{1.6}$$

where the wave function Ψ depends on the position $\vec{r}$ and the spin of the electron and

$$H_D = -e\varphi + \beta E_0 + \alpha_i \cdot (c\vec{p} + e\vec{A}) \tag{1.7}$$

is the one-electron Dirac Hamiltonian. Here -e is the charge of the electron, $E_0 = m_0c^2$ and $\vec{p}$ are the electron rest energy and the momentum operator of the electron, respectively, with c the speed of light and m_0 the rest mass. The α_i and β Dirac operators are usually expressed in terms of the Pauli spin matrices (see definition in [BS57]).

The exact eigenvalues of states with a principal quantum number n and a quantum number j describing the total angular momentum are

$$E_{nj} = c^2 \left\{ \left[1 + \left(\frac{Z\alpha}{n - (j+1/2) + \sqrt{(j+1/2)^2 - (Z\alpha)^2}} \right)^2 \right]^{-1/2} - 1 \right\} . \qquad (1.8)$$

Here $\alpha = \mathrm{e}^2/\hbar \mathrm{c} \cong 1/137$ is the fine structure constant [WG34]. An expansion of this expression in powers of $(Z\alpha)^2$ yields:

$$E_{nj} = c^2 \frac{1}{2} \frac{(Z\alpha)^2}{n^2} \left[1 + \frac{(Z\alpha)^2}{n} \left(\frac{1}{j+1/2} - \frac{3}{4n} \right) \right] + \dots \ . \qquad (1.9)$$

However, even this exact solution does not give a complete description of the hydrogen atom. Indeed, the experiment made by Lamb and Retherford [LR47] in 1947 showed a splitting between ${}^2s_{1/2}$ and ${}^2p_{1/2}$ levels with the same j quantum number, which were predicted to be degenerate by Eq. (1.9). This observation led to some corrections [Wel48] to the Dirac electron theory.

1.2 QED corrections

The discrepancy between theory and experiment found in the fine structure of the second quantum state ($n = 2$) of hydrogen triggered the search for a theoretical explanation. Kemble and Present [KP32] as well as Pasternack [Pas38] showed that the shift of the 2s level could not be explained by a nuclear interaction of a reasonable magnitude, and Uehling [Ueh35] found that the effect of the polarization of the vacuum was much too small and it had, in addition, the opposite sign. Schwinger [Sch48] and Weisskopf [Wei39], as well as Oppenheimer [Opp30, Opp31, Opp35] suggested that a possible explanation might be a shift of the energy levels by the interaction of the electrons with the radiation field, an additional radiative correction called the self-energy of the electron.

Attempts to evaluate the radiative corrections to electron binding energies had heretofore been beset by divergence difficulties, which arise in the calculations as a consequence of virtual transitions involving photons with unlimited energy. Experiments later confirmed that the underlying elementary phenomena causing the Lamb shift were the self-energy of the electron and the polarization of the vacuum [Sch49]. These effects are essentially due to the interaction of the electrons with the vacuum fluctuations of the electromagnetic field.

1.2.1 Self-energy of the electron

In classical electrodynamics the self-energy of an electron without spin at rest consists solely of the energy-equivalent of its rest mass m_0 and of its electrostatic field, which diverges linearly for an infinitely small electron radius [Wei39].

The dominant contribution to the Lamb shift in a strong Coulomb potential, the self-energy, can be calculated accurately in the framework of QED [Moh75]. It is represented by means of a Feynman diagram in Fig. 1.1a. It describes the emission and the subsequent reabsorbtion of a virtual photon, *i.e.*, the interaction of the electron with its own radiation field. This leads to a considerable correction of the electron mass and binding energy. As an example, for the 1s Lamb shift in hydrogen, the self-energy contribution is 8396.456(1) MHz over the 8172.802(40) MHz of the total shift [WHK 95], roughly equivalent to 30 μeV.

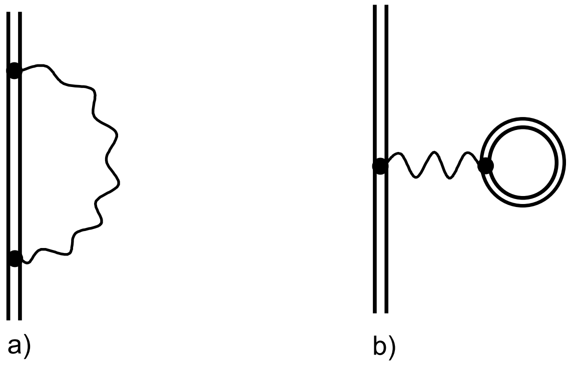

Figure 1.1: Feynman diagrams: a) the self-energy and b) the vacuum polarization of a bound electron. Double lines indicate wave functions and propagators in the external field of the nucleus.

To get a first impression concerning the importance of both radiative processes in highly charged ions we can consider the associated energy shift for a K-shell electron in hydrogen-like uranium. The sum of the calculated vacuum polarization and the self-energy corrections amounts to -266 eV, which should be compared with the total K-shell electron binding energy of 132 keV [MPS98].

1.2.2 Polarization of the vacuum

The vacuum-polarization, which was first treated by Uehling in 1935 [Ueh35] is shown in the Feynman diagram in Fig. 1.1b. This figure is often called the photon self-energy. Here, a virtual photon generates a virtual electron-positron pair which, in lowest order in the coupling constant $Z\alpha$ to the external field, is supposed to propagate freely, *i.e.*, undisturbed by the Coulomb field. The production of the virtual $e^+ - e^-$ pair gives rise to an effective modification of the Coulomb potential $1/r$ and thus, causes a shift of the electron binding energy. The vacuum-polarization potential has been accurately and efficiently evaluated to order $Z\alpha$ and $Z\alpha^2$ [FR76].

1.2.3 Reduced mass

The motion of the nucleus around the atomic center of mass modifies slightly the electron's energy and its magnetic moment [Sal52, Sch48]. The Dirac equation is limited in its application to the energy levels of a single electron moving around a nucleus and justified only to the extent that the electron may be considered to move in a fixed field of force. As a consequence, this equation is not valid for the discussion of the effect of the nuclear motion on the energy levels. The influence of the motion of the nucleus on the spectra of hydrogen and hydrogen-like light ions (which are not strongly affected by relativity) may be accounted for by replacing the electron mass m_0 by the reduced mass $\mu = m_0 M/(m_0 + M)$, M being the mass of the nucleus. This simple procedure does not suffice neither for systems with more than one electron nor for relativistic electrons.

1.3 Multi-electron systems

The Hamiltonian for multi-electron atoms is in most cases investigated under the independent-particle model, in which the electrons are assumed to move independently of each other in an average field due to the nucleus and the other electrons. The independent-particle model and the variational principle lead to the Hartree-Fock equations where the average potential is spherically symmetric.

1.3.1 The multi-configuration Hartree-Fock method

The Hartree-Fock (HF) method was developed to study atomic configurations containing closed shells. A method introducing a self-consistent field (SCF) for determining the wave functions and energy levels of an atom with many electrons was developed by Hartree [Har34], and later eveloped from a variational principle and modified to take account of exchange and of Pauli exclusion principle by Slater [Sla29] and Fock. No attempt was made to consider relativistic effects, and the use of spin wave functions was purely formal. However, since the relativistic corrections depend on the ratio Z/α, they are important for heavy atoms.

Attempts to set up relativistic self-consistent field calculations were initiated by Swirles in 1935 [Swi35]. She showed that the Dirac equation could be solved with a variational principle, and was able to carry out the relativistic version of the Hartree-Fock equations for a closed shell configuration. As her work predated to the modern developments using Racah tensor operators, she was unable to present the equations in the relatively simple form that we use now. The first numerical results were reported by Williams [Wil40], who neglected exchange terms. A number of calculations giving full solutions of the Hartree-Fock equations, including the exchange terms have been later on reported by Grant [Gra61].

A generalization of the HF method to account for electron correlation effects led to the so-called multi-configuration Hartree-Fock (MCHF) procedure [FS83]. In MCHF, corrections to the mean field description are accounted for by constructing the many-electron wavefunction as a linear combination of anti-symmetrized products of one-electron orbitals.

1.3.2 The multi-configuration Dirac-Fock method

The relativistic analogue method to the MCHF is the multi-configuration Dirac-Fock (MCDF) method [GMP76]. In the relativistic Dirac-Fock method the Hamiltonian for an N-electron atom is given by

$$H = \sum_{i=1}^{N} H_i + \sum_{i<j}^{N} \frac{1}{r_{ij}} \quad , \tag{1.10}$$

where H_i is the Dirac Hamiltonian for an electron i including the nuclear Coulomb interaction (see Eq. (1.7)) and $r_{ij} = |\vec{r_i} - \vec{r_j}|$ is the difference between the positions $\vec{r_i}$, $\vec{r_j}$ of the electrons i and j, respectively.

Each atomic state is expressed as a linear combination of N-electron basis functions. These are constructed from single-electron central-field Dirac spinors $u_a(r)$ of the form [Gra70]

$$u_a(r) = \frac{1}{r} \begin{pmatrix} P_a(r) & \chi_a \\ iQ_a(r) & \bar{\chi}_a \end{pmatrix} \quad , \tag{1.11}$$

where $P_a(r)$ and $Q_a(r)$ are the purely radial functions. χ_a and $\bar{\chi}_a$ are the two-component spherical spinors. The label a represents the set of $n_a l_a j_a m_{j_a}$ quantum numbers (where $P_a(r)$, $Q_a(r)$ depend only on n, l and j and χ_a, $\bar{\chi}_a$ depend on l, j and m).

The orbitals $u_a(r)$ are eigenfunctions of $\vec{j}^2$, j_z and the parity operator P. The parity of the state is given by (-1)^{l_a}, where $l_a = j_a \pm \frac{1}{2}$ is the orbital angular momentum of the large component. The eigenvalues of $\vec{j}^2$ and j_z are given by $j_a(j_a+1)$ and m_{ja}, respectively. Under the assumption that $u_a(r)$ forms an orthonormal set, the configuration state functions (CSF) are constructed as linear combinations of anti-symmetrized products of single-particle spinors of the form

$$u_{a_1}(\vec{r}_1)u_{a_2}(\vec{r}_2)...u_{a_N}(\vec{r}_N) \quad , \tag{1.12}$$

corresponding to an assignment of the N electrons to specified states $a_1, a_2, ..., a_N$. They are coupled together to give an eigenstate of the sequence total angular momentum $\vec{J}^2$ and its z-component J_z, with $\vec{J}$ being $\vec{J} = \sum_{i=1}^{N} \vec{j}_i$.

These CSF, denoted by $\Phi_r(\gamma_r PJM)$, are eigenfunctions of $\vec{J}^2$ and J_z, belonging to the eigenvalues $J(J+1)$ and M_J the z component of the total angular momentum, and of parity P. The label γ_r denotes the set of internal symmetry labels necessary to define an orthonormal N-electron basis. A general open-shell atomic state is expressed as a linear combination of CSF belonging to the same P and M. Such a linear combination is called an atomic state function (ASF) and written as

$$\Psi_\alpha(PJM) = \sum_{r=1}^{N} c_{r\alpha}\Phi_r(\gamma_r PJM) \quad . \tag{1.13}$$

The essence of the MCDF method is to determine the configuration-mixing coefficients $c_{r\alpha}$ and the orbitals $u_a(r)$ by applying the variational method to the expectation values of the Hamiltonian with respect to the ASF $\Psi_\alpha(PJM)$.

The relativistic Dirac-Fock equations for neutral atoms or ions in a bound state have been solved numerically within the framework of the multi-configuration approximation at first by Desclaux [Des75] and Grant [GMN 80].

1.3.3 The many-body perturbation theory

The Hartree-Fock method deals with particles with weak or long-range interactions. However this method is difficult to apply to systems of particles which interact strongly through short-range potentials. The origin of the difficulty lies in the strong correlations which might exist in the wave-functions of the multi-particle system, and which are neglected in the Hartree-Fock method.

The development of many-body perturbation theory (MBPT) was initiated by Brueckner [BL55, Bru55] and Goldstone [Gol57], which introduced the one-body potential. This procedure was later extended to general open-shell systems by Brandow [Bra67] and Lindgren [Lin85].

As follows from Eq. (1.10) the non-relativistic Hamiltonian for an atomic system is (in atomic units),

$$H = -\frac{1}{2}\sum_{i=1}^{N} \nabla_i^2 - \sum_{i=1}^{N} \frac{Z}{r_i} + \sum_{i<j} \frac{1}{r_{ij}} \quad , \tag{1.14}$$

where the terms on the right-hand side represent the kinetic energy, the nuclear attraction and the inter-electronic repulsion, respectively. Relativistic effects, such as the spin-orbit interaction, and effects of the radiation field (QED) are omitted here. Except for the simplest systems, the eigenvalues of this Hamiltonian cannot be determined exactly and various approximation schemes have to be applied.

A first scheme results from applying perturbation theory. Here, the Hamiltonian is divided into two parts:

$$H = H_0 + V \quad , \tag{1.15}$$

where H_0 is an approximate (unperturbed) Hamiltonian, which can be treated exactly and should be a reasonably good approximation of the full Hamiltonian and V is the perturbation. The unperturbed Hamiltonian H_0 is assumed to be the Hamiltonian of the central-field model given by

$$H_0 = \sum_{i=1}^{N} \left[-\frac{1}{2}\nabla_i^2 - \frac{Z}{r_i} + U(r_i) \right] = \sum_{i=1}^{N} h_0(i) \quad , \tag{1.16}$$

where $U(r_i)$ represents a Hartree-Fock central potential approximating the effect produced by the other electrons. Here the electrons move independently of each other in a spherically symmetric field. Furthermore, this field is considered to be the same for all electrons.

The perturbation V is the non-central part of the electrostatic interaction

$$V = \sum_{i<j} \frac{1}{r_{ij}} - \sum_{i=1}^{N} U(r_i) \quad . \tag{1.17}$$

A second method used to treat many-body systems is the relativistic many-body perturbation theory (RMBPT) first introduced by Johnson, Blundell and Sapirstein [JBS88a, JBS88b]. This method is particularly well suited for calculations of the properties of highly charged multi-electron ions because of the rapid convergence of the $1/Z$ expansion [Doy69], which is of crucial importance for this technique.

To summarize, the methods employed in the calculation of relativistic bound-state energies of multi-electron systems can be divided into two classes [Kim97]. In the first class, the relativistic effects are partially taken into account in the calculation of the wave-functions. Such methods are based upon a generalization of the Dirac equation for an electron in a central field to a multi-electron case. The principal method whitin this category is the relativistic Hartree-Fock method. Also in this category is the relativistic $1/Z$ expansion theory, in which relativistic hydrogenic wave-functions are used. The second class of methods includes all approaches based upon non-relativistic wave-functions. In these methods the relativistic effects are taken into account in the perturbation terms of the Hamiltonian only. For atoms with relatively small nuclear charge Z (strictly those for $(\alpha Z)^2 \ll 1$) the relativistic Hamiltonian is taken to be the Breit-Pauli Hamiltonian.

1.4 Radiative transitions

Depending on the type of radiative transition which take place in a multi-electron atom, different so-called *selection rules* apply. These rules depend on the quantum numbers of initial and final states of the electronic systems (see Table 1.1). The strongest transitions result from the electric dipole interaction E1. Transitions that obey the selection rules for E1 are called *allowed* transitions. If these selection rules are not satisfied, the dipole moment is zero, and the transition rate is also zero (see below). In such a case, the excited state can relax through so-called *forbidden* transitions [Bow36]. For cases where E1 radiative transitions are forbidden, the upper state is said to be metastable. The use of the word *forbidden* is somewhat misleading here, it actually means *electric-dipole forbidden.* These transitions are possible, but just occur at slower rates than E1. After the electric dipole interaction, the next two strongest interactions between the photon and the atom give rise to the magnetic dipole M1 and electric quadrupole E2 forbidden transitions. The M1 and E2 transitions have much smaller probabilities than E1 transitions. However, these processes become stronger for highly charged ions, and the transition probabilities for M1, E2 ... lines grow with -in most cases- high powers of the ionic charge Z. For instance, for H-like ions the transition probability of the M1 radiation, if the energy level separation is primarily due to spin-orbit interaction, scales with Z^{10}. Thus, the forbidden transitions can be very strong in highly charged ions. As an example of the different possible radiative transitions a typical level scheme for Kr XIX is shown in Fig. 1.2.

Table 1.1: Selection rules between discrete states transitions

		Electric dipole (E1) "allowed"	**Magnetic dipole (M1) "forbidden"**	**Electric quadrupole (E2) "forbidden"**
Rigorous rules	1.	$\Delta J = 0, \pm1$ $(0 \not\leftrightarrow 0)$	$\Delta J = 0, \pm1$ $(0 \not\leftrightarrow 0)$	$\Delta J = 0, \pm1, \pm 2$ $(0 \not\leftrightarrow 0)$ $(1/2 \not\leftrightarrow 1/2)$ $(0 \not\leftrightarrow 1)$
	2.	$\Delta M_J = 0, \pm 1$ $(0 \not\leftrightarrow 0$ when $\Delta J = 0)$	$\Delta M_J = 0, \pm 1$ $(0 \not\leftrightarrow 0$ when $\Delta J = 0)$	$\Delta M_J = 0, \pm 1, \pm 2$
	3.	Parity change	No parity change	No parity change
For *LS*-coupling only	4.	$\Delta S = 0$	$\Delta S = 0$	$\Delta S = 0$
	5.	$\Delta L = \pm 1$ $(0 \not\leftrightarrow 0)$	$\Delta L = 0$ $\Delta J = \pm 1$	$\Delta L = 0, \pm 2$ $(0 \not\leftrightarrow 0)$ $(0 \not\leftrightarrow 1)$

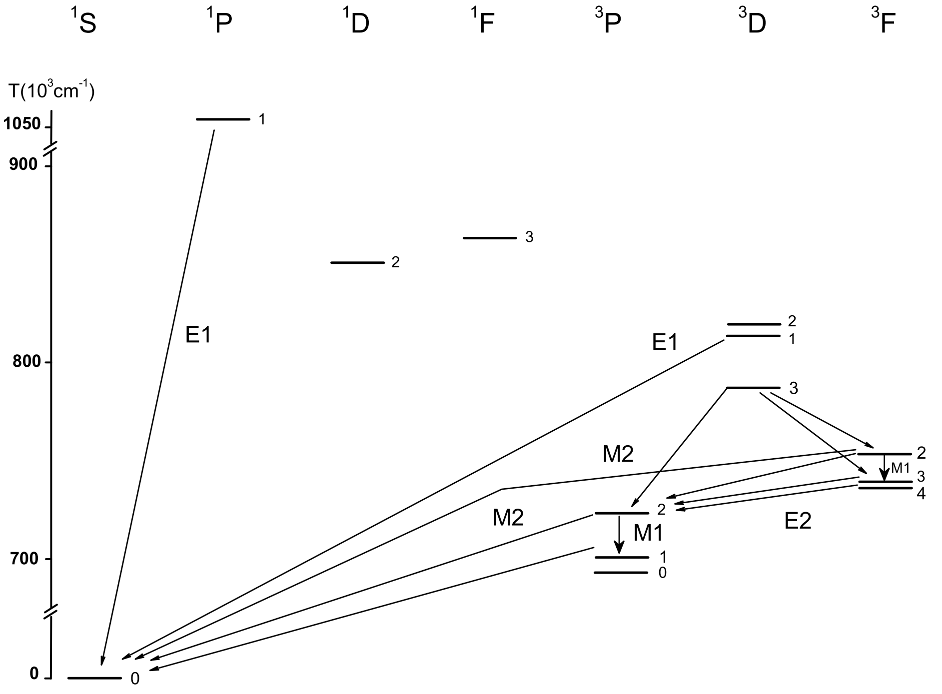

Figure 1.2: Level scheme of the $3s^23p^53d$ levels in the Ar-like krypton (KrXIX) [TBB 01]. The energy scale is only approximate.

1.4.1 The magnetic dipole forbidden transition

The transition rate A_{12} within fine structure states is calculated from the initial and final wave functions (Ψ_1, Ψ_2) of the involved states by using the Fermi golden rule:

$$A_{12} = \frac{2\pi}{\hbar} \left| M_{12} \right|^2 g\left(h\nu\right) \quad , \tag{1.18}$$

where M_{12} is the transition matrix element and $g(h\nu)$ is the degeneracy or density of states. The matrix element is equal to the overlap integral:

$$M_{12} = \int \Psi_2^* \left(\vec{r}\right) B' \left(\vec{r}\right) \Psi_1 \left(\vec{r}\right) d^3\vec{r} \ . \tag{1.19}$$

where B' is the interaction between the atom and the photon wave that causes the transition.

When the transitions are taking place via the magnetic dipole mechanism, the expression for the B' is given by the operator of the magnetic moment

$$Q^{M1} = -\frac{e\hbar}{2m_0 c} \sum_i (\vec{l}_i + 2\vec{s}_i) \quad , \tag{1.20}$$

which takes into account the sum over all electrons i of the orbital angular momentum $\vec{l}_i$ and the spin $\vec{s}_i$ of the individual electrons.

The magnetic dipole line strength for a transition between two states within the LS-coupling, in the notation of Condon and Shortley [CS59], is given as the squared reduced matrix element

$$S^{M1}_{nlj,n'l'j'} = \left| \left\langle \alpha J || Q^{M1} || \alpha J' \right\rangle \right|^2 \quad . \tag{1.21}$$

Here, l, j and l', j' are the quantum numbers of the active electrons participating in the transition. As M1 transitions are only possible between components of the fine structure $J = L + 1/2$ and $J' = L - 1/2$ ($J' = J - 1$), a final expression is given by

$$S^{M1}(LJ, LJ') = \frac{(L+1/2+J+1)(L+1/2-J+1)(J-L+1/2)(J+L-1/2)}{4J} \ . \tag{1.22}$$

In this special case, this quantity does not depend on the n, n' quantum numbers anymore [CLFM01]. Relationships between the oscillator strength S (dimensionless) and the transition probability A is generally valid for M1 and E1 transitions. In SI units A^{M1} (in s^{-1}) is related to S^{M1} by the expression

$$A^{M1} = \frac{16\pi^3\mu_0}{3h\omega_i\lambda^3} S^{M1} \quad , \tag{1.23}$$

where μ_0 is the vacuum permeability, ω_i is the statistical weight of the initial state and λ is the transition wavelength.

For the electric dipole the transition probability is written as follows

$$A^{E1} = \frac{16\pi^3}{3h\epsilon_0\omega_i\lambda^3} S^{E1} \quad , \tag{1.24}$$

where ϵ_0 is the vacuum permittivity.

In Fig. 1.3 the transition probabilities for the E1 and M1 transitions along the H-like isoelectronic sequence are compared. The values of A are plotted against

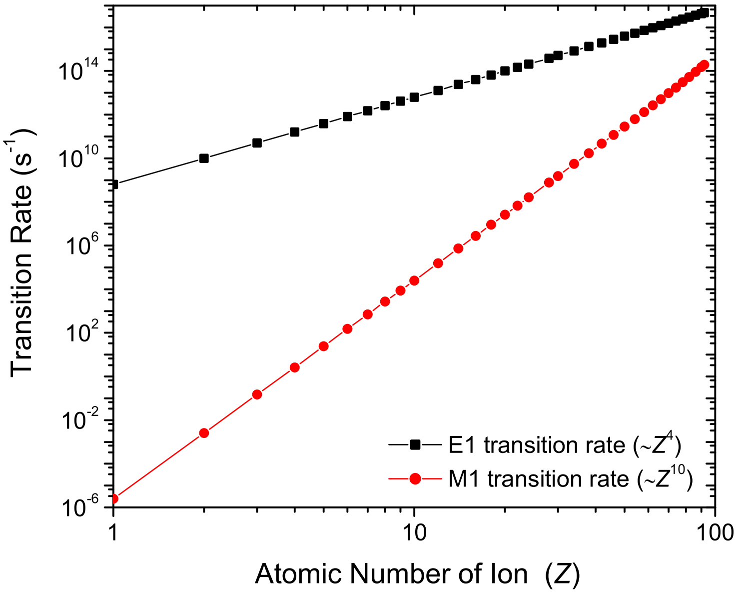

Figure 1.3: Transition probabilities versus the ion charge Z for the H-like isoelectronic sequence for $^2P_{1/2}$ – $^1S_{1/2}$ E1 transition (open triangles) and the $^2S_{1/2}$ – $^1S_{1/2}$ M1 transition (open circles) [BS03].

the atomic number Z of ions [BS03]. As we can see, the electric dipole transitions have much larger probabilities than the M1 transitions. It can also be seen that the transition probabilities for these two cases increase with different powers of Z.

1.5 External magnetic field. Zeeman effect

Now we consider states of an atom or ion that lay in a uniform external magnetic field. For a small perturbation H_B the interaction is written in the classical form as follows

$$H_B = -\vec{\mu} \cdot \vec{B} = -\frac{\mu_B}{\hbar}(\vec{L} + 2\vec{S}) \cdot \vec{B} = -\frac{\mu_B}{\hbar}(\vec{J} + \vec{S}) \cdot \vec{B} \ , \tag{1.25}$$

where $\vec{\mu}$ is the total magnetic moment of the electronic system and $\vec{B}$ the external magnetic field. In terms of the orbital and spin magnetic moment the interaction, in the non-relativistic limit, is given by

$$H_B = \left(\sum_i g_L \mu_B \vec{l}_i + \sum_i g_S \mu_B \vec{s}_i \right) \cdot \vec{B} \ , \tag{1.26}$$

where both g_L and g_S, the orbital and spin g-factors are defined to be positive.

It is important to consider the size of the perturbation H_B compared with other terms in the Hamiltonian. In the case of a *weak field*, the LS-coupling approximation is used. Here, the energy splitting produced by the external field ($\approx \ \mu_B B$) is small compared to the fine structure splitting $\zeta(LS)$ of Eq. (1.3) which is proportional to the internal magnetic field of the atom ($\approx \ \mu_B B_{int}$); we speak here of the Zeeman effect [Zee97]. In a *strong field* ($\mu_B B \ \gg \ \zeta(LS)$) the LS-coupling is no longer appropriate. The field-induced precessions are so rapid that we must take into account the total angular momentum $\vec{L}$ and spin $\vec{S}$ as they individually precess about $\vec{B}$, that is, the effect of $\vec{B}$ is effectively to decouple $\vec{L}$ from $\vec{S}$, and to make $\vec{J}$ meaningless. In this limit we speak of the Paschen-Back effect [PB12]. Then, it is appropriate to describe the atom in terms of partially coupled basis functions $|\gamma LSM_LM_S\rangle$, where M_L and M_S are the projections on the z-axis, *i.e.*, the direction of $\vec{B}$, of the $\vec{L}$ and $\vec{S}$, respectively.

Zeeman effect in LS-coupling

In first order perturbation theory the energy shift caused by the Zeeman effect is given by

$$\Delta E = \langle \gamma LSJM_J | H_B | \gamma LSJM_J \rangle \ , \tag{1.27}$$

and Eq. (1.26) is rewritten as

$$\begin{aligned} H_B &= \mu_B(\vec{L} + g_s\vec{S}) \cdot \vec{B} \\ &= \mu_B B(L_z + g_s S_z) \ , \end{aligned} \tag{1.28}$$

where L_z and S_z are the projections of the total angular momentum and spin onto the axis defined by the direction of the external field, respectively.

In Fig. 1.4 we show a vector model where $\vec{L}$ and $\vec{S}$ precess rapidly around $\vec{J}$ with a precession rate proportional to $\zeta(\gamma LS)$, while $\vec{J}$ slowly precesses around the z-axis with a rate proportional to $\mu_B B$ ($<\zeta(\gamma LS)$).

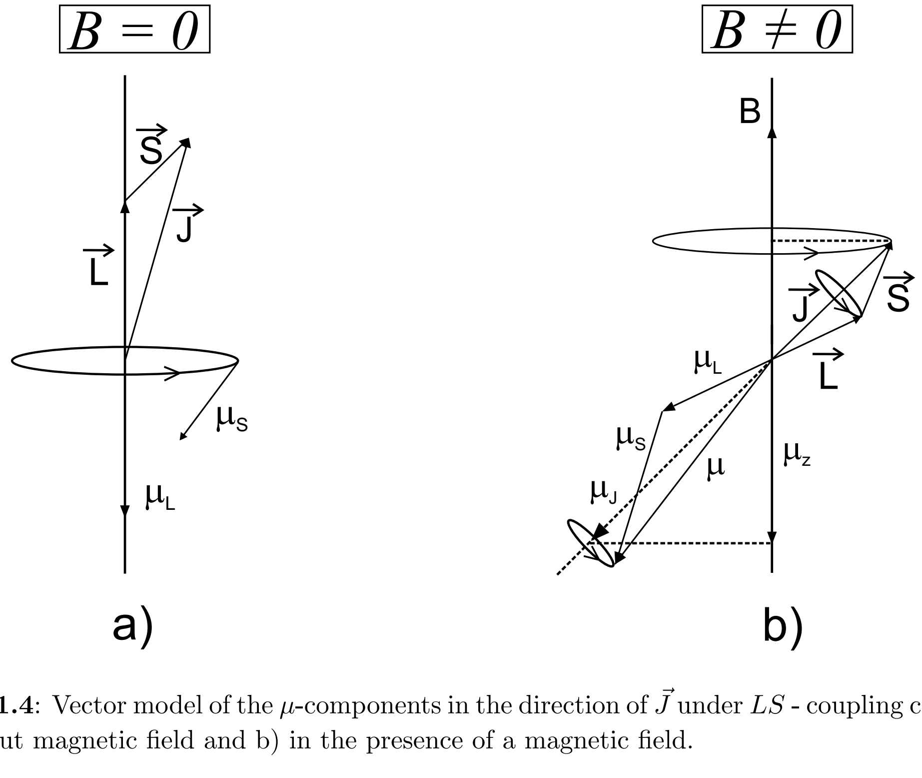

Figure 1.4: Vector model of the μ-components in the direction of $\vec{J}$ under LS - coupling conditions. a) without magnetic field and b) in the presence of a magnetic field.

To evaluate the matrix elements of L_z and S_z we take the projection of $\vec{L}$ onto $\vec{J}$ and then project it onto the z-axis (along the B direction), and in the same manner the projection of $\vec{S}$ onto $\vec{J}$. Using the identities

$$\begin{cases} \vec{L}\cdot\vec{J} = \frac{1}{2}(\vec{J}^2 + \vec{L}^2 - \vec{S}^2) \\ \vec{S}\cdot\vec{J} = \frac{1}{2}(\vec{J}^2 - \vec{L}^2 + \vec{S}^2) \ , \end{cases}$$

the energy shift becomes

$$\begin{aligned} \Delta E = \mu_B B \langle \gamma LSJM_J | \tfrac{1}{2} \Big\{ & (\vec{J}^2 + \vec{L}^2 - \vec{S}^2) \\ & + g_S(\vec{J}^2 - \vec{L}^2 + \vec{S}^2) \Big\} \tfrac{J_z}{J(J+1)} | \gamma LSJM_J \rangle \ , \end{aligned} \tag{1.29}$$

where $J_z = L_z + S_z$. Making the projection of the total magnetic moment μ_B of the electrons onto $\vec{J}$ we can define an effective μ-factor by

$$\mu_{\text{eff}} = -g_J \mu_B J_z \ , \tag{1.30}$$

where g_J depends on L, S and J. The energy shift is then written as follows:

$$\begin{aligned} \Delta E &= \langle \gamma LSJM_J | - \mu_{\text{eff}} B | \gamma LSJM_J \rangle \\ &= \langle \gamma LSJM_J | g_J \mu_B B J_z | \gamma LSJM_J \rangle \\ &= g_J \mu_B B M_J \ . \end{aligned} \tag{1.31}$$

Comparing Eq. (1.31) with Eq. (1.29) the Landé g_J-factor is obtained:

$$g_J = \tfrac{J(J+1)+L(L+1)-S(S+1)}{2J(J+1)} + g_S \tfrac{J(J+1)-L(L+1)+S(S+1)}{2J(J+1)} \ . \tag{1.32}$$

For a singlet state ($S = 0$, $J = L$), we obtain g_J=1, independently of L, S, and J. In the absence of spin, the *normal* Zeeman effect results just from the interaction of the orbital moment L with the external field, and the interaction energy of the atom is therefore

$$\Delta E = -\mu_z B = \mu_B B M_L \ , \tag{1.33}$$

where M_L is the orbital magnetic quantum number. This equation shows us that the application of an external B-field splits the degenerate M_L states evenly. For a transition between two singlet levels the energy spacing between the states is $\mu_B B$, the same for each term, and the photon energy is

$$h\nu = h\nu_0 + \mu_B B \Delta M_L \ , \tag{1.34}$$

where $h\nu_0$ is the energy difference between the unperturbed levels.

The polarization of the Zeeman lines is determined by the selection rules and the observation angle. If we are looking along the field (longitudinal observation), the photons must be propagating in the z-direction. Light waves are transverse and therefore only the x and y polarizations are possible. When observing at right angles to the field (transverse observation), all three lines are present (see Fig. 1.5a). In both cases the lines are symmetrically arranged around the position of the unperturbed transition and separated by $\mu_B B/h$.

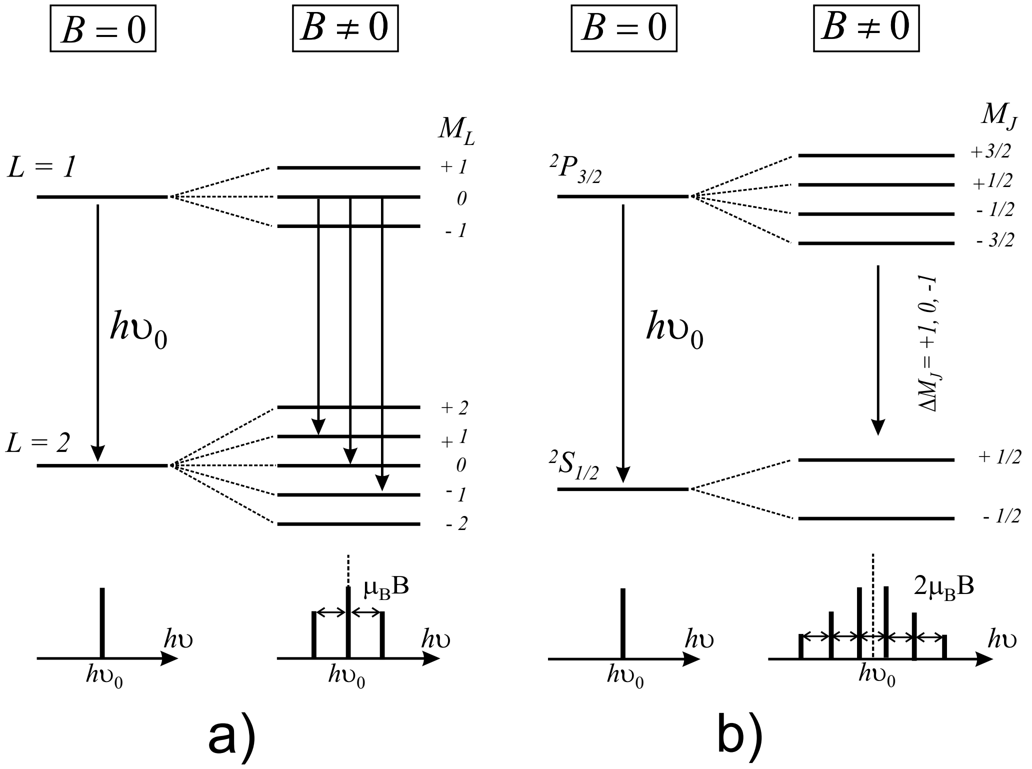

Figure 1.5: a) Normal Zeeman effect for a p → d transition. The field splits the degenerate M_L levels equally. Optical transitions can occur if $\Delta M_L = 0,\pm1$. (For the sake of clarity, only the transitions originating from the $M_L = 0$ level of the $L = 1$ state are labeled.) b) Anomalous Zeeman splitting of the sodium D-line (D_2 = 589.0 nm) by a weak magnetic field.

For general case of transitions between multiplets in LS-coupling, the situation is different. In this case $g_J \neq 1$ depending on the L, S and J and, hence, it is different for each level. This is known as the *anomalous* Zeeman effect, which is the most common case despite of its name. The frequency of the transition $(\gamma LSJM_J) \rightarrow (\gamma' L' S' J' M_J')$ is given by

$$\begin{aligned} h\nu &= (E' + \Delta E') - (E + \Delta E) \\ &= h\nu_0 + \mu_B B (g_J' M_J' - g_J M_J) \ , \end{aligned} \tag{1.35}$$

where g_J and $g_{J'}$ correspond to the Landé g-factors of the initial and final states, respectively (see Fig. 1.5b).

In the Zeeman effect, the field-dependence of the energy of each state is in first order linear in B, as shown in Fig. 1.6. From Eq. (1.31) one can express the expectation value of μ_z as the negative slope of the energy with respect to the field:

$$\langle \mu_z \rangle = -\frac{\partial E}{\partial B} = -g_J \mu_B M_J \ . \tag{1.36}$$

In the Paschen-Back regime this dependence is not any longer linear as it can be seen in Fig. 1.6. A direct measurement of the electron moment can most easily be made by a measurement of the g-factor of an atomic energy state [Phi49]. Direct

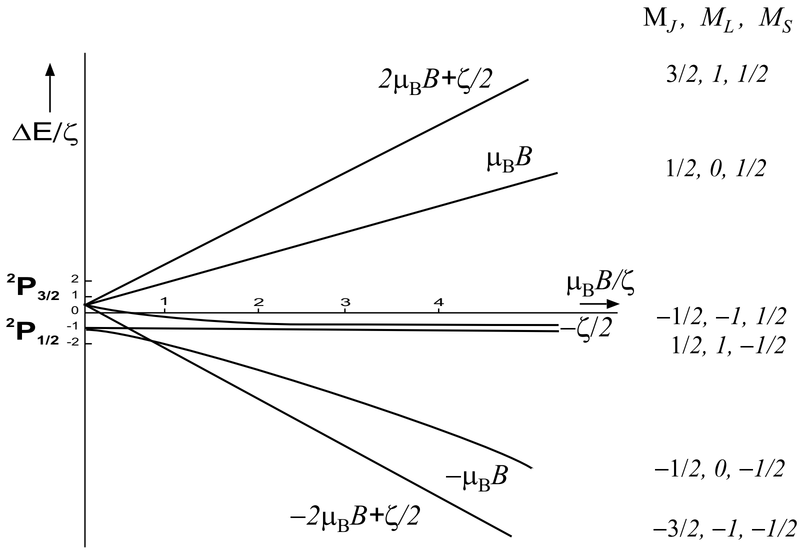

Figure 1.6: The dependence of the Zeeman energy states of ^2P term on the magnetic field. $\Delta E/\zeta$ is plotted as a function of $\mu_B B/\zeta$. The ΔE is plotted for $g_S = 2$.

determinations of the g-factors of atomic states can be done by measurements of the frequencies of Zeeman lines in a known magnetic field [KF48].

Polarization and intensity of the multiplet Zeeman components

The polarization expresses the direction of the electric vector $\vec{E}$ in a given coordinate system, whereas the intensity of a line is proportional to the magnitude $|\vec{E}^2|$. Table 1.2 shows the polarization directions for E1, M1, and E2 transitions. Conventionally, π-components are those polarized parallel to the external field (the θ direction), and σ-components are those polarized perpendicular to the field (the ϕ direction). As a particularity, for the longitudinal view ($\theta = 0°$), only the $\Delta M_J = \pm 1$ components appear and are always circularly polarized. Thus, the longitudinal observations cannot distinguish the type of transition.

Table 1.2: Multipole Zeeman component polarizations. θ is the observation angle with respect to the magnetic field axis. π and σ are linear polarized. The elliptical and circular lights are right (r) and left (l) polarized. The symbol —— denotes zero intensity

Transition type		**Transverse ($\theta = 90^0$)**	**Diagonal ($\theta = 45^0$)**	**Longitudinal ($\theta = 0^0$)**
E1	$\Delta M_J = 0$	π	π	——
	$\Delta M_J = \pm 1$	σ	elliptical (r, l)	circular (r, l)
M1	$\Delta M_J = 0$	σ	σ	
	$\Delta M_J = \pm 1$	π	elliptical (r, l)	circular (r, l)
E2	$\Delta M_J = 0$	——	π	——
	$\Delta M_J = \pm 1$	π	elliptical (r, l)	circular (r, l)
	$\Delta M_J = \pm 2$	σ	elliptical (r, l)	——

Because the electric and the magnetic fields are perpendicular to each other, the M1 Zeeman components have *opposite polarizations* to the E1 components. In the case of E1 transitions, the central components (ΔM_J=0) are polarized parallel to the field. Meanwhile, in M1 transitions the central components are polarized perpendicular to the field. And hence, for M1 radiation, the $\Delta M_J = 0$ transitions are σ-components, and the $\Delta M_J = \pm 1$ transitions are π-components (see Fig. 1.7) [SM68].

The angular distribution of the magnetic dipole radiation is identical with that of the electric dipole radiation, and therefore, the Zeeman patterns for M1 are given by the same equations as for E1. In many laboratory sources, the magnetic sublevels are

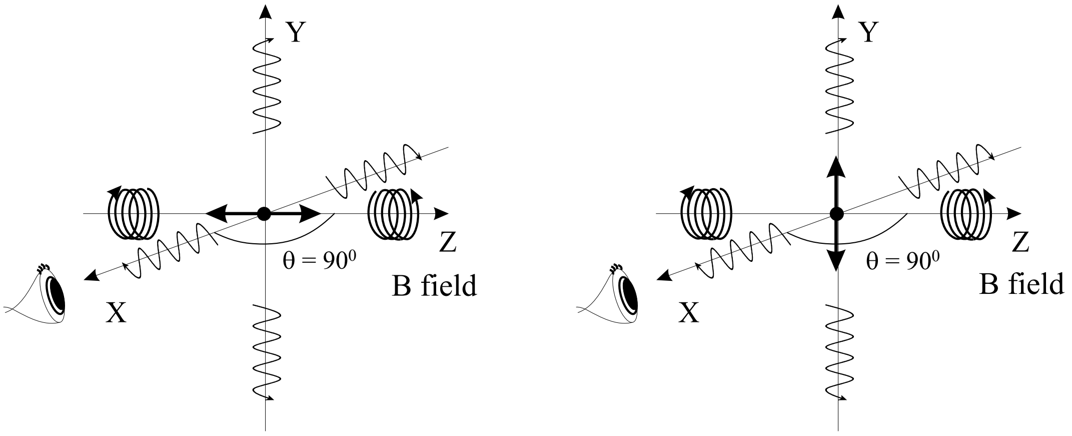

$\pi\ (\Delta M_J = \pm 1)$ $\sigma\ (\Delta M_J = 0)$

Figure 1.7: For M1 transitions, the π- and σ-components are linearly polarized (parallel and vertical to the B-field, respectively) at the observation angle of $\theta = 90^0$.

populated equally so that only the atomic transition probability and the multipole field intensity have to be considered when calculating the line intensities. For dipole transitions (E1 or M1), the field intensity pattern $I_{lq}(\theta)$, where l is the multiplet type ($l = 1$ for dipole) and $q = \Delta M_J$, is

$$\begin{aligned} I_{10}(\theta) &= \frac{3}{8\pi} sin^2\theta \\ I_{1\pm1}(\theta) &= \frac{3}{8\pi}\frac{1+cos^2\theta}{2} \quad . \end{aligned} \tag{1.37}$$

1.6 Nuclear interaction. Isotopic shifts

For atoms with different nuclear mass M but the same nuclear charge Z, their nuclear structures, shape and finite mass produces small but discernible shifts on the energy levels known as *isotopic shifts.* This energy shift is caused by two effects: The first one is due to the fact that the atomic level is described by eigenfunctions with eigenvalues for the angular momentum and energy. As the former has a defined fixed value, any change in the mass affects the total energy. This is known as the *mass shift* (MS). Second, even though different isotopes have the same number of protons they have different mass distributions in the nucleus. Depending on the size and shape of the nuclear electronic charge distribution, the energy of an atomic level is different. This nuclear charge distribution, depending on the number of neutrons, modifies the electric field at short distances from the origin and thus influences the energy of the atomic electrons. This change in the level energy is called the *field shift* (FS). In other words, the mass shift or recoil effect arise from the finiteness of the nuclear mass, and the field shift arise from the finite nuclear size.

The mass effect tends to decrease with Z since the atomic mass increases with Z and thus, the ratio m_0/M is reduced, whereas the field effect tends to increase with Z because the size of the electronic orbitals becomes smaller and the ratio of the nuclear size to the orbital size as well as their mutual overlap increases. Hence, for light elements, *i.e.*, small Z, the mass effect is generally predominant over the field effect while for heavier elements the field effect is dominant over the mass effect. Generally, the total shift is small for intermediate Z ($Z \approx 20$ to 40).

1.6.1 Mass shift

The nuclear mass effect is originated from the fact that the mass of the electron is not completely negligible compared with the mass of the nucleus. This effect is explained by assuming that the nucleus and the electron revolve about their common center of mass. It has been discussed and satisfactory compared with the observed displacements for H_α and D_α [PWH94, Pac94]. In atoms with more than one electron, since the optical electron interacts with all other electrons as well as with the nucleus, the problem is much more complex. A common approximation for this case consists in separating the nuclear mass contributions into two parts, the normal mass shift (NMS) and the specific mass shift (SMS) sometimes also called mass polarization correction. This second part includes the contributions characteristic of the many-body problem.

In the one-body problem the energy is corrected by the replacement of the electron mass by the reduced mass $\mu = m_0 M/(m_0+M)$, where m_0 is the electron rest mass and M is the nuclear mass. This change in mass leads to the energy correction

$$E^{nr}_{NMS} = E - E_0 = -E_0 \frac{m_0}{m_0 + M} \quad , \tag{1.38}$$

where the superscript nr is used for non-relativistic. This equation represents the exact evaluation of the NMS approximation. For systems having more than one electron calculations need to include electron-electron correlation effects, which cause an additional shift called specific mass shift. For multi-electron systems a non-relativistic calculation of the SMS was first performed by Hughes and Eckart [HE30]. The energy correction is given by

$$E^{nr}_{SMS} = E - E_0 = -\left\langle \psi \left| \frac{1}{M} \sum_{i<j}^{N} \nabla_i \nabla_j \right| \psi \right\rangle \quad . \tag{1.39}$$

Relativistic corrections to the order $(v/c)^2$ were derived, with the aid of the Breit [Bre29] two-body relativistic interactions, to the order m_0/M by Lowen [Low37]. A full relativistic theory of the nuclear mass effect can only be formulated whitin the framework of quantum electrodynamics [TSC 03]. Such a theory was first presented by Shabaev [Sha85], who derived complete formulae as a function of αZ for the recoil corrections to the atomic energy levels to first order in m_0/M. Pachuki derived also formulae to calculate the mass corrections in H-like atoms to order $(\alpha Z)^6 m_0^2/M$ [PG95]. Whitin the lowest-order relativistic approximation ($\approx (v/c)^2$) and to the first order in m_0/M, the sum of the mass corrections can be derived by using the following mass Hamiltonian

$$H^{rel}_{M} = \frac{1}{2M} \sum_{ij} \left[\vec{p}_i \cdot \vec{p}_j - \frac{\alpha Z}{r_i} \left(\vec{\alpha}_i + \frac{(\vec{\alpha}_i \cdot \vec{r}_i)\vec{r}_i}{r_i^2} \cdot \vec{p}_j \right) \right] \quad , \tag{1.40}$$

where the superscript *rel* refers to relativistic, $\vec{\alpha}$ is a vector incorporating the Dirac matrices and $\vec{p}_{i,j}$ are the four momentum operator of the electrons. The expectation value of H^{rel}_M on the Dirac wave function yields the total mass correction.

By separating Eq. (1.40) into two parts, the lowest-order relativistic correction to the one-electron normal mass operator can be written as follows:

$$H^{rel}_{NMS} = -\frac{1}{2M} \sum_{i} \frac{\alpha Z}{r_i} \left(\vec{\alpha}_i + \frac{(\vec{\alpha}_i \cdot \vec{r}_i)\vec{r}_i}{r_i^2} \cdot \vec{p}_i \right) \quad . \tag{1.41}$$

The corresponding two-electron correction or specific mass shift is

$$H^{rel}_{SMS} = -\frac{1}{2M} \sum_{i \neq j} \frac{\alpha Z}{r_i} \left(\vec{\alpha}_i + \frac{(\vec{\alpha}_i \cdot \vec{r}_i)\vec{r}_i}{r_i^2} \cdot \vec{p}_j \right) \quad . \tag{1.42}$$

To the lowest order in m_0/M, the mass isotope shift between two ion masses M_1 and M_2, is determined as the difference of the expectation values of the finite mass correction Hamiltonian H^{rel}_M for two different isotopes H^{rel}_{M1}, H^{rel}_{M2} as

$$\delta E_{MS}^{rel} = \left\langle \psi | H_{M1}^{rel} - H_{M2}^{rel} | \psi \right\rangle \quad , \tag{1.43}$$

where $|\psi\rangle$ is the eigenvector of the Dirac-Coulomb-Breit Hamiltonian.

1.6.2 Field shift

If a bound electron has an appreciable probability density at zero radius, as in the case of an s electron, then the binding energy of the system is lower if the nucleus is spread out, for instance over a sphere with radius R. This consideration is not essentially changed by the presence of other electrons around the nucleus, except for a certain amount of screening by other s electrons. The extended structure of the nucleus was first suggested by Goudsmit [PG30] as the reason for the isotope shift observed in the spectra of heavy atoms. Between two isotopes, the binding energy is higher for the (heavier) one with the greater radius. This effect gives rise to the field shift. The magnitude of the volume effect depends somewhat upon the radial charge distribution in the nuclear model chosen; the influence of the charge distribution was first studied by Humbach and later reviewed by Ford and Hill [FH55].

To a good approximation, for an s electron the field shift can be approximated as:

$$\Delta E_{field} = |\psi(0)|^2 \left\langle V - V' \right\rangle \quad , \tag{1.44}$$

where $|\psi(0)|$ is the electronic wave function at the nucleus and V, V' are the electrostatic potentials in the region close to the nucleus for the two different isotopes, respectively. This approximation assumes that the nuclei are uniform and spherical, and that the electronic wavefunction is uniform over the nuclear radius. Further analysis along these lines yields:

$$\Delta E_{field} = \frac{2\pi}{3} Z |\psi(0)|^2 \left(\left\langle r_A^2 \right\rangle - \left\langle r_{A'}^2 \right\rangle \right) \quad , \tag{1.45}$$

where $\langle r^2 \rangle$ is the difference of the mean-square nuclear radii between two different masses A and A'.

Then, the field shift can be written as

$$\delta\nu_{i,field}^{AA'} = F_i \lambda^{AA'} \quad , \tag{1.46}$$

where $\delta\nu_i^{AA'}$ is the difference in transition frequency for the two isotopes (i) with masses A and A', respectively, and $\lambda^{AA'}$ is defined by

$$\lambda^{AA'} = \tilde{K}\delta\left\langle r^2\right\rangle^{AA'} \quad , \tag{1.47}$$

where $\tilde{K}$ can be approximated theoretically, but only differs significantly from unity for heavy nuclei. And F_i is a relativistic electronic factor defined in the following manner:

$$F_i(r) = \frac{\pi a_0^3}{Z}\Delta_i|\psi(0)|^2 f(r) \quad , \tag{1.48}$$

where a_0 is the Bohr radius, Z is the atomic number, $f(r)$ is the nuclear form factor and $\Delta|\psi(0)|^2$ is the change in the electronic density between the states of the transition. It is clear from Eq. (1.47) that a measurement of the isotope shifts across a chain of isotopes can yield the change in their mean square charge radii.

In recent relativistic calculations on the isotope effect [TSC 03] the field isotope shift between two isotopes have been determined by

$$\delta E_{FS} = \left\langle \psi | \sum_i \delta V_N(r_i, R) | \psi \right\rangle \quad , \tag{1.49}$$

where

$$\delta V_N(r) = V_N(r, R+\delta R) - V_N(r, R) \quad , \tag{1.50}$$

and δR is the difference of the root-mean-square (rms) nuclear charge radii ($R = \left\langle r^2\right\rangle^{1/2}$) for the two isotopes. Here, the nuclear charge distributions $\rho(r', R)$ was assumed to follow the Fermi model [PTF92]

$$\rho_{Fermi}^{nuc}(r) = \frac{\rho_0}{1+e^{(r-c/a)}} \quad , \tag{1.51}$$

where c is the radius at which $\rho^{nuc}_{Fermi}(r) = \rho_0/2$, and a is the skin thickness. Then, the potential of the extended nucleus is expressed by

$$V_N(r,R) \quad = \quad -4\pi\alpha Z \int_0^\infty dr' r^2 \rho(r',R) \frac{1}{r_>} \quad , \quad r_> = max(r,r') \ . \tag{1.52}$$

This potential shape is used in the Dirac-Coulomb-Breit Hamiltonian to obtain the relativistic electronic wave functions in [TSC 03]. If the nuclei are spherically symmetric and if an approximate $\mathrm{A}^{1/3}$ law of radius holds, then the fractional increase of radius is just $\delta\mathrm{A}/3\mathrm{A}$, and the difference of the mean-square nuclear radii can be expressed by

$$\delta \left\langle r^{2\sigma} \right\rangle = (2\sigma/3)\,(\delta A/A) \left\langle r^{2\sigma} \right\rangle \quad , \tag{1.53}$$

where $\sigma = \left[1 - (\alpha Z)^2\right]^{1/2}$ and $\langle r^2 \rangle$ is averaged over the radius and angle. From knowledge of the regular variation of nuclear deformation one can find the magnitude of the isotope shift corresponding to an equivalent uniform distribution of radius

$$R_{eq} = \left[\frac{5}{3}\left\langle r^2 \right\rangle\right]^{1/2} \quad , \tag{1.54}$$

which by means of measurements of the optical shift [FH55] was found to be

$$R_{eq} = (0.90 \pm 0.1) \times 10^{-13} A^{1/3} cm \ \ , \tag{1.55}$$

appreciably too small to agree with the results obtained in μ-meson or electron-scattering experiments [FR53,HFM53]. The explanation offered by Wilets [WHF53] was that the nuclear density is not a constant but depends slightly on the neutron-proton ratio. When a neutron is added to a nucleus, the nuclear density increases slightly as a result of the diminished Coulomb energy, and the resultant fractional increase of radius is less than $(1/3A)$. The isotope shift is consequently smaller than for constant density nuclei, which was the erroneous assumption which led to the anomalously low radius given by Eq. (1.54).

Another possible contribution to the isotopic shift can be caused by the polarization, *i.e.*, the virtual excitation, of the nucleus by the electrons. This effect may be interpreted in terms of admixtures to the nuclear ground state of low-lying excited levels, in such a way as to give greater concentration of protons toward the center of the nucleus where the electron probability density is greatest. Contributions arising from the nuclear polarization [BAC50], as well as those due to the intrinsic magnetic moment of the electron were first pointed out by Breit and his student Clendenin [BC52]. Recent calculations of the nuclear polarization correction in heavy systems were performed by [NLP 96, PMG 89].

Chapter 2

Optical emission from an Electron Beam Ion Trap

An electron beam ion trap (EBIT) at the Max-Planck-Institute für Kernphysik (MPIK) in Heidelberg has been used to produce and trap highly charged ions for in situ spectroscopic observation. The machine design has originally been developed for x-ray spectroscopy measurements of the trapped ions. With the subsequent addition of visible (VIS), ultraviolet (UV), and vacuum ultraviolet (VUV) spectrometers, high-resolution observations of spectral emission lines from a few eV to several tens of keV (up to 100 keV) are now possible.

2.1 Principle and applications

The electron beam ion trap, schematically shown in Fig. 2.1, is a very convenient tool if one wants to study highly charged heavy elements with only a few electrons left [Gil01]. One of its advantages is the minimization of the Doppler shift due to typically slow motion of the ions along the line of sight in the trap. It is possible to produce ions with a relatively narrow charge state distribution under excitation by a nearly mono-energetic electron beam and, thus, it is a powerful source for emission spectroscopy. By allowing high precision measurements, higher order effects due to various interactions among the nucleus, the electrons, and the electromagnetic field, such as QED effects can be studied in detail.

The device consists of three main assemblies: an electron gun, a trap region and a collector. In the electron gun, electrons emitted from a negatively biased cathode are accelerated towards the trap region, which is positively biased with respect to the laboratory ground potential. The accelerated electron beam is compressed by a strong axial magnetic field. To achieve such a high field, two pairs of superconducting coils, cooled down to 4.2 K with liquid helium, are used. At this low temperature, the trap itself becomes a very efficient cryo-pump, helping to produce the required vacuum (10^{-13} torr) in the trap region to prevent charge exchange effects causing losses of the trapped ions (see Fig. 2.1).

After passing through the trap region, the electrons are decelerated as they approach the collector electrode which is biased at the same potential as the cathode. The magnetic field strength is reduced towards the collector resulting in a re-expansion of the focused electron beam. Finally, the electron beam with a kinetic energy of the order of 1 keV is stopped at the collector electrode.

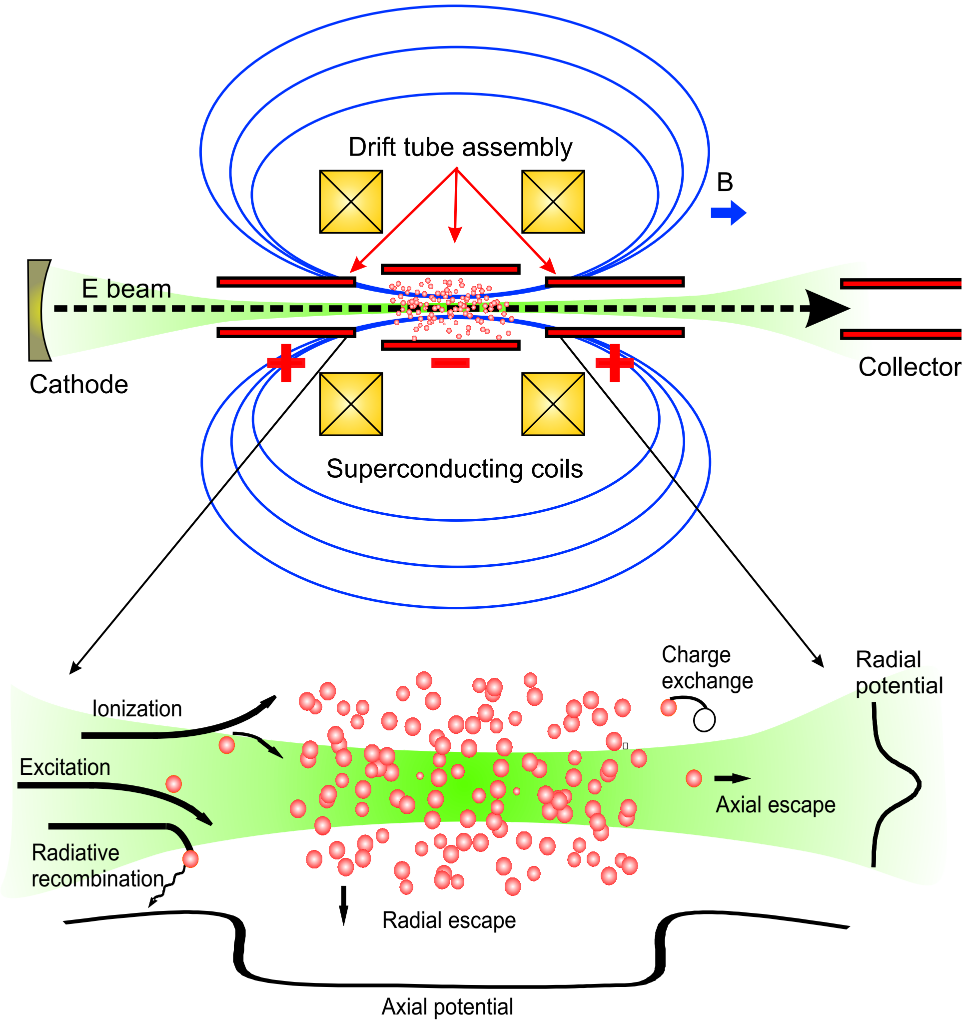

Figure 2.1: A schematic diagram of the principle of an EBIT and some of the processes occurring inside the trap.

The radial trapping of the ions is provided by the negative space charge potential of the compressed electron beam. The axial trapping is generated by applying appropriate voltages to the drift tube electrodes, which can be biased independently. Thus, different trap configurations can be chosen for specific purposes. In such a way, a shallow trap is used when cold ions are required, and a deep trap when the ion temperature is less important.

There are a few EBITs worldwide. The first one was built at the Lawrence Livermore National Laboratory (LLNL) [MLK 88], where also the second one, called Super-EBIT [MEK94], was later constructed allowing higher electron beam energies and currents (up to 200 keV and 200 mA, respectively). Based on these models, two more machines were built at the National Institute of Standards and Technology (NIST) [Gil97] and at Oxford University [SVM 94]. Another slightly modified copy is the Berlin EBIT [BFF 97]. There is a new EBIT at Stockholm University [Uni05]. High-energy EBITs are currently working at LLNL, at the University of Electro-Communication in Tokyo [CAI 96], at the Institute of Modern Physics in Shanghai and at the MPI für Kernphysik in Heidelberg. There also exists a compact EBIT using a permanent magnet at the Forschungszentrum Rossendorf in Dresden. Two more EBITs are under construction at the MPI in Heidelberg, which will be used at the ISAC facility at TRIUMF (Vancouver), and at the Tesla test facility laboratory in Hamburg, respectively.

2.1.1 Atomic collisional processes

The ions in an EBIT are produced by successive electron impact ionization events from either low charge state ions or neutrals that are introduced into the trap. A detail understanding of the atomic physics processes occurring in the trap is essential for the analysis of the ion charge balance inside and the radiation emitted from the trap.

An *excitation process* from a level nl to a level $n'l'$ is possible only if the collision energy exceeds the necessary threshold energy. The collision reaction reads

$$A^{q+}(nl) + e^- \longrightarrow \left[A^{q+}\left(n'l'\right)\right]^* + e^- \quad , \tag{2.1}$$

where q is the ions charge state. The excited ion is stabilized usually by emitting a photon with specific energy, by a photon cascade, or by an Auger process. The electron impact *ionization* (EI) is the dominant ion production process in most plasmas. The most simple process of which is direct single ionization,

$$A^{q+} + e^- \longrightarrow A^{(q+1)+} + 2e^- \quad . \tag{2.2}$$

Electron *recombination* take places when an electron is captured into a bound state of an ion. If a single photon is released, the process is called *radiative recombination* (RR),

$$A^{q+} + e^- \longrightarrow A^{(q-1)+}(nl) + h\nu \quad . \tag{2.3}$$

Another type of recombination may also occur through a resonant process called dielectronic recombination (DR),

$$A^{q+} + e^- \longrightarrow A^{**(q-1)}(nln''l'') \longrightarrow A^{(q-1)+}(nl) + h\nu \quad . \tag{2.4}$$

These two processes (RR and DR) are studied and described in the context of EBITs in more detail by González Martínez in [Gon05].

When an ion captures one or several electrons from a neutral atom the charge exchange process take place:

$$A^{q+} + B \longrightarrow A^{(q-p)+}(n^1l^1, n^2l^2, ..., n^pl^p) + B^{p+} \quad . \tag{2.5}$$

This process results in the stepwise lowering of the charge state, and eventually in the loss of HCI. While neutrals may affect strongly the charge balance, in an EBIT, charge exchange between highly charged ions is very unlikely and can be ignored in most cases, due to their low kinetic energies and the strong Coulomb repulsion between them.

The rate of change of the number density of a particular charge state is coupled to the number density of its neighboring charge states through the previous processes (ionization, excitation, recombination and charge exchange) [PBD 91].

2.1.2 The Heidelberg EBIT

The main difference between the Heidelberg design and all other EBITs essentially being of the Livermore type is its horizontal arrangement, as shown in Fig. 2.2.

Moreover, it has two thermal shields in order to reduce the liquid helium consumption and, thus, the running costs. Besides, these shields provide an efficient differential pumping providing an enhancement of the vacuum quality. The reason for this horizontal design is to facilitate simple extraction of ions, which, for instance, can be transferred into a *reaction microscope* [KSM 97] to study collisions involving slow highly charged ions with atoms, and molecules [UMD 03] as well as to other experiments for ion-surface interaction studies.

The magnetic field strength can be as high as 9 T. This highest field can be reached by cooling the super conducting (SC) magnet down to 2.2 K by means of a Lambda-plate refrigerator. Such a strong field compresses the electron beam diameter down to below 50 μm. Due to the high electron beam energy and current, combined with the excellent vacuum conditions, it has already been possible to produce a broad variety of highly charged ions, as for instance Ar^{18+}, Kr^{36+}, Xe^{54+}, ... Hg^{78+}.

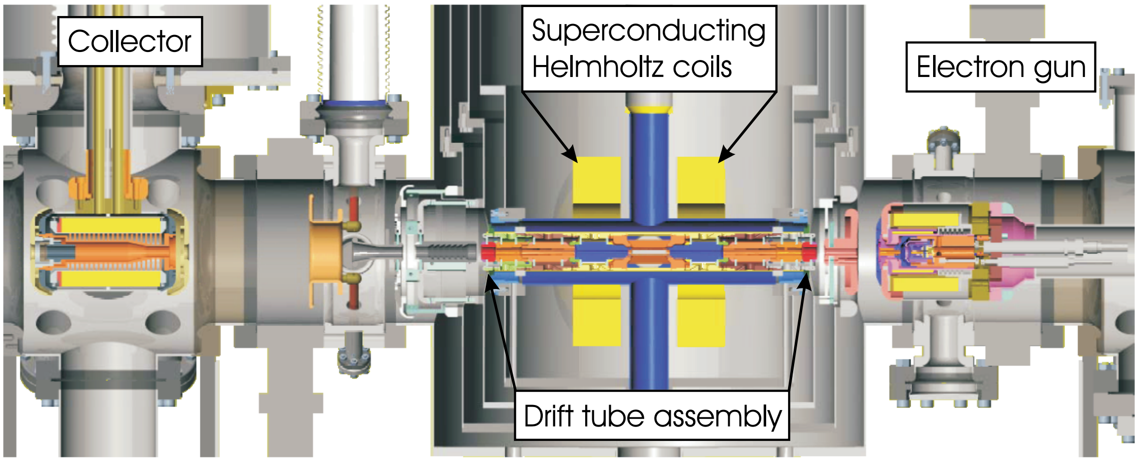

Figure 2.2: The horizontal design of the Heildelberg EBIT.

Electron gun

The main parts of the electron gun are a thermoionic cathode, a focus and an anode electrodes, respectively. The cathode, which uses a dispenser of barium oxide, has a spherical-concave shape (Pierce geometry) which produces well-defined beam profiles and a smoother beam-waist than other commonly used cathode designs [CBM 04]. The focus electrode controls the emission current and compensates the edge effects of the cathode field. To accelerate the electrons emitted from the cathode, a tubular anode electrode is used. Proper tuning of the potentials applied to these two electrodes (focus and anode) improves the focusing, and thus, the beam intensity and quality.

The effect of a residual magnetic field at the cathode surface, which is to limit the minimum diameter achievable under a given B_{MAX} at the trap center, is minimized by means of a so-called bucking coil, which surrounds the electron gun. A proper tuning of the magnetic field at the cathode surface by means of this coil minimizes the diameter of the electron beam in the trap region (see below). The picture of the electron gun, shown in Fig. 2.3, displays these and other important parts as the trimming coil, which are used to tune the beam.

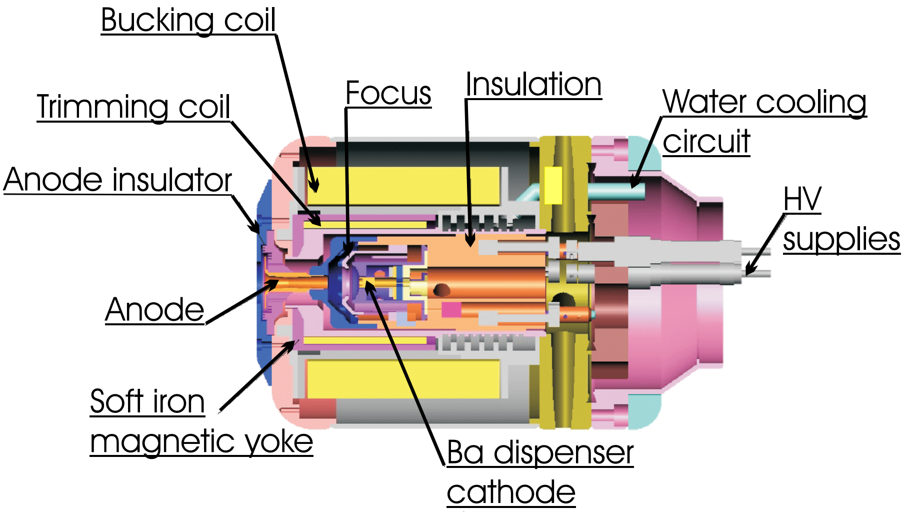

Figure 2.3: Electron gun assembly.

Trap, electrodes and magnet

Two superconducting coils are mounted in a Helmholtz configuration around the trap region. The trap region consist of nine electrodes called *drift tubes* (DT). These electrodes have different cylindrical shapes, with a radius decreasing towards the direction of the central trapping region. The middle one is 40 mm long and has a 5 mm inner radius (r_{dt}). The neighbouring electrodes are 55 mm, 56 mm, 27 mm and 15 mm long, respectively. This distribution is symmetrical on both sides of the central drift tube. By applying appropriate voltages to these electrodes, various trap configurations with a length varying from 40 to 350 mm can be formed. The central DT has four elongated apertures allowing optical access to the trapped ions. Depending on the experimental goal, ports with optical lenses for laser or visible spectroscopy, or beryllium windows for x-ray experiments are used. The port under the trap region is used for the neutral gas injection (see below).

In Fig. 2.4 the main vacuum chamber containing the two thermal shields cooled with a cryogenic system is shown. The outer shield operates at about 50 K. The second thermal shield lies at temperature of about 16 K. This shield surrounds the cryostate, which is filled with liquid He at 4.2 K, and contains the superconducting coils. Hence, the pressure in the trap region is estimated to be as low as 10^{-13} Torr.

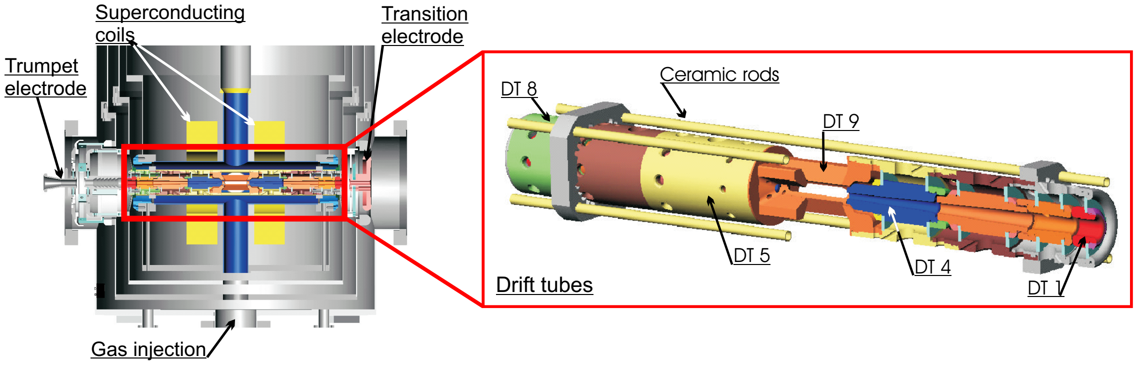

Figure 2.4: The main vacuum chamber with, on the right, an enlargement of the setup for the drift tubes. In DT9, the central drift tube, there are four rectangular apertures for optical access.

Just in front of the drift tubes, the so-called transition electrode is located. A good guiding of the electron beam from the electron gun through the drift tubes to the collector without hitting the electrodes is very important. Two pairs of small magnetic coils (steering magnets) mounted outside the vacuum chamber are used to steer the electron beam and reduce current losses.

In this experiment, the trap is continuously loaded with neutral gas atoms by means of an atomic beam. It is periodically dumped to avoid the slow accumulation of high-Z ion impurities by applying a positive voltage to DT9. As an example, for argon a typical cycle lasts a few seconds.

Electron collector

The purpose of the electron collector is to slow down and stop the electron beam after it has passed the trap. It consists of a water-cooled collector electrode and additional electrodes called suppressor and extractor, and it is surrounded by a magnet coil. This coil (see Fig. 2.5) compensates the residual axial magnetic field of the SC magnet allowing the electron beam to expand and hit the collector wall. In order to prevent the secondary electrons produced here from escaping back into the trap, a suppressor electrode biased negatively with respect to the collector is used. The extractor electrode is used to extract ions from the electron beam. This electrode has a negative potential applied in order to stop the electrons from leaving the collector through its rear aperture. The collector is cooled with water to remove the heat produced by the electron beam.

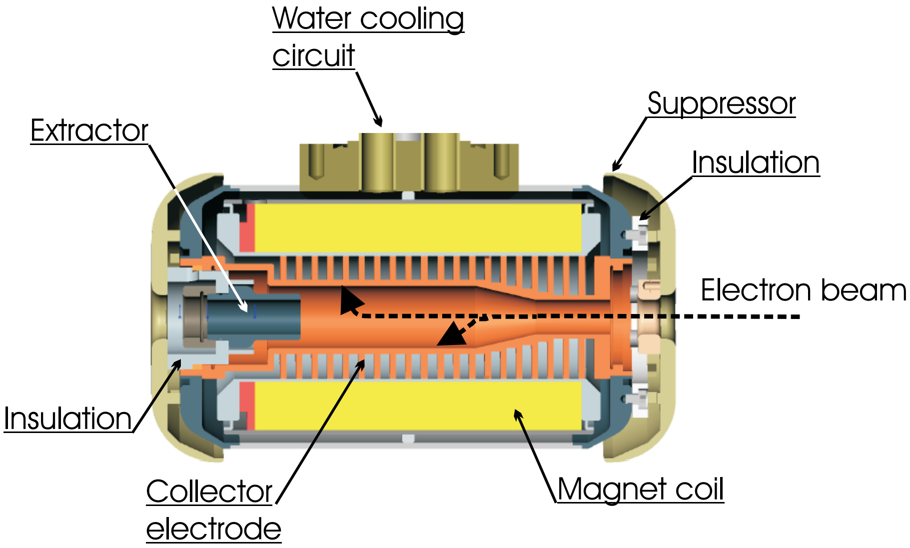

Figure 2.5: Sketch of the electron collector.

Gas injection

An atomic beam is injected into the trap by means of two differential pumping stages. This system lets only ballistic molecules pass through the two stages, producing a narrow slit-shaped atomic beam and, hence, less atoms can contaminate the main tank vacuum. Atoms or molecules in the gas phase (Ne, Ar, Kr, Xe, Cl_2, UF_6, Hg,...) can be injected in this way. It has to be mentioned that barium and tungsten ions evaporated from the cathode material are always present in the trap.

In order to regulate the gas injection, a needle valve connected to the gas supply is controlled thermally. The gas pressure, monitored by ionization gauges, is about 10^{-8} Torr in the first stage (see Fig. 2.6).

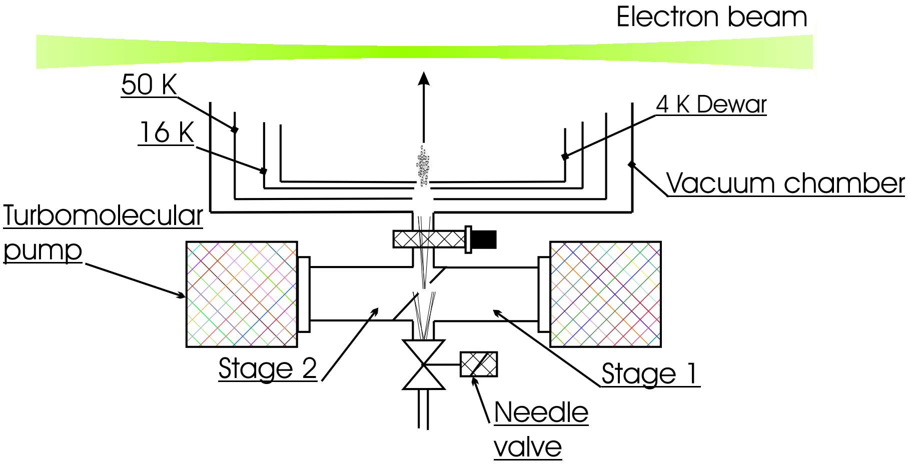

Figure 2.6: The two-stage differentially pumping gas injection system.

2.2 Properties of the electron beam

The optimum operation of the EBIT depends on a proper tuning of the electron beam. While the electron beam energy (E_e) determines the ion charge state, the ionization rate depends on the electron beam current (I_e). For a given current, a smaller beam diameter means a higher electron density and, thus, shorter ionization times and higher excitation rates. The diameter and position of the electron beam depend mainly on the field strength of the superconducting magnet, but it is also affected by the operation of the bucking coil and the steering magnets.

2.2.1 Electron beam radius

A rigorous calculation of the electron beam radius, r_H, performed by Herrmann [Her58], based on a non-laminar electron beam of cylindrical shape, and also taking into account the thermal motion of the electrons, yields

$$r_H = r_B \sqrt{\frac{1}{2} + \frac{1}{2}\sqrt{1 + 4\left(\frac{8 m_0 k_B T_c r_c^2}{e^2 r_B^2 B^2} + \frac{B_c^2 r_c^4}{B^2 r_B^2}\right)}} \, , \tag{2.6}$$

which contains the contribution of the cathode properties, namely its radius r_c, the magnetic field strength on its surface B_c and its temperature T_c. k_B is the Boltzmann constant and e is the elementary charge. r_B is a fictitious value of the radius of an ideal electron beam, obtained using the Brillouin theorem [Bri45]. This theorem does not take thermal effects into consideration and, for a laminar electron flow, propagating in an uniform axial field B in terms of the electron beam current I_e, the electron speed v_e and the electron mass m_0, yields a radius r_B of

$$r_B = \sqrt{\frac{2m_0 I_e}{\pi\epsilon_0 v_e e B^2}} \ , \tag{2.7}$$

where ϵ_0 is the permitivity of the vacuum. In Fig. 2.7a the calculated dependency of the electron beam radius r_H as a function of the electron beam current is shown. The Herrmann radius is plotted as a function of the electron beam energy E_e in Fig. 2.7b as well. Here, we can see that r_H does not change significantly with E_e.

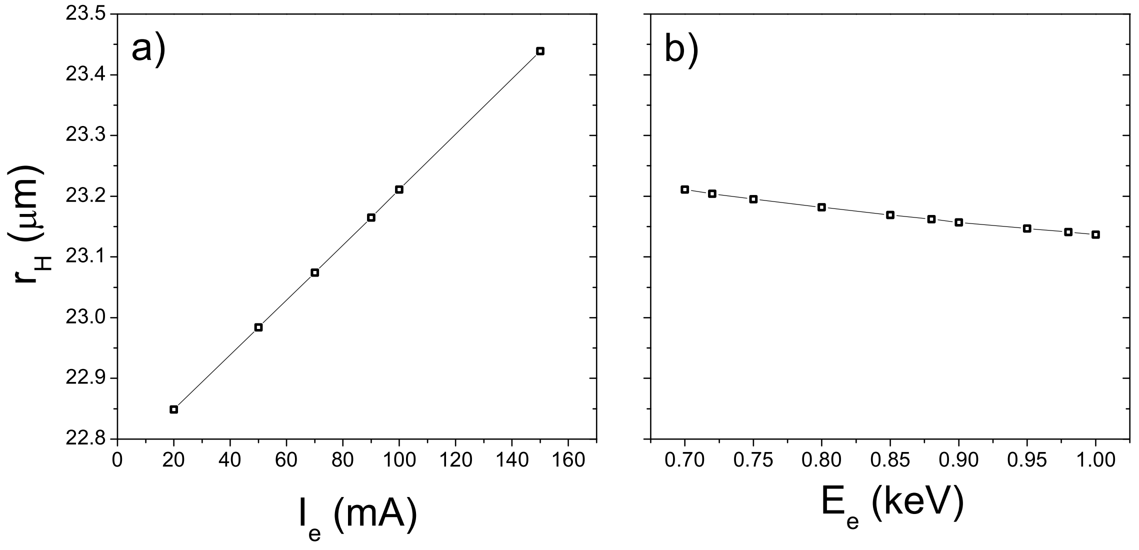

Figure 2.7: The electron beam radius r_H as a function of a) the electron beam current I_e and b) the electron beam energy E_e at $B = 8$ T.

The magnetic field on the surface of the cathode B_c has to be minimized to optimize the laminar flow of the electron beam [Her58]. This is achieved by a combination of the bucking coil, the trimming coils and the superconducting magnet. The strong influence of the bucking coil on the beam radius has been measured by Utter [UBC 99] in the EBIT at LLNL in Livermore. There, the electron beam image was obtained by observing x-rays emitted by the trapped ions with a pinhole camera and a position sensitive detector. At a field of 3 T, the beam diameter could be modified from 40 μm to 80 μm by changing the bucking coil current from 0.95 A to 1.20 A. However, the compression of the electron beam radius is essentially caused by the axial magnetic field as is shown in Fig. 2.8.

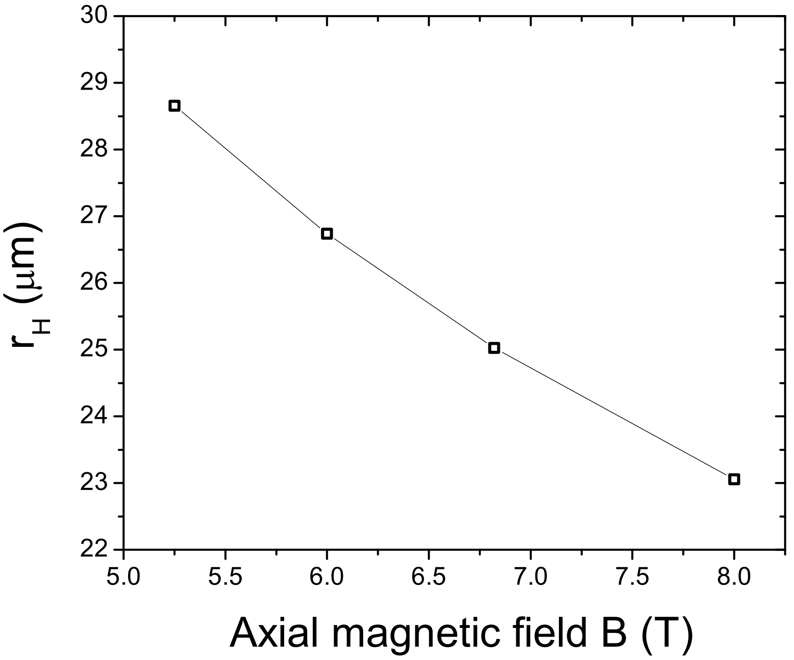

Figure 2.8: Electron beam radius as a function of the axial magnetic field for a beam energy $E_e = 0.7$ keV and a beam current $I_e = 50$ mA calculated with Eq. (2.6).

2.2.2 Radial space charge potential

The electron charge density generates a space charge potential V_{sp} which must be taken into account to know the actual acceleration voltage. The electron beam is assumed to have a flat uniform profile distribution along the radial direction within its radius r_e, and to flow along the axis of a drift tube with a radius r_{dt} [Gil01]. Under the boundary conditions that the space charge potential is zero at the drift tube wall and steady at the electron beam edge $r = r_e$, the V_{sp} is given by

$$V_{sp}(r \leq r_e) = \frac{I_e}{4\pi\epsilon_0 v_e}\left[\left(\frac{r}{r_e}\right)^2 + \ln\left(\frac{r_e}{r_{dt}}\right)^2 - 1\right] , \tag{2.8}$$

$$V_{sp}(r \geq r_e) = \frac{I_e}{2\pi\epsilon_0 v_e}\ln\left(\frac{r}{r_{dt}}\right) , \tag{2.9}$$

where v_e is the electron velocity. At the drift tube center, $r = 0$, the radial space charge potential can be calculated using the following approximation

$$V_{sp}(0)[V] \approx \frac{30 I_e\,[A]}{\sqrt{1-\left(\frac{E_e[keV]}{m_0c^2}+1\right)^{-2}}}\left[\ln\left(\frac{r_e}{r_{dt}}\right)^2-1\right] \quad , \tag{2.10}$$

with the electron speed expressed as $v_e = c\sqrt{1-(E_e/m_0c^2+1)^{-2}}$, and the electron mass $m_0c^2 = 511$ keV. A reduction of the electron beam radius produces an increase of the radial space charge potential. In Fig. 2.9 the calculated space charge potential V_{sp} is plotted versus the electron beam energy for different electron beam currents, showing how it changes linearly with the electron beam current at a given electron energy. For instance, and for an electron beam radius of 29 μm at $E_e = 0.7$ keV the space charge potential is calculated to be $V_{sp} =$ - 128 V at $I_e = 20$ mA and - 645 V at 100 mA, respectively.

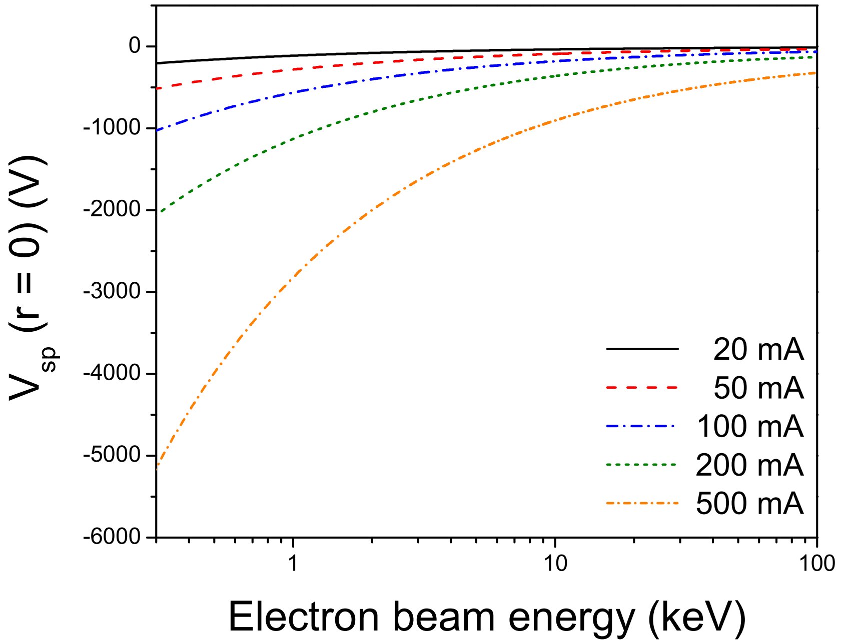

Figure 2.9: Space charge potential at the electron beam center as a function of the electron beam energy E_e for different electron beam currents.

However, the effective radial space charge potential due to the electron beam (negative) is reduced when highly charged ions (positive) are accumulated in the trap. Therefore, an additional factor f, the so-called compensation factor, has to be taken into account. It is defined as

$$f = \frac{\sum n_q q}{n_e} \quad , \tag{2.11}$$

where n_q is number density of ions with the charge q and n_e the negative (electron) charge density, within the electron beam volume of interest [Wid98]. The electron density n_e can be determined by assuming that the distribution of the transversal thermal velocities of the electrons follows a Gaussian function. Its radial dependence is written as

$$n_e(r) = n_{e0} e^{-\frac{r_e^2}{2\sigma_r^2}} \quad , \tag{2.12}$$

where the maximum n_{e0} and the width σ_r (the geometrical cross section) of the Gaussian beam charge distribution are given by

$$\begin{aligned} n_{e0} &= \frac{I_e ln5}{\pi r_b^2 v_e} \quad , \\ \sigma_r^2 &= \frac{r_b^2}{2ln5} \quad . \end{aligned} \tag{2.13}$$

Using these definitions, the beam radius r_b encloses 80 % of the total charge.

We finally obtain an expression for the actual beam energy E_e including the space charge effects

$$E_e = -V_{cathode} + V_{dt} - V_{sp}(1-f) \quad . \tag{2.14}$$

To determine the still unknown f, one observes the appearance and/or disappearance of some characteristic spectral feature or signal due to certain charge state X^{q+}. In order to produce that charge state, the electron beam needs an energy at least as high as the ionization potential of the $X^{(q-1)+}$ ion, $I_P^{(q-1)+}$.

By recording $V_{cathode}$, V_{dt} (and in some cases the additional acceleration voltage applied to the whole electron gun) and observing the threshold behavior of the chosen feature, the value of f can be obtained by means of Eq. (2.14), when $E_e = I_P^{(q-1)+}$.

2.2.3 Axial space charge potential

Due to the different radii of the drift tubes along the beam axis, a variable axial space charge potential V_{sp}^{ax} is inherently generated along the electron beam propagation in addition to the radial one. This produces a trapping potential along the drift tube electrodes, which can be approximately calculated as the difference between the radial space charge potential of the two neighboring electrodes, $V_{sp}^{ax} = V_{sp}^{dt_i} - V_{sp}^{dt_{central}}$. Here dt_i represents the radius of the drift tubes next to the the central drift tube $dt_{central}$. In our case $r_{dt_{central}} = 5$ mm and $r_{dt_i} = 1.5$ mm. With these parameters, the axial space charge potential difference between the central and neighboring electrodes is:

$$V_{sp}^{ax}\,[V] = \frac{72.24\,I_e\,[A]}{\sqrt{1 - \left(\frac{E_e[keV]}{511} + 1\right)^{-2}}} \quad . \tag{2.15}$$

In order to illustrate the importance of this effect, a simulation of the electrostatic potential along the $r = 0$ axis (under the assumption that all drift tubes are grounded) caused by an 0.7 keV, 50 mA electron beam is shown in Fig. 2.10. Under those conditions, the axial space charge potential generated is $V_{sp}^{ax} = 69$ V, which even without any external voltage applied to the drift tubes is sufficient to trap ions.

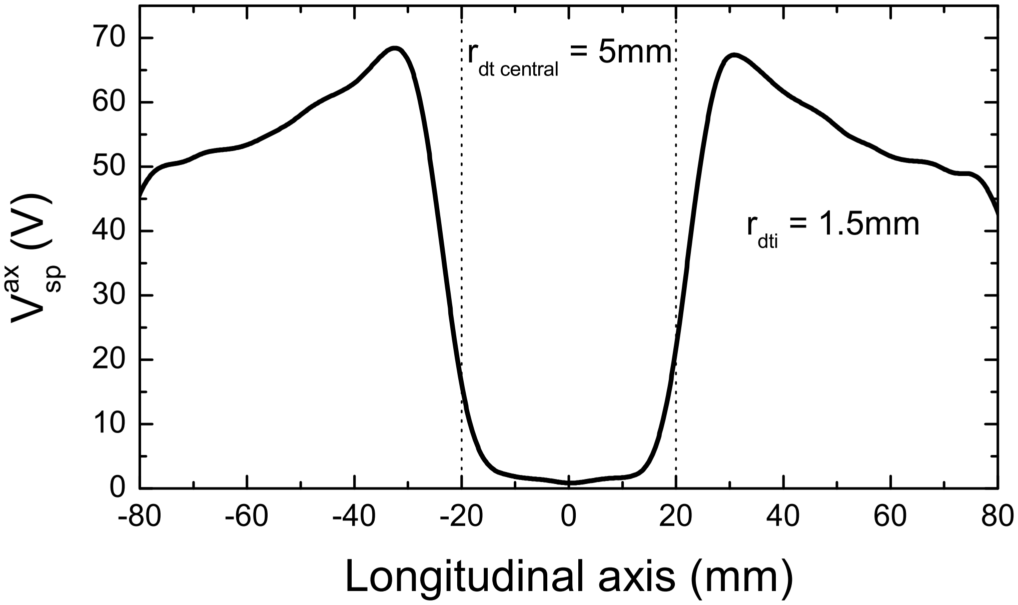

Figure 2.10: Simulation of the axial space charge potential in the trap region for 0.7 keV and 50 mA electron beam energy and current, respectively.

2.2.4 Heating and cooling mechanisms

Most of the electron-ion collisions in an EBIT result in the transfer of a small random amount of kinetic energy to the ions. Thus, despite of the large difference in the masses of ions and electrons, the ion population is heated up by the electron beam. Changing their charge state during an ionization process, ions can gain kinetic energy depending on their electrostatic potential at the position where ionization took place. Among the different processes which may contribute to the heating of the ions, the collisional heating dominates in the EBIT. The heating rate dE_q/dt is given by

$$\frac{dE_q}{dt} = \frac{0.442 q^2 2 j_e n_q \ln(P_m/P_0)}{A E_e} \quad (eV/sec \cdot cm^3) \ , \qquad (2.16)$$

where A is the ion mass (in atomic units), P_0 and P_m are the minimum and maximum ion-electron impact parameter, respectively, q is the ion charge and n_q denotes the number density of q times ionized ions [LMH 88]. The expression $\ln(P_m/P_0)$, denoted as $\ln(\Lambda)$, is usually called the *Coulomb logarithm*, and typically has a value of the order of 10.

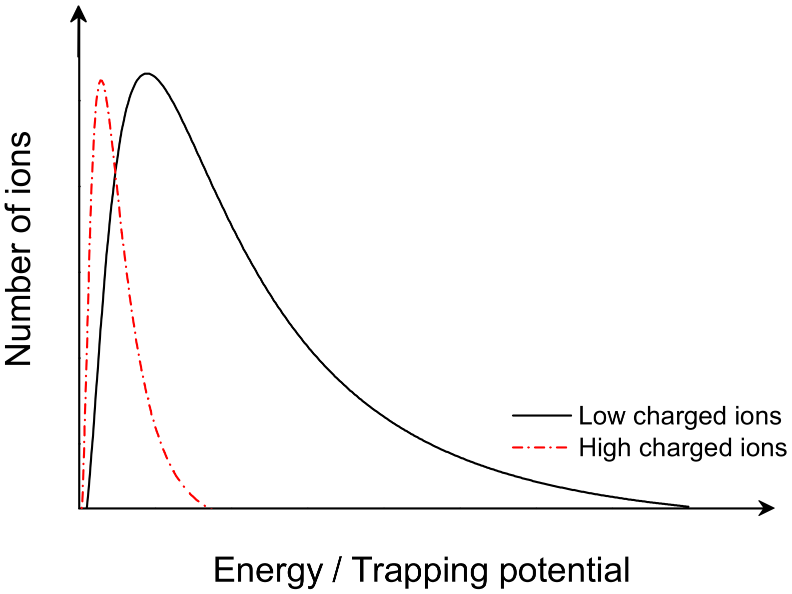

Figure 2.11: Evaporative cooling of highly charged ions by an admixture of low charged ions.

This continuous heating would eventually result in all ions leaving the trap. In order to counter act the heating, an appropriate cooling mechanism is needed. Evaporative cooling is used for this purpose in EBITs [LMH 88]. It basically consists in the cooling of the HCIs of interest by ion-ion collisions with lighter ions in somewhat lower charge states (see Fig. 2.11). This process is deliberately enhanced by introducing a light element, typically Ne or N_2 into the EBIT. Its atoms are rapidly ionised to their bare state and quickly thermalize with the heavier ions by collisions. Their lower maximum charge state implies a lower effective trapping potential and, thus, they can evaporate from the trap more easily. In this way, the light element efficiently cools the HCIs under study. Other techniques developed for this purpose are pulsed evaporative cooling [KCO99] and sympathetic cooling [MFR 01].

In the present experiment, the first factor studied with respect to the ion temperature was the electron beam energy. In Fig. 2.12 a decreases in the width of the observed emission line (see section 3.5.2) can be seen while lowering the beam energy. So, by reducing the electron beam energy but keeping it high enough to produce the desired charge state the temperature of the trapped ions is decreased.

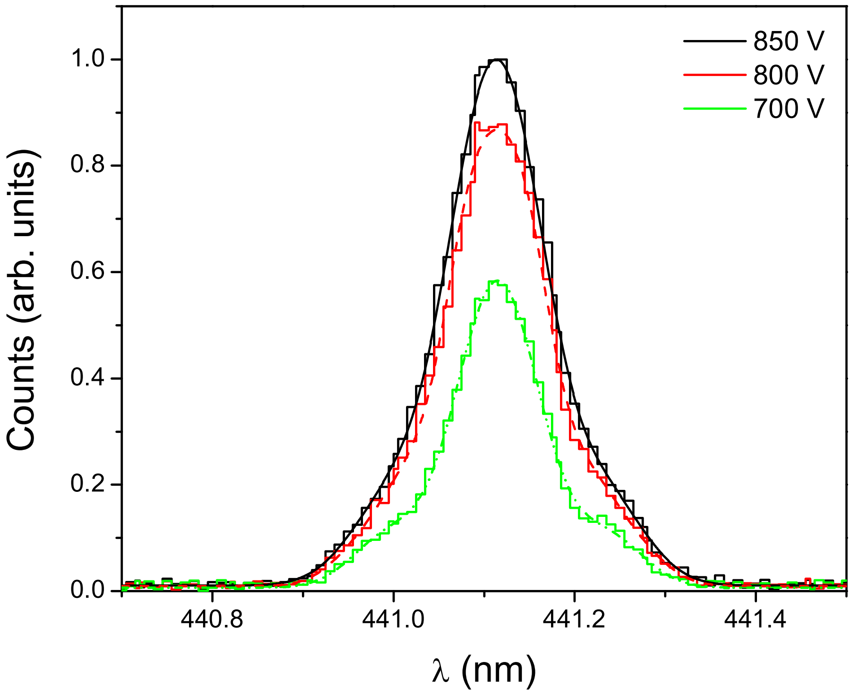

Figure 2.12: Profile of the emission line from the $^2P_{3/2} - ^2P_{1/2}$ transition in Ar^{13+} for different electron beam energies (non-calibrated wavelength scale).

The next factor which helps in reducing the temperature is simply realized by lowering the external axial trapping potential, thereby controlling the evaporation rate. Thus, the Doppler broadening was reduced as well, as shown in Figs. 2.13a and b, respectively, for two different E_e values.

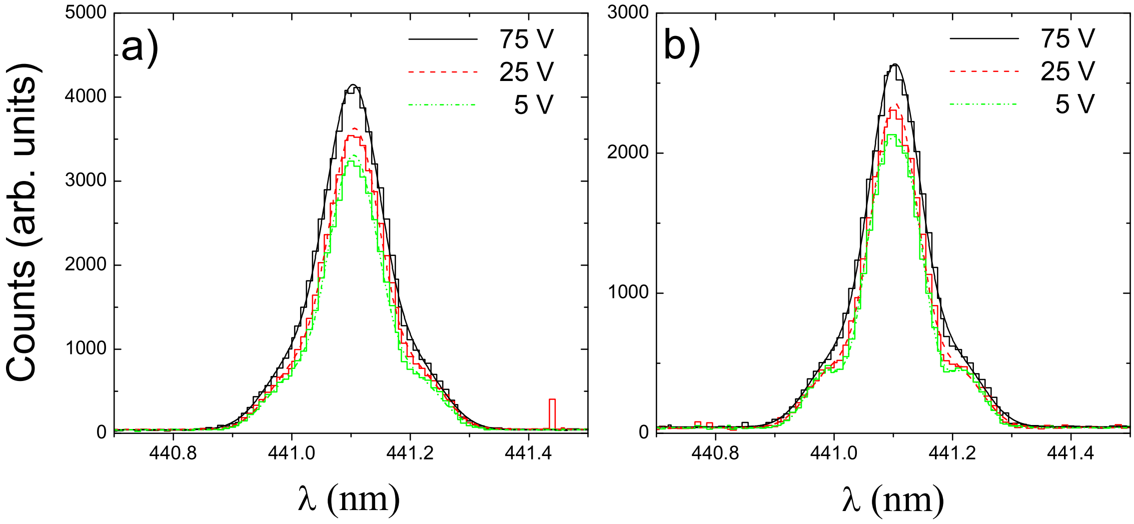

Figure 2.13: Profile for the emission line from the $^2P_{3/2} -^2 P_{1/2}$ transition in Ar^{13+} at a) 800 eV and b) 700 eV electron beam energy (I_e = 100 mA and 70 mA, respectively) for different external axial trapping potentials, *i.e.*, drift tube voltages (non-calibrated wavelength scale).

For the present experiments ion cooling is very important, since the Zeeman splitting of the fine structure $^2P_{3/2} -^2 P_{1/2}$ transition in Ar^{13+} is very small and can only be resolved at low temperatures. The accuracy of the wavelength measurement can also be increased with narrower lines. For this purpose, the electron beam current was varied as well, looking for the best conditions (see Fig. 2.14).

Moreover, by increasing the gas injector pressure the neutral atom density in the trap increases. The ion production rate increases accordingly, and more light ions can be evaporated. Enhanced evaporative cooling leads to ion temperature reduction and, thus, to a narrowing of the spectral width of the emission lines, as shown in Fig. 2.15.

A systematic optimization of the evaporative cooling allowed us finally to achieve a FHWM of only 0.013(1) nm, for the HCI forbidden lines. After correcting for the apparatus profile of the spectrometer, this Doppler broadening of the line implies ion temperatures as low as 6(1) eV. The ion temperatures of 60 eV, in an EBIT, reported by Beiersdorfer [BOD 96] had enabled very high resolution x-ray measurements. In our experiment, the achieved temperature is even lower and helped to carry out the present wavelength measurements, which have the highest accuracy ever reported for HCI.

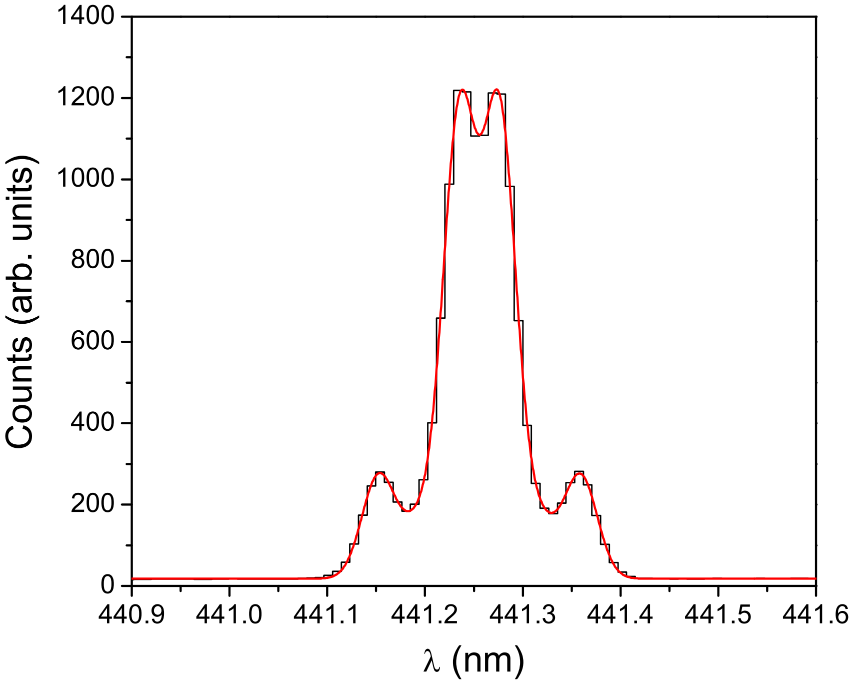

Figure 2.14: Resolved Zeeman splitting spectrum of the fine structure $^2P_{3/2} -^2 P_{1/2}$ transition in Ar^{13+} for E_e = 700 eV, V_{dt} = 0 V and I_e = 50 mA.

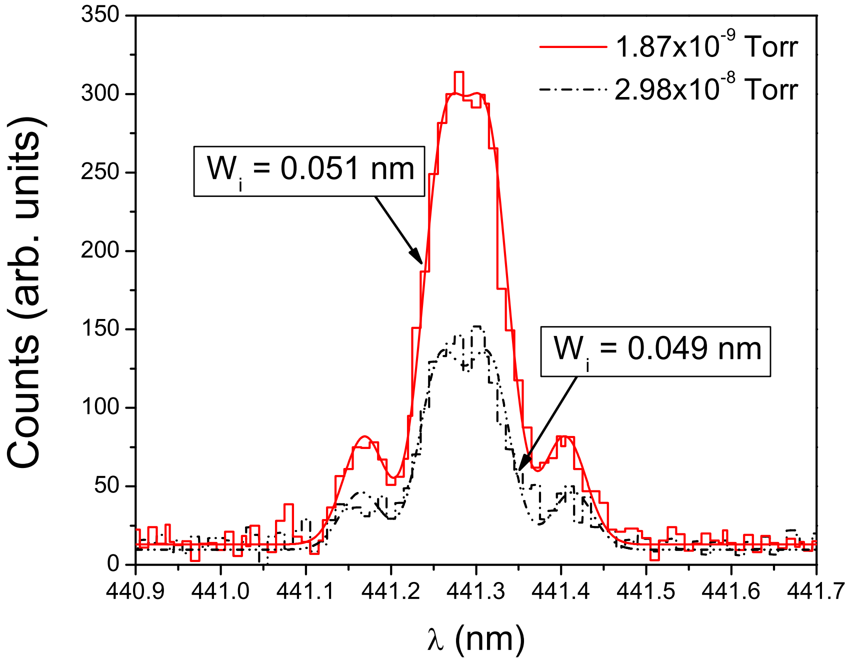

Figure 2.15: Reduction of the spectral line width of the emitted light for two different injector gas pressures (non-calibrated wavelength scale).

Chapter 3

Experimental setup

Spectroscopic observations in an EBIT require always the use of very sensitive instrumentation. The low number of trapped ions (10^5 to 10^7 typically), the reduced solid angle subtended by spectrometers (10^{-3} to 10^{-8}) as well as the small excitation cross sections imply in many cases that long observation times are necessary to acquire sufficient statistical significance. Under these circumstances, detector noise becomes also a central issue.

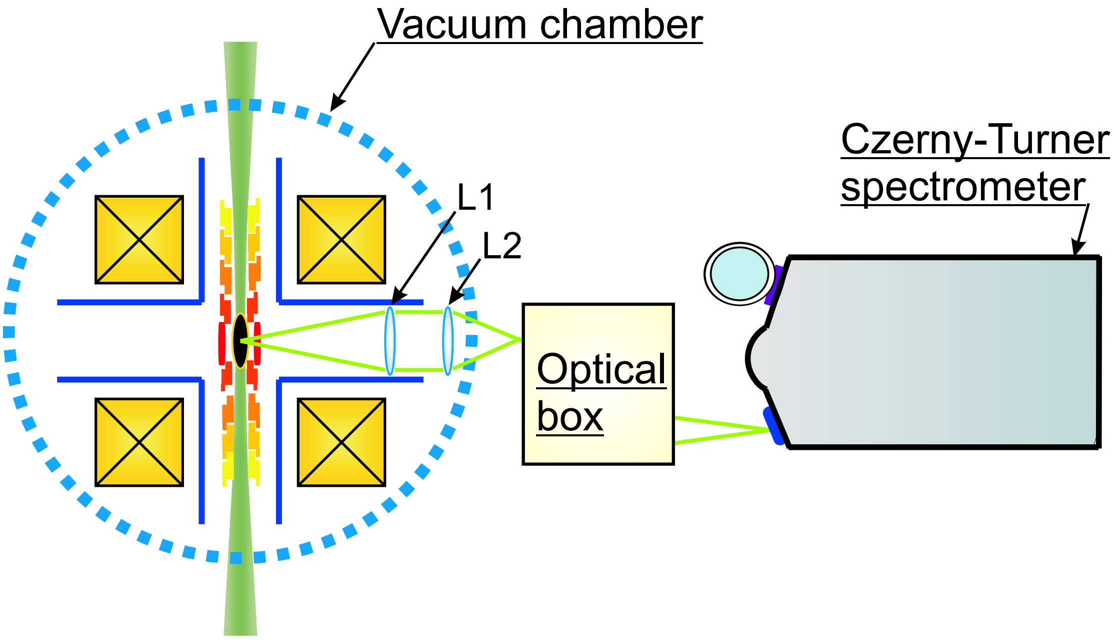

Figure 3.1: Sketch of the set up used in this experiment. Two quartz lenses (L1, L2) are installed inside the main vacuum chamber. Outside the EBIT, the light passes through an optical system into the Czerny-Turner spectrometer.

]

In the present experiment, the observation of the visible forbidden lines produced in the EBIT has been carried out using a Czerny-Turner spectrometer equipped with a cryogenically cooled charge coupled device (CCD) camera. Since the ion cloud in the EBIT has a horizontal shape (40 mm length × 0.3 mm diameter, roughly), it is convenient to rotate its image in order to increase the amount of light going through the vertically arranged spectrometer slit by means of an optical system consisting of mirrors and lenses (see Fig. 3.1). This setup was enclosed in a box mounted onto the same table as the spectrometer and fixed to it to prevent any relative motion. The data acquisition and the spectrometer control were carried out using a specialized software (Jobin-Yvon Spectra-Max for Windows version 3.0).

3.1 Optical imaging system

In order to obtain a real image of the trapped ions outside the EBIT, two lenses (L1, L2) are mounted inside the main vacuum chamber. The optical access is provided by a quartz window (≈ 92% transmission) setup on a side vacuum port. The optical system, used to rotate the image, is composed of two lenses and three mirrors contained in a completely opaque and closed box. The lenses (L3, L4) are used to transfer the image of the trap produced by the first set of lenses to the entrance slit of the spectrometer, as shown in Fig. 3.2. With the first and second mirrors (M1, M2) the image is rotated from horizontal to vertical. The last mirror (M3) is required to align the optical axis with the spectrometer (see Fig. 3.13). The distance from M1 to the spectrometer entrance slit is 230 mm.

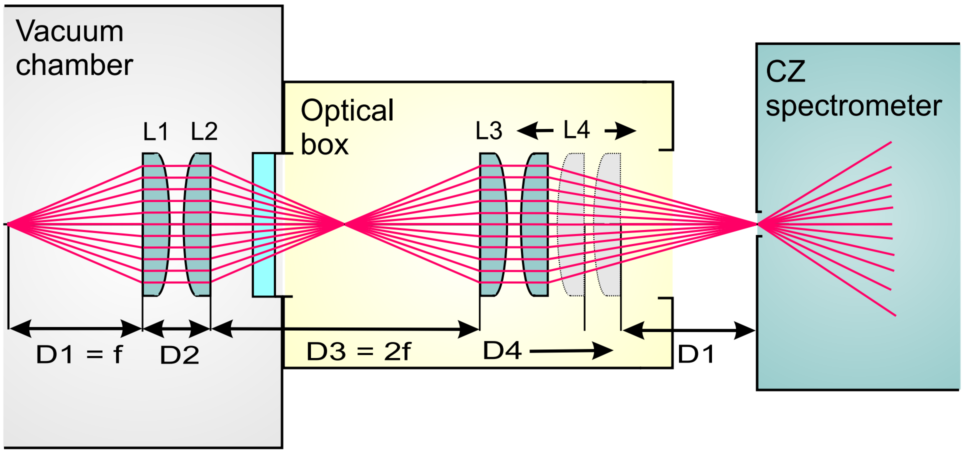

Figure 3.2: Optical system used to generate an image of the ion cloud inside the trap at the entrance slit of the spectrometer. The distance from the trap center to the port view is 300 mm. The lens L4 can be moved back and forth and, hence, the distances D4 and D1 change.

All the lenses used in this system are planoconvex. This arrangement was choosen to reduce spherical aberration. They are made of quartz (fused silica) and have 50 mm diameter and 150 mm focal length. The magnification of the system is roughly one at 441 nm. The substrate material of the mirrors is fused silica; they are coated with aluminum and have a protective MgF_2 layer. Their diameter is 25 mm and their flatness is $\lambda/4$ over the central 90% of the mirror diameter.

Coma and astigmatism

In a real imaging system, for points off the optical axis the images are comet-shaped figures rather than circles. This aberration is called coma [JW57]. A lens produces a sharp image at the field center, but the image becomes increasingly blurred towards the field edges.

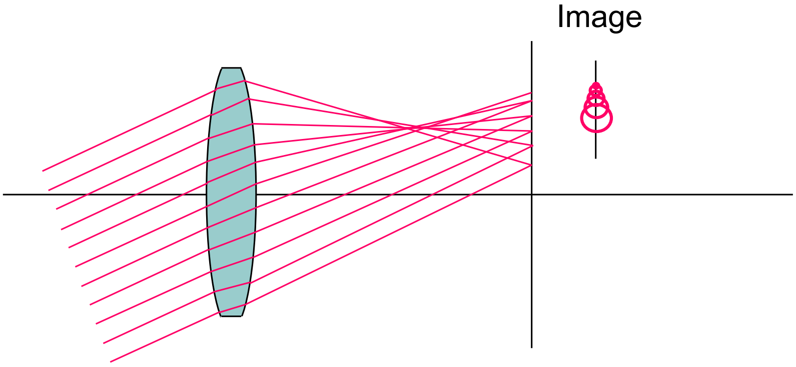

Figure 3.3: Illustration of the coma aberration of a lens.

The astigmatism of the spectrometer setup produces a curvature of the spectral image observed on the CCD camera. However, by binning the camera in 8 regions (stripes) and only using the central ones (where the image is sharpest) in the analysis, this effect is nearly eliminated. In Fig. 3.4a the FWHM for the $^2P_{3/2} - {}^2P_{1/2}$ transition in B-like argon is shown as a function of the CCD region (see below). The curvature of the lengthy image of the ion-cloud along the non-dispersive direction and the coma cause a wider FWHM of the line at the CCD regions further away from its center (towards the end of the trap). In Fig. 3.4b the peak intensity of this spectral emission lines is also shown as a function of the region on the CCD camera, *i.e.*, the position of emitters in the trap (the center of the CCD at around pixel number 500 corresponds to the center of the trap). The narrowest width corresponds to the highest line intensity.

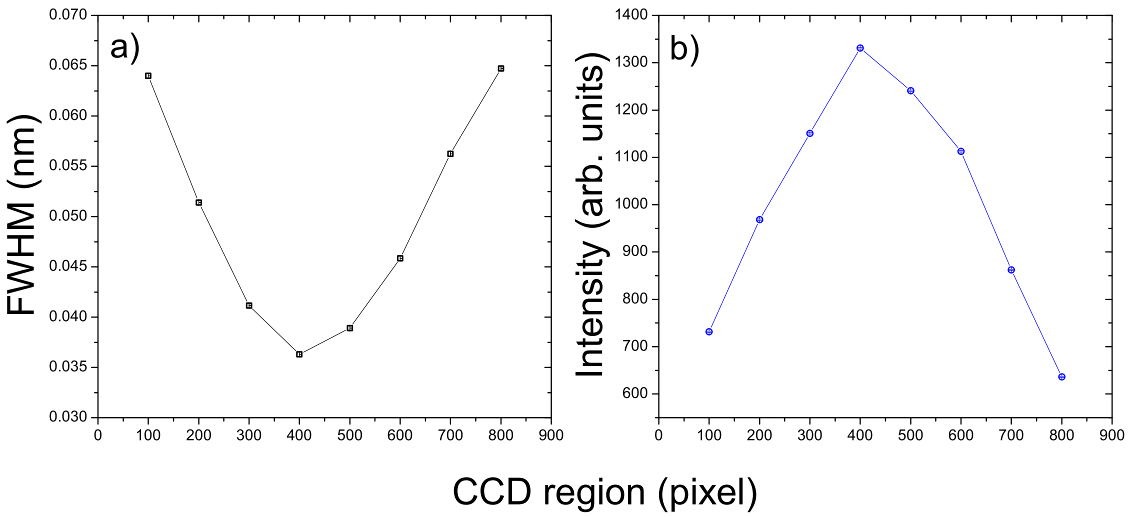

Figure 3.4: a) FWHM in nm (black squares) and b) peak intensity in arbitrary units (blue circles) as a function of the CCD region along the non-dispersive direction of the spectrometer.

3.2 Czerny-Turner spectrometer

The Czerny-Turner (CT) spectrometer function is to disperse the light into discrete wavelengths by means of a grating. The spectral image is viewed in the exit focal plane using a two dimensional CCD camera. A concave optical mirror (MC) is used to collimate the incoming radiation. After diffraction by the grating, the light is subsequently focused by a second concave mirror (MF) onto the CCD camera, as shown in Fig. 3.5.

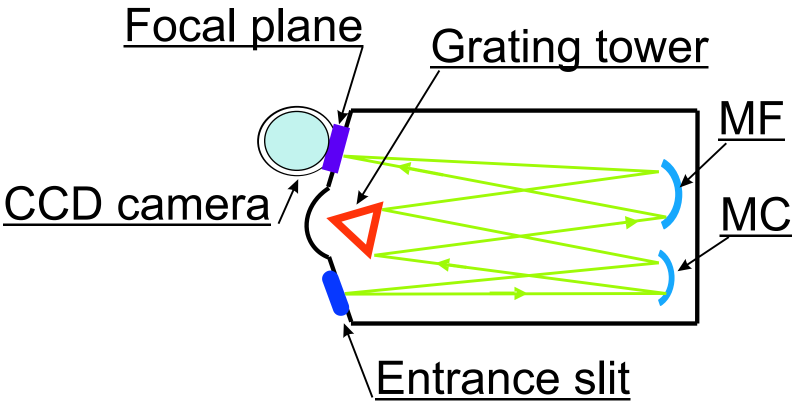

Figure 3.5: Illustration of the Czerny-Turner spectrometer.

In a CT spectrometer with a rotational grating, the axis of rotation of the grating is usually aligned along its surface. The symmetrical geometry of the CT produces a flattened spectral field and good coma correction at any given wavelength. The spherical aberration created by the first mirror is compensated by the second mirror (see below). The astigmatism is also reduced by illuminating the grating with an only slightly divergent beam. The focal length of the present spectrometer is 550 mm and its input aperture ratio f/6.4.

3.2.1 Grating properties

In a grating, the incident and reflection angles of a light beam with a wavelength λ (see Fig. 3.6) are related by the following equation:

$$sin\alpha + sin\beta_k = kn\lambda \ , \tag{3.1}$$

where α is the incidence angle, β_k the diffraction angle relative to the grating normal (N_G), k the diffraction order and n the groove density ($1/d$). When $k = 0$, Eq. (3.1) is reduced to $\alpha = \beta_0$, the specular reflection law. If the diffraction angle is fixed, the difference between α and β_k, the so-called deviation angle (D_V), is constant (see Fig. 3.6).

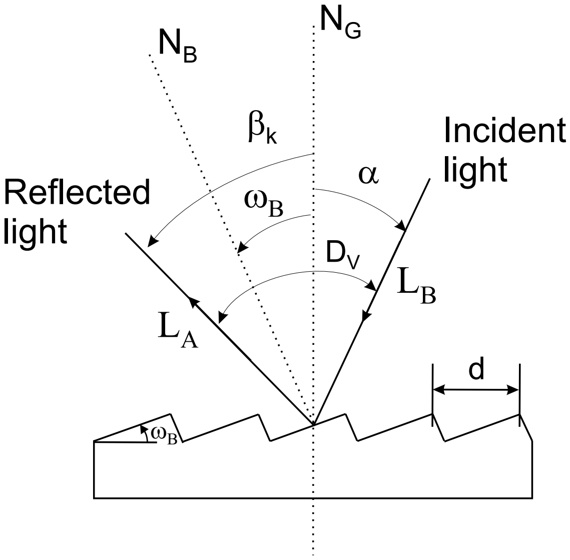

Figure 3.6: Scheme of the light reflexion in a grating. N_B is the blaze normal and ω_B defines the blaze angle. The distance between two consecutive grooves is defined by d.

A reflection grating can concentrate most of the diffracted spectral radiation into a single spectral order and, therefore, reduce the intensity of all other orders. This redistribution of intensity among the orders depends on the angle between the reflecting elements and the grating surface, which is called the *blaze angle* ω_B (see Fig. 3.6). Blazed gratings are optimized for a specific wavelength range and can reach an typically absolute efficiencies of more than 70% for this respective range.

Dispersion

The derivative of the diffraction angle over the wavelength is known as the *angular dispersion.* It is a measure of the angular separation between beams of adjacent wavelengths. An expression for the angular dispersion is derived by differentiating Eq. (3.1) for a fixed incident angle α. Thus,

$$\frac{\partial \beta_k}{\partial \lambda} = \frac{kn}{cos\beta_k} \quad . \tag{3.2}$$

A high dispersion can be achieved either by choosing a grating with a high groove density (n), or by using a coarse grating in high diffraction order (k). The linear wavelength dispersion at the exit focal plane of a spectroscopic instrument is usually specified as *reciprocal linear dispersion* given in nm/mm. If the focal length of the instrument is L_B, then the reciprocal linear dispersion is given by:

$$D(\lambda) = \frac{\partial \lambda}{\partial p} = \frac{kncos\beta_k}{L_B} \quad , \tag{3.3}$$

where p represents the distance in mm. Since the size of the instrument depends on the focal length of the optical system, by choosing a grating with a high groove density, the instrument can be made more compact.

As shown in Eq. (3.3), the relation between the pixel position p on the CCD camera and the real wavelength λ is given by the dispersion function $D(\lambda)$. This function depends on the wavelength. At least one reference point p_0 in the spectrum (a known wavelenght λ_0) is required to calibrate the wavelength scale, if $D(\lambda)$ is known. Then the λ of any other line on the spectrum can be obtain by

$$\lambda = \lambda_0 + \int_{p_0}^{p} D(\lambda) dp \quad . \tag{3.4}$$

This is, in general, difficult and often only numerically solve because the dispersion function is not a simple function of the wavelength. If the dispersion function is independent of λ, Eq. (3.4) is expressed as

$$\lambda = \lambda_0 + D(p - p_0) \ , \tag{3.5}$$

and the desired wavelength λ can be determined. For the CT spectrometer configuration, the dispersion function is given by [JW81]

$$D(\lambda) = \frac{d\lambda}{dp} = \frac{dx}{dp}\frac{1}{kL_Bn}\left(\sqrt{cos^2\phi - \left(\frac{kn\lambda}{2}\right)^2} - \frac{kn\lambda}{2}tan\phi\right) \ , \tag{3.6}$$

where dx/dp is the pixel size of the chip in the CCD and ϕ is the incidence grating angle. The use of this equation is cumbersome since for determination of each wavelength one would have to numerically solve Eq. (3.4) for the unknow λ.

Resolution

The *resolution* or *chromatic resolving power* of a grating describes its ability to separate adjacent spectral lines. The resolution is generally defined as R = $\frac{\lambda}{\Delta\lambda}$, where $\Delta\lambda$ is the difference in wavelength between two spectral lines with equal intensity that are separable.

The limit of resolution of a grating is R = kN, where N is the total number of grooves illuminated on the grating. A more practical expression for the resolution is obtained using Eq. (3.1)

$$R = kN = \frac{Nd(sin\alpha + sin\beta_k)}{\lambda} \ . \tag{3.7}$$

Since $sin\alpha + sin\beta_k$ can have a maximum value of 2, the maximum resolving power at any wavelength turns out to be equal to $2Nd/\lambda$, where the product Nd is the illuminated width W of the grating, and, therefore,

$$R_{max} = \frac{2W}{\lambda} \ . \tag{3.8}$$

This condition for the maximum resolution corresponds to the grating Littrow configuration, *i.e.*, $\alpha \approx \beta_k$, $|\alpha| \approx |\beta_k| \approx 90°$. The measured resolving power of a real grating is less than the theoretical value as the surfaces or the grating grooves deviate from the ideal shape and position. In the present experimental setup, we use a plano-blazed holographic grating which parameters are listed in Table 3.1.

Table 3.1: Properties of the plano-blazed holographic grating used here. λ_B is the blaze wavelength at the blaze angle ω_B and $R^{th,ex}$ denotes the theoretical and experimental spectrometer resolution, respectively

Parameter	***Value***
Grooves/mm	2400
Dimensions	76 × 76 mm
ω_B (at λ_B = 441 nm)	31.95°
Efficiency range	(0.67 - 2) λ_B
$\partial\lambda/\partial p$	0.643 nm/mm
R^{th}	0.002 nm
R^{ex}	0.03 nm

Efficiency

The grating efficiency is generally a rather complex function of the wavelength and polarization of the incident light and depends on the groove density, the shape of the grooves and the grating material. Depending on the orientation of the incident electric field vector with respect to the grating grooves, the efficiency can change rapidly over a narrow wavelength range, as shown in Fig. 3.7. This phenomenon was first observed by Wood in 1902 [Woo35], and usually called Wood's anomalies.

We have measured the efficiency of the grating for the light being polarized either parallel (S) or perpendicular (P) with respect to the grating grooves, by means of a hollow cathode lamp (see below). To separate S from P, a polarizer (PW-64) was inserted in front of the CT (see Fig. 3.13). The value of the transmission coefficient of this polarizer, provided by the company, for a given polarization is higher than 60% over the spectral range of interest (440 - 600 nm), as shown in Fig. 3.8. In Fig. 3.9 the ratio between the intensity of the perpendicular polarized radiation P and the parallel polarized radiation S is plotted versus the wavelength.

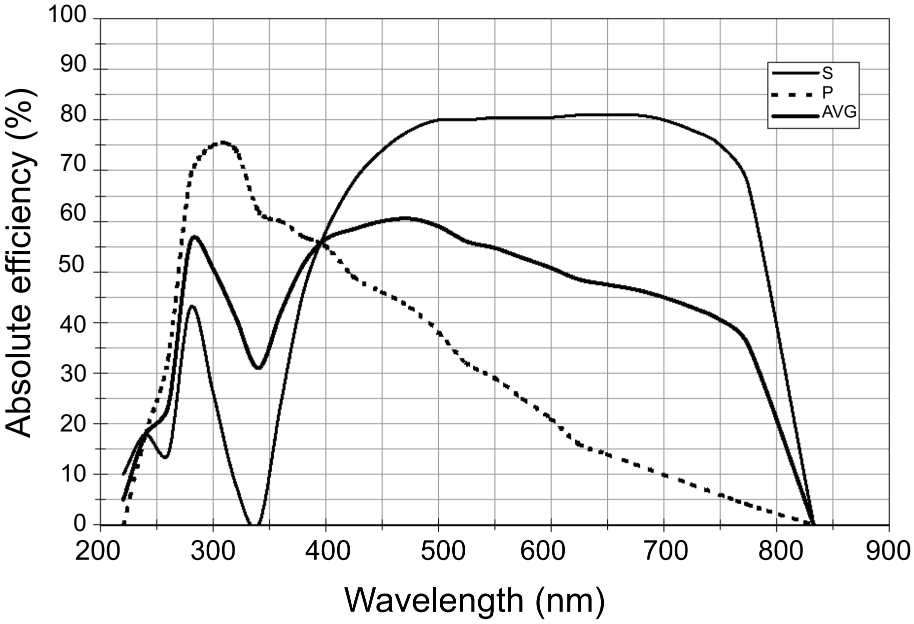

Figure 3.7: Theoretical efficiency as a function of the wavelength for a 2400 l/mm grating optimized for the visible region [Opt05]. S represents the incident light being polarized parallel with respect to the grating grooves, P the perpendicular polarization and AVG the averaged or random polarization.

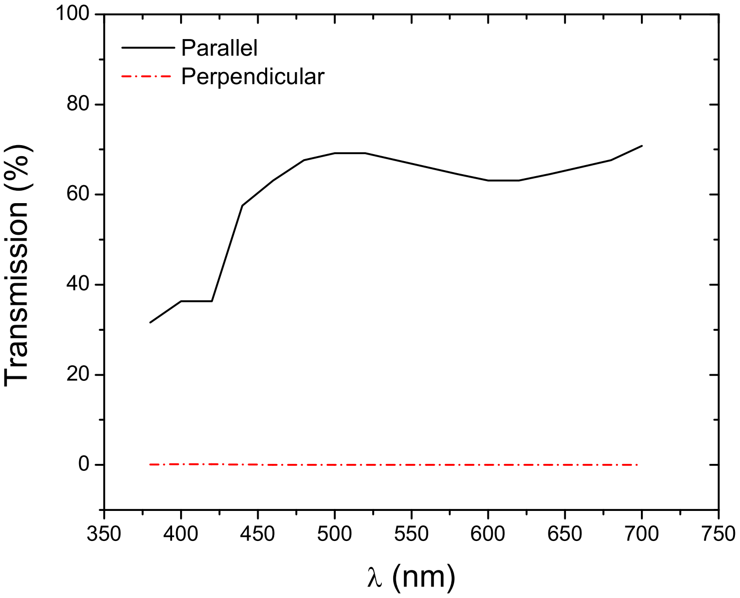

Figure 3.8: Transmission of the polarizer as a function of the wavelength. The solid line represents the transmission for the parallel polarization and the dash-dot line shows the transmission for the perpendicular one.

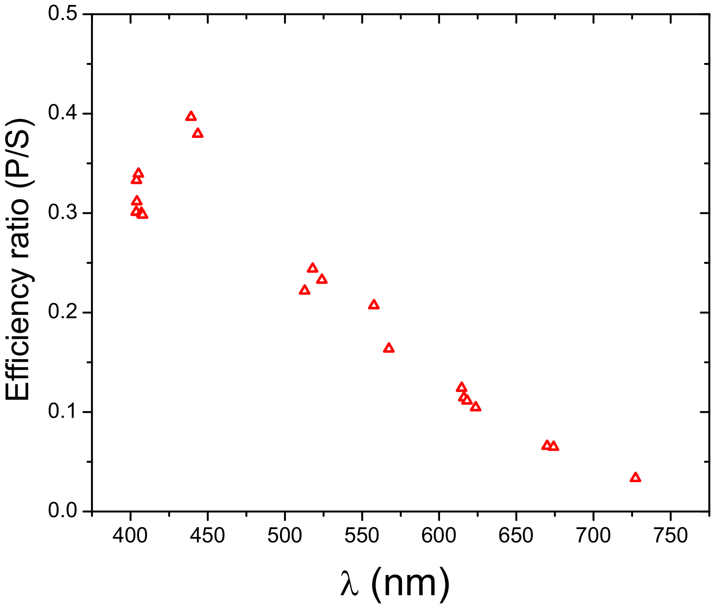

Figure 3.9: Ratio between the measured intensity of the perpendicular (P) and parallel (S) polarized beams, respectively, as a function of the wavelength, for the same incident flux.

3.3 CCD detector

The CCD camera is a solid state detector array made of silicon with a sensitive range from 400 to 1100 nm. It converts the incoming light into electrons through the photoelectric effect. These free electrons are stored in a rectangular array of imaging elements called pixels defined by a grid of gate electrodes in the X and Y directions, respectively. The charge is collected under the gate with the highest potential. During the readout cycle, the voltages applied to the gate electrodes are manipulated to shift the accumulated charge across the pixels to the output register at the edge of the array. The CCD provides simultaneously information for both intensities and positions projected along the height of the spectrograph image plane. The CCD chip size used is 30×12 mm^2 and is composed of 2000×800 pixels. Each pixel has an area of 15×15 μm^2.

The CCD readout can be binned and, thus, allow us to adjust the effective detector height from one pixel up to the full height of the camera. As more than one binned area can be read out for a given image, multiple spectra at different heights in relation to the main optical axis can be obtained. This results in horizontal images separated across the chip height (onto which the spectrometer slit is imaged). In this experiment the whole area of the CCD camera was usually divided into 8 different regions, each of them having 100 pixel height.

Three sources of noise affect the CCD: thermal dark current, readout noise and cosmic rays. The dark current is caused by free electrons resulting from thermal excitation from the valence band to the conduction band in the Si material. The readout noise is generated during the digitalization process, which involves an amplification of the charge. To correct the first of these two effects, a dark image is taken, in which no light strikes the chip and then subtracted pixel by pixel from the object image. As the camera is cooled with liquid nitrogen (LN2) to reduce thermal noise, it can integrate weak signals for hours without accumulating disturbing background (less than 1 electron/pixel/hour). Typical readout noise is less than 3 electrons/pixel at -140° C.

Cosmic rays are highly energetic particles which generate a huge amount of charge due to ionization processes over a few adjacent pixels, and appear as bright spots on the image. These cosmic ray hits are easily to discriminate and can be subtracted from the spectrum.

3.4 Adjustment procedure

The image focussing on the CCD camera was done by moving the MF mirror of the CT spectrometer. Then, the optical system and the spectrometer must be aligned with respect to the ions trapped inside the EBIT. To find the optical axis a He-Ne laser was used. For the fine tunning, the last lens L4 in the optical system is moved, perpendicular and parallel to the electron beam axis, to improve the focus and alignment adjustment, respectively.

3.4.1 Image focusing

In order to focus the slit image properly onto the CCD detector, the second mirror (MF) of the CT spectrometer (see Fig. 3.5) is mounted in a linear stage, which can be moved back and forth by means of a micrometer screw within a range of 25 mm. Fig. 3.10 shows how the shape of a calibration line changes as a function of the MF position. Here, it should be noticed the sharp deformation of the observed profile at large displacements from the ideal position. The best focus was obtained at the setting of $\approx$ 15 mm. The mirror was then adjusted around the optimum position in fine steps in order to maximize the line intensity and to reduce the width of the observed spectral line, as shown in Fig. 3.11.

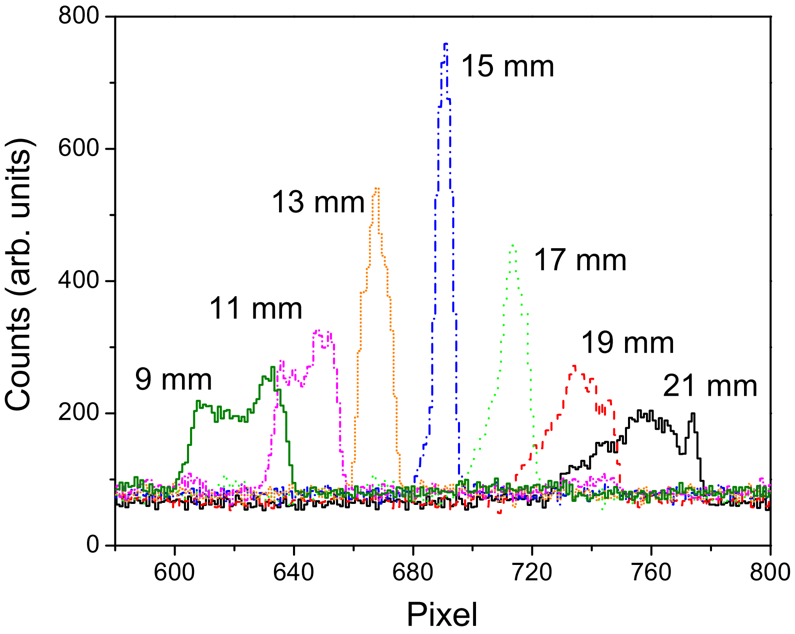

Figure 3.10: Bringing the CCD into the focus by moving the MF mirror in 2 mm steps. As the optimum focus is approached the spectral line shown here appears narrower and more symmetrical, and, thus, displays a higher peak intensity.

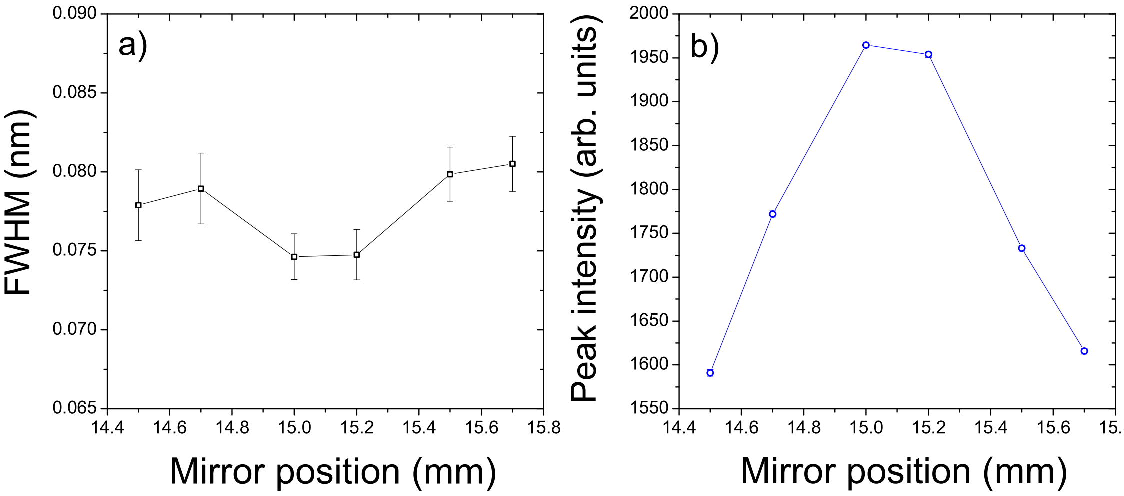

Figure 3.11: a) FWHM (black squares) and b) intensity in arbitrary units (blue circles) as a function of the fine focusing of the MF mirror position.

3.4.2 Alignment of the spectrometer

During the alignment procedure, at first a linearly polarized He-Ne laser (at 633 nm) beam is sent through the optical system from the last lens L3 into the center of the quartz window (vacuum chamber). Then the optical box is fixed to a table preventing any movement. Once the optical axis has been so found, the spectrometer is mounted onto the same table behind the box, in such a way that the imaginary line between the entrance slit and the center of the first mirror MC of the CT spectrometer is aligned to the optical axis defined by the laser. The spectrometer is fixed to the table at about 300 mm from the view port window. Since blue light ($\approx$ 400 nm) is more strongly focused than red light ($\approx$ 700 nm), this distance slightly varies as a function of the wavelength under observation.

The size of the image coming from the central drift tube slits of the EBIT is 40 mm (length) $\times$ 7 mm (height), and is projected onto the entrance slit plane. The entrance slit has a height of 15 mm and a variable width of up to 2 mm, which can be closed down as much as desired to increase the spectral resolution. By using a beam stop, the height of the entrance slit can be reduced as well in few steps down to 1 mm.

In order to center the image of the trapped ions on the entrance slit, first the slit is fully opened to 2 mm width and an image of the trapped ions is collected at the wavelength of some prominent spectral line in which the ions emit radiation. Since the entrance slit is much wider than the ion cloud image, the centroid of the wide line observed indicates its position on the entrance slit plane. Then, the slit is closed down to 50 μm width and another image is taken. In this case, the centroid position is due to the image of the narrow slit, which has a fixed position with respect to the instrument axis. If the centroids of these two lines are shifted, the image of the ion cloud is not exactly centered on the slit. In order to adjust the image to the slit, the last lens L4 (mounted on a linear stage) is moved left and right (parallel to the electron beam axis) using a micrometer screw. After moving the lens, another image using again a 2 mm slit is taken and compared with the one obtained with the narrow slit width. This process is repeated until the image of the ion cloud is centered onto the spectrometer entrance slit.

As can be seen in Fig. 3.12, when the slit width is 50 μm and less, the line centroids are shifted. This indicates that the image of the ion cloud is not perfectly aligned with respect to the entrance slit. Such a misalignment results in a loss in signal intensity and could, under certain conditions, affect the wavelength calibration.

Once the optimum for the 50 μm slit is achieved, the slit is successively closed down to 20 μm and 10 μm, then, the same process is repeated (see Fig. 3.12). Moreover, L4 can also be moved back and forth to focus the ion cloud image as perfectly as possible onto the entrance slit. When the slit is fully open the real image of the trapped ions at the entrance slit plane, which is narrower than the slit, is projected onto the CCD. In this case, one can see a convolution of the geometrical size of the ion cloud and the spectral width of the emission line used for the image. By reducing the slit width, the spectrometer resolution improves within certain limits. However, the line peak intensity is reduced. As a compromise between intensity and resolution, the spectrometer slit was set to 50 μm in most of the present measurements.

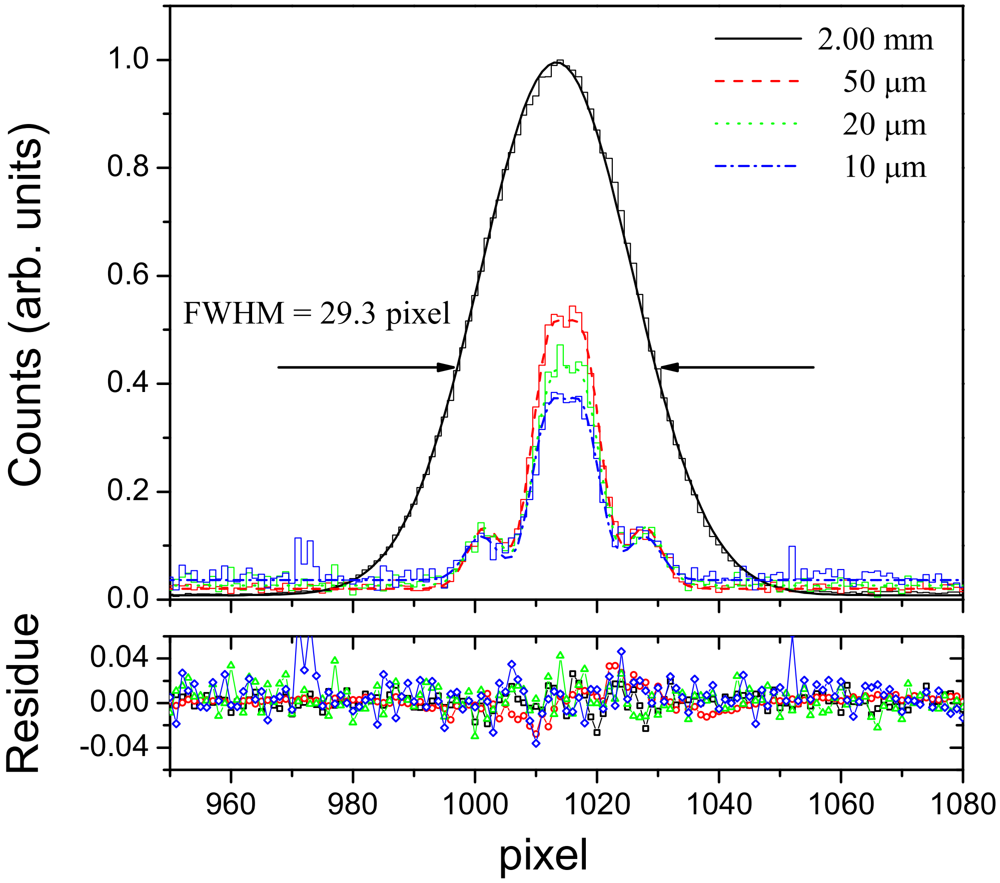

Figure 3.12: Image of the ion cloud on the CCD detector taken at different slit widths. The lower diagram displays the residues. Square symbols correspond to 2.00 mm, circles to 50 μm, triangles to 20 μm and rhombuses to 10 μm slit width, respectively.

In Fig. 3.12, for the ion cloud images taken with a 2 mm slit, the observed line is fitted with a single Gaussian function. As the entrance slit is made narrower and, thus, the resolution increases, the Zeeman splitting becomes apparent. For instance in the ${}^2P_{3/2}-{}^2P_{1/2}$ transition, six components are expected and, hence, the spectrum is fitted with six Gaussian functions, for the cases of 50 μm, 20 μm and 10 μm slit width, respectively.

3.5 Calibration

The observed spectrum on the CCD camera delivers intensity as a function of the pixel position. We need to convert this "internal" unit, *i.e.*, the number of pixels into correct wavelengths. For that purpose, a hollow cathode lamp was used. Moreover, to determine the "real" width or intensity of a line we need to know how the spectrometer itself affects the assumed Gaussian profile of the individually observed emission lines of the spectrum.

3.5.1 Hollow cathode lamp

In order to calibrate the observed spectrum, reference lines are needed. A hollow cathode lamp yields a strong signal characterized by sharp emission lines. The lamp consists of an anode and a cylindrical cathode sealed in a glass tube filled with an inert gas at a typical pressure of 1 - 5 Torr. The cathode is made of the element under study. A window transparent to the emitted light is fused to the end of the tube. Light is emitted from the lamp when sufficient potential difference is applied between the cathode and the anode resulting from collisions of gas molecules and atoms sputtered from the cathode with discharge electrons. The radiation from the lamp is focused by means of two achromatic doublet lenses (with 56 mm and 75 mm focal length, respectively) onto an optical fibre and guided through it into the optical box. Here, the light is reflected by means of a diffuser placed in front of the first mirror (M1). From there on, the radiation from the calibration lamp follows the same path as the ion cloud image into the spectrometer as shown in Fig. 3.13. The diffuser is moved into the beam path for the calibration only, and is moved out for data taking.

In the present case, the cathode is made of iron, and the lamp is filled with neon, which emits many lines in the spectral region of interest (200 - 700 nm). The maximum operation current of the lamp is 10 mA. A zoom into some of the typically ten emission lines used for calibration in a single exposure is shown in Fig. 3.14. These spectral lines are fitted to Gaussian functions (see below), all of them having the same width. In the fit, the square root of the statistical error is used to determine the error associated to the center peak position. Only prominent

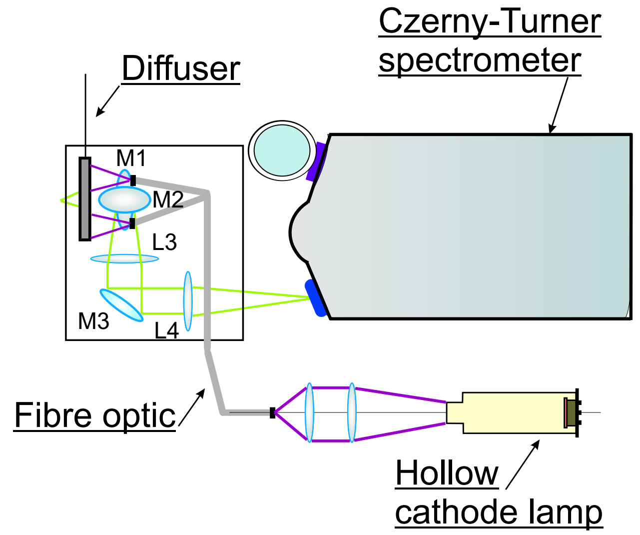

Figure 3.13: Setup for the hollow cathode lamp used for the light wavelength calibration.

lines with accurately known values are used for the calibration and, hence, the non fitted lines have larger residues. The recommended wavelengths, which were used here have been taken from the NIST data base (*http://physics.nist.gov*), and are listed in Table 3.2. Most of these lines have an uncertainty as small as 0.0005 nm and, in the best cases, the uncertainties are only 0.00005 nm. The contribution of the uncertainty of the calibration line wavelength to the total error bar is, therefore, almost completely negligible.

Table 3.2: Reference lines used for the calibration taken from *http://physics.nist.gov*

Species	λ ***(nm)***	***Species***	λ ***(nm)***	***Species***	λ ***(nm)***
Fe I	432.5762	Fe I	448.2228	Ne I	596.16243
Fe I	437.5929	Ne I	588.18952	Ne I	596.54716
Fe I	438.3544	Ne I	590.248	Ne I	597.46283
Ne II	439.1995	Ne I	590.64278	Ne I	597.55340
Fe I	440.4750	Ne I	591.36325	Ne I	598.79070
Ne II	440.930	Ne I	591.89080	Ne I	599.16511
Fe I	441.5122	Ne I	593.44560	Ne I	600.09263
Fe I	442.7299	Ne I	593.93180		
Fe I	446.1652	Ne I	594.48342		

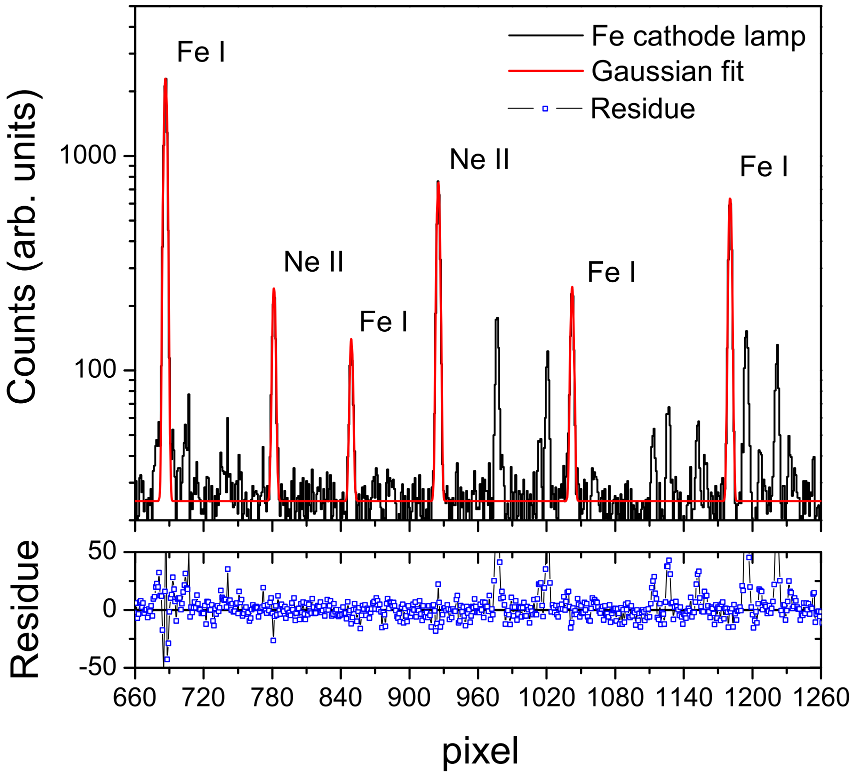

Figure 3.14: A typical spectrum from a calibration Fe lamp over 438 - 443 nm range. Some of the lines were fitted with Gaussian functions. The lower plot displays the residue of the fit.

3.5.2 Spectral line profiles

The light emitted in atomic transitions is not perfectly monochromatic. The observed spectral lines are always broadened, partly due to intrinsic physical reasons and partly due to the finite resolution of the spectrometer. The *natural line* width, as well as, the *Doppler*, the *Stark* and the *pressure broadening* are different mechanisms which affect the final spectral line width. The Lorentzian and Gaussian profiles which are produced by these different broadening mechanisms appear convoluted in the observed spectral lines, resulting in the more general Voigt profile. The Doppler broadening is caused by the thermal motion of the ions in the trap. The Stark broadening [Sal98] is due to the averaged effect of the microscopic electric fields experienced by the radiating species during collision with particles which are charged or have a strong permanent electrical dipole. Pressure broadening [Gri97] is due to collisions of the emitters with neighboring particles which cause a perturbations of the energy levels. These two last effects are negligible compared with the Doppler effect and, hence, not described here.

Natural broadening

The excited states decay to the ground state with a finite lifetime (τ) by spontaneous emission. Thus, the indetermination in time due to the Heisenberg uncertainty principle produces the so-called natural broadening of the emission line. A Lorentzian, also known as Breit-Wigner [BW36], distribution corresponds to this natural broadening and reads as

$$y = \frac{1}{2\pi} \frac{\Gamma}{\left(\nu - \nu_0\right)^2 + \Gamma^2} \quad , \tag{3.9}$$

where ν_0 is the peak center and Γ is the full width at half maximum (FWHM), which for a normalized function $\Gamma = 1/2\pi\tau$. In Fig. 3.15 the Lorentzian function is compared with a Gaussian function (see below).

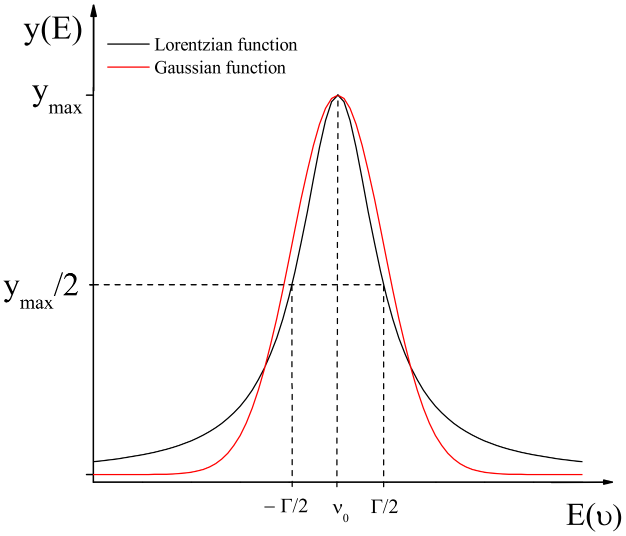

Figure 3.15: Lorentzian and Gaussian profiles, respectively. The full width at half maximum is given by Γ.

Doppler broadening

The thermal velocity distribution, $n(v)$, of the light emitting ions, with the velocity v is usually described by the following, so-called Maxwellian-Boltzmann distribution function [BS03]:

$$n(v)dv = N\sqrt{\frac{M_i}{2\pi k_B T_i}}exp\left(-\frac{M_i v^2}{2k_B T_i}\right) dv \quad , \tag{3.10}$$

where N is the total number of ions, M_i the ion mass, T_i the ion temperature and k_B the Boltzmann constant. The average velocity v_0 of the distribution is given by

$$v_0 = \sqrt{\frac{2k_B T_i}{M_i}} \quad . \tag{3.11}$$

Due to the Doppler effect, the observed radiation frequency ω emitted by an ion moving with a velocity v relative to the observer differs from the frequency ω_0 observed when the ion is at rest by

$$\omega = \omega_0 \left(1 - \frac{v}{c}\right) \quad , \tag{3.12}$$

where c is the speed of light. The normalized Doppler broadened shape of a spectral line is a Gaussian profile given by

$$I(\omega) = \frac{1}{\sqrt{\pi}\Delta\omega_D} exp\left[-\frac{(\omega-\omega_0)^2}{\Delta\omega_D^2}\right] \quad , \quad \Delta\omega_D = \omega_0 \frac{v_0}{c} \quad , \tag{3.13}$$

where the quantity $\Delta\omega_D$, called the Doppler width, is

$$\Delta\omega_D = \frac{2\omega_0}{c}\left[2ln2\frac{k_B T_i}{M_i}\right]^{1/2} \quad . \tag{3.14}$$

This value of $\Delta\omega_D$ corresponds to the FHWM of the Doppler broadened line. As an example, the Doppler broadening of the $1s^2 2s^2 2p\ {}^2P_{3/2} -{}^2 P_{1/2}$ transition in Ar^{13+} (M_i = 40 a.u. and at λ = 441 nm) in a plasma with $k_B T_i$ = 300 eV is about $\Delta\omega_D \approx$ 0.1 nm, which corresponds to an spectral line width of 5.5 $\times 10^{-6}$ eV, compared with 4.3$\times 10^{-13}$ eV natural line width.

Instrument response

The finite resolution of a spectrometer is characterized by the instrumental response function or apparatus profile, *i.e.*, the response of the spectrometer to a δ-function-like spectral line. When the light passes through the spectrometer, the resulting line shape is characterized by the convoluted form $g(\lambda)$:

$$g(\lambda) = \int_{-\infty}^{\infty} G(x) I(\lambda - x) dx \quad , \tag{3.15}$$

where I is the instrument response function and G the true line profile. To determine the instrumental function we used the narrow spectral lines emitted by the Fe hollow cathode lamp, since their width is much smaller than the instrument resolution. The lines choosen were the strongest and/or most-isolated ones. These observed lines were fitted by Gaussian functions described by

$$y = y_0 + \frac{A}{\omega\sqrt{\pi/2ln4}} e^{-2ln4\left(\frac{x-x_c}{\omega}\right)^2} \quad . \tag{3.16}$$

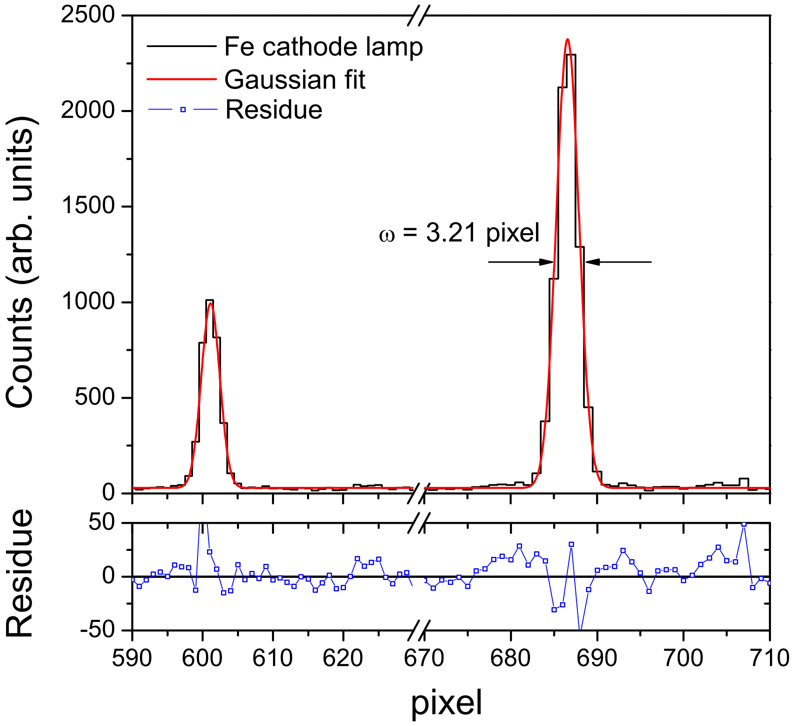

Figure 3.16: Observed line profile obtained with 50 μm slit width. The lower plot shows the residues.

Although the emission lines should be represented by a Voigt profile, the broadening of the emission line is almost purely due to the Gaussian width, as explained before. The deconvolution function required in order to obtain the instrument profile is difficult to solve analytically. However, as the Doppler line width (from the hollow cathode lamp) is smaller than the spectrometer response function we can say, to a very good approximation, that the Gaussian profile of these lines represents the instrument response function reasonably well (see Fig. 3.16). For a spectrometer slit width of 50 μm (ideally the slit image would be a box function of 50 μm width), all of the lines displayed a FWHM of 3.2 pixels over the whole wavelength range investigated.

3.5.3 Dispersion

In order to obtain the dispersion function (see Eq. 3.5) of the spectrometer which best represents the experimental results we can approximate the wavelength λ with a polynomial function of the pixel position p

$$\lambda = A + B * p + C * p^2 + ... \quad , \tag{3.17}$$

where A, B and C are free parameters. From a calibration spectrum such as the one shown in Fig. 3.14 we determine the pixel positions of a series of known lines by fitting single Gaussian to them. Each of these peak positions values ise related to the references wavelengths listed in Table 3.2. Then, with each pair of values (reference wavelength versus peak position) we made a plot (see Fig. 3.17). Although, the error bar of the peak position is in most cases of the order of 0.03 pixel, they are relatively large compared with the typical precision of the reference wavelengths of 0.0001 nm. Hence, no one of these errors (on X and Y axis), are appreciably visible on the plot. The observed data were then fitted with first, second and third order polynomial functions.

Table 3.3: Result for the A, B and C parameters of the polynomials

Function	$\boldsymbol{A}$	$\boldsymbol{B}$	$\boldsymbol{C}(\times 10^{-8})$	$\boldsymbol{D}(\times 10^{-12})$	χ^2/DOF	$\boldsymbol{R}^2$
Linear	432.26(2)	0.00895(2)	—	—	900.68	0.99996
Parabolic	432.223(1)	0.009092(2)	-9.0(1)	—	1.78	1
Cubic	432.222(1)	0.009098(5)	-10.0(8)	4(3)	1.77	1

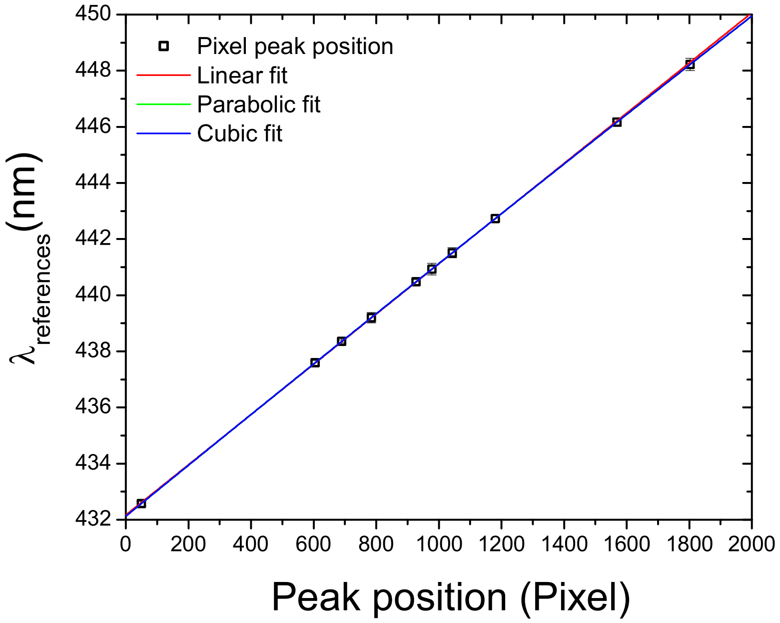

Figure 3.17: Reference lines versus peak position of the emission lines of the calibration lamp.

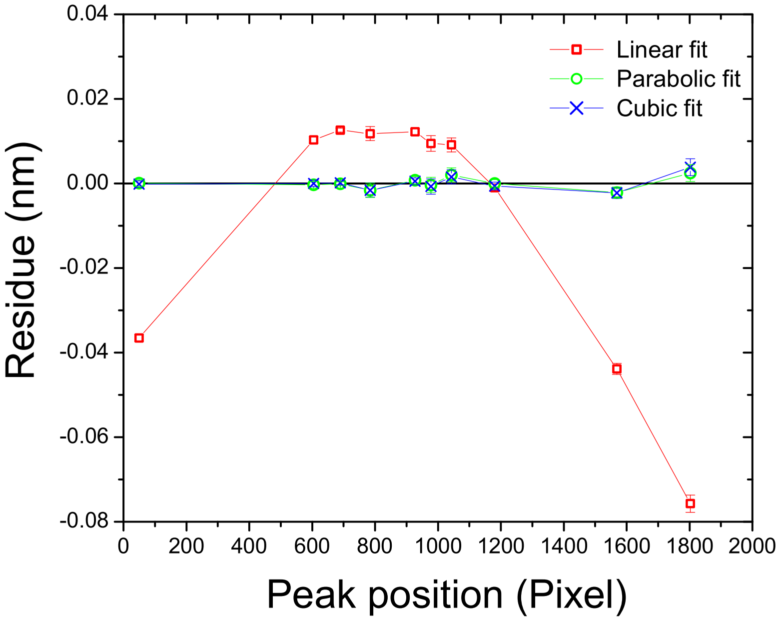

Figure 3.18: Residue of the polynomial functions as a function of the peak position.

The results of the fit are shown in Table 3.3. The χ^2/DOF is the reduced χ^2 for the parameter values over the number of degrees-of-freedom DOF. The χ^2 defines the best fit by choosing the parameters such that the sum of the squares of the deviations of the theoretical curve from the experimental points for a range of independent variables is at its minimum. The DOF is given by the number of data points considered less the number of free parameters. R^2 is the square of the correlation coefficient, which is a measure of the quality of the least-squares fitting to the original data. Its maximum value is 1, and corresponds to a perfect fit.

In Fig. 3.18 the residues (the differences between the fitted curve and the data points) are shown. The best fit function has the smallest residuals. In such a way, the linear fit is ruled out. There is almost no difference in quality (within the error bars) between the parabolic and cubic fit, and therefore the parabolic one was chosen to approximate the spectrometer dispersion function.

3.6 Data acquisition process

The acquisition process consist of three parts: *i)* A first calibration is made by sending diffuse light of the calibration lamp to the spectrometer (see Fig. 3.13). *ii)* Without changing any spectrometer parameters, the diffuser is removed and the EBIT image is now registered. *iii)* Then, a second calibration is made. This set of three spectra delivers what we call a data point. The two calibrations are important to check the experimental stability of the system; only when the two calibrations are consistent, we use the data point in the further analysis.

The averaged acquisition time for one data point including the calibration is typically 30 to 60 minutes. This exposure time can vary strongly depending on the intensity of the observed emission lines. During this time two independent spectra are taken (accumulations) for each calibration as well as the ion spectrum, of which the second one is used to discriminate and remove possible spikes due to the cosmic rays. To reduce vibrations, during the whole experiment, the access to the experimental area is restricted to filling liquid nitrogen for cooling the CCD camera once a day.

The CCD chip has 2000 pixels to cover roughly an 18 nm range when using the 2400 l/mm grating. Thus, we have a linear dispersion of 9×10^{-3} nm/pixel. The grating is moved in fine steps of 0.01 nm between individual data points corresponding roughly to 11 pixels steps to obtain enough data points across the line profile for the accurate determination of the centroid, and also to reduce systematic uncertainties of any particular pixel. By scanning the grating between 30 to 40 times (see

Fig. 3.19) for a given line, we obtain enough data points accross the line profile to determine the line centroid with an accuracy of 0.3 pixels.

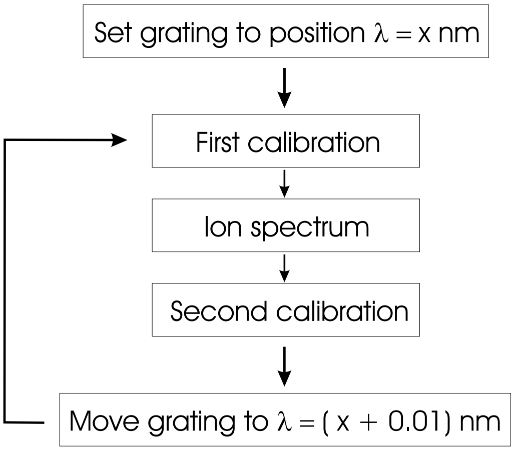

Figure 3.19: Diagram of the routine followed in the data acquisition process.

Chapter 4

Results and discussion

The improved experimental resolution achieved in the present work allows us to study the isotopic shifts in middle-Z ions, and the g_J-factor of some metastable levels. Moreover, by investigating different isotopes, we have explored the relativistic recoil effect and compared to most recent calculations for the first time. The favorable experimental conditions of our set up were also used to extract information on other important parameters of the trapped ions, as their temperature and spatial extension. These quantities are inferred from characteristics of the spectral lines, such as their width, intensity and wavelength. Argon was chosen since many observations of its coronal lines have been reported and their wavelengths have been systematized in a considerable amount of works since Edlén [Edl55] and Pryce [Pry64]. The interest in these transitions is also reflected in the large number of calculations published [SJS96a, SJS96b].

4.1 Wavelength determination

The ground configuration $2s^2 2p$ of B-like Ar^{13+} ions consists of two levels, $^2P_{1/2}$ and $^2P_{3/2}$ as shown in Fig. 4.1. They have the same parity and, hence, the upper level cannot decay through an electric dipole (E1) transition but a relaxation through a magnetic dipole (M1) or an electric quadrupole (E2) transition is possible. Since the M1 decay is about five orders of magnitude faster than the competing E2 transition, it is the only important one for the determination of the transition energy. Be-like argon, Ar^{14+}, on the other side, has four fine structure levels in its first excited configuration $1s^2 2s2p$, $^1P_1$ and $^3P_{0,1,2}$. In the present work, we studied the forbidden transition from the $^3P_2$ to the $^3P_1$ level (see Fig. 4.2). These two ions under study feature just one single measurable line in the visible spectrum each. For the first

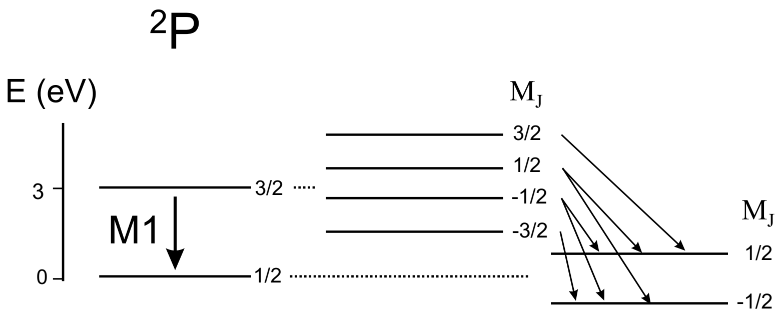

Figure 4.1: Grotrian diagram of the $2s^22p$ levels in the B-like argon (Ar XIV). The energy scale is only approximate.

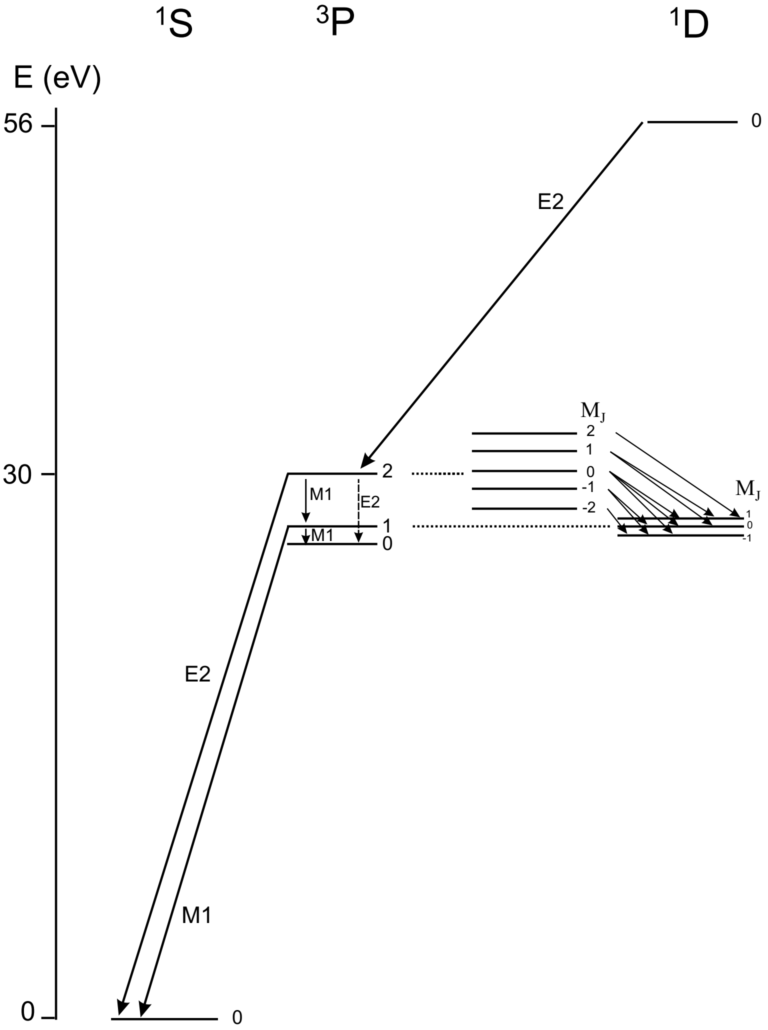

Figure 4.2: Grotrian diagram of the $2s2p$ levels in the Be-like argon (Ar XV). The energy scale is only approximate.

case, Ar^{13+} ($^2P_{1/2}$ – $^2P_{3/2}$) the localization of the emission line in the spectrum is an easy task, due to its high intensity. However, this is not the case for the second, Ar^{14+} ($^3P_2$ – $^3P_1$), much weaker line. Here, the necessary adjustments to the spectrometer were carried out using the strong transition $^2P_{1/2}$ – $^2P_{3/2}$ from Cl XIII [Edl82] because its wavelength is close to the Ar XV line, allowing faster focusing and alignment (see Fig. 4.3).

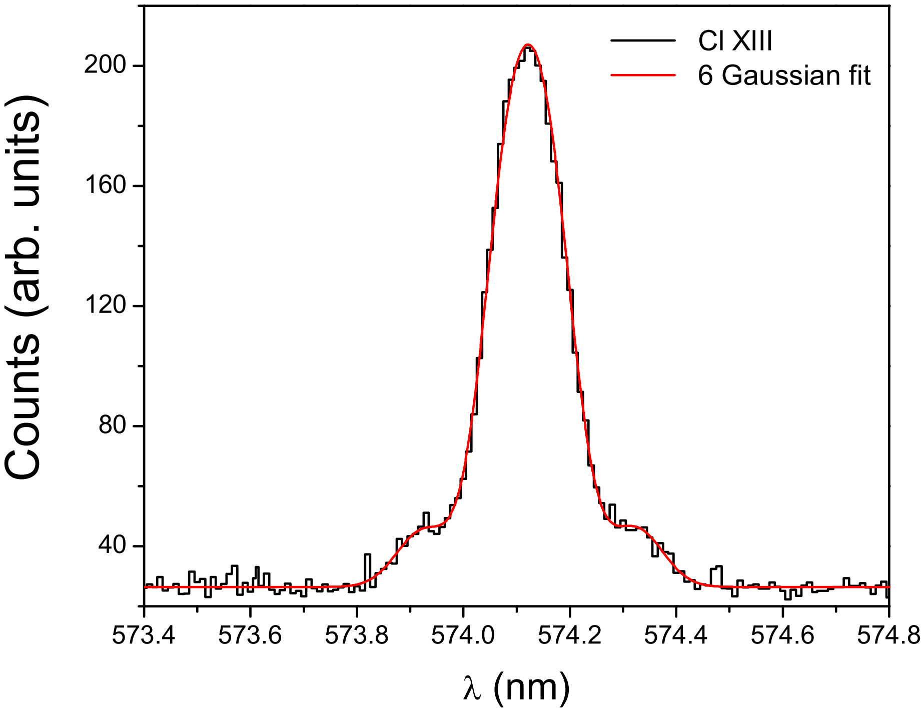

Figure 4.3: Typical spectrum showing the Zeeman splitting of the transition $^2P_{1/2}$ – $^2P_{3/2}$ in Cl^{12+} at $E_e = 700$ eV, $I_e = 90$ mA and 8 T magnetic field.

In an EBIT, the electron beam energy basically determines the ion charge state. The minimum energy required to ionize Ar^{12+} and Ar^{13+}, are 675 eV and 744 eV, respectively. The main operational parameters used in the present experiment are listed in Table 4.1. The injected gas pressure was similar in both cases. The trap was dumped every few seconds in order to avoid an excessive accumulation of heavy impurity ions. The axial main magnetic field was varied in a series of measurements in order to check any possible influence of its value in the center of gravity of the emission lines (see below). The exposure times were shorter for Ar^{13+} than Ar^{14+}, due to the higher excitation rate of the upper level and also to the absence of any competing transition starting from the same level. For Be-like argon, a very low potential was applied to the trap drift tubes.

Table 4.1: EBIT operational parameters for the visible transitions under study. * Electron beam energy without including the space charge potential of the electron beam

Parameter	$\boldsymbol{Ar}^{13+}$	$\boldsymbol{Ar}^{14+}$
Beam energy* (keV)	0.875	1.097
Beam current (mA)	50	88
Drift tube potential DT4/DT5/DT8 (V)	0 / 0 / 0	5 / 0 / 400
Injection pressure (Torr)	7×10^{-9}	4×10^{-9}
Dump time (s)	20	1
Magnetic field (T)	5 - 8	5 - 8
Single exposure time (s)	1800	2400

The best conditions for data acquisition were found to be a most shallow trap and the highest possible magnetic field (see section 2.2) for the EBIT operation. This reduced the spectral line width, allowing us to resolve the Zeeman splitting (see Section 1.5) for the B-like transition. However, for the Be-like line this splitting was not clearly visible when looking into the different CCD camera regions individually since the signal is much weaker. Nevertheless, it was possible to observe this effect by averaging three out of the eight camera regions, as will be shown later. The data analysis was carried out by means of a program written in the LabVIEW language (see Appendix B).

4.1.1 Zeeman splitting in B-like argon

From the Zeeman splitting of the M1 transition in B-like argon, six components are expected, as shown in Fig. 4.4. In this spectrum, the six components correspond to two different polarizations, namely π- and σ-components, with a polarization parallel and perpendicular to the magnetic field, respectively, for a transversal view. This spectrum is fitted with 6 Gaussians for which the main three parameters are the width W_i, the amplitude A_i and the peak position xc_i. The widths of the 6 lines are constrained to be equal, as they are mainly determined by the ion temperature and the spectrometer resolution. As the amplitude depends on the population and transition probabilities of the different levels, and the spectrum has to be almost completely symmetric around its center of gravity, they are equally fixed in pairs. The peaks are nearly equidistant, and the differences between their positions will be used for the g_J-factor determination.

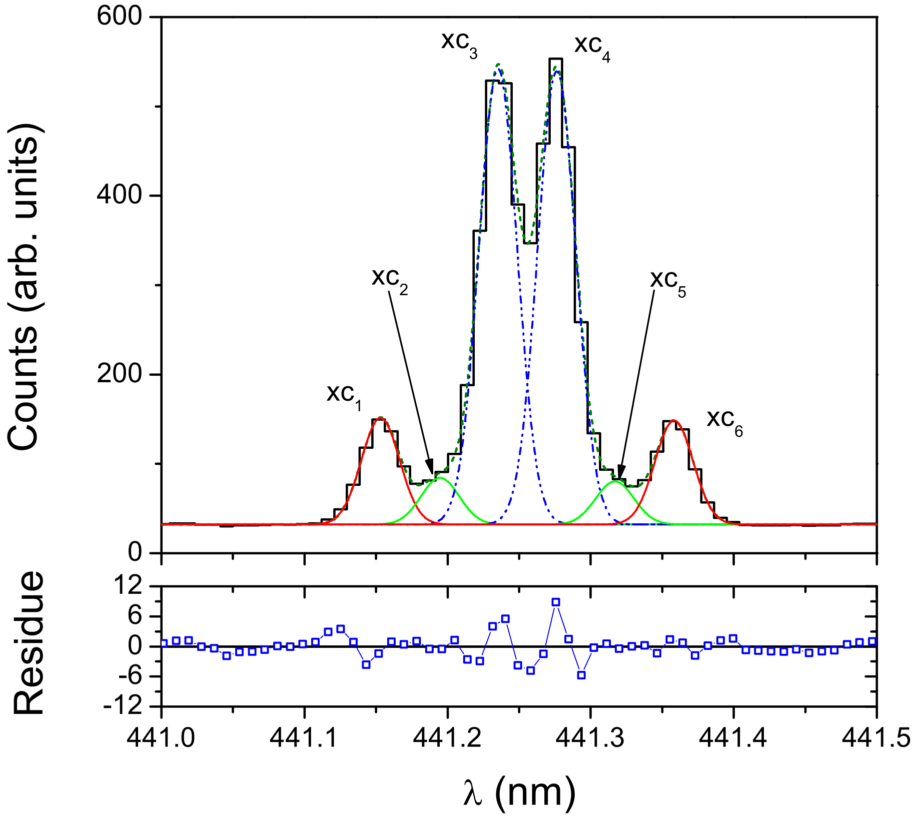

Figure 4.4: Typical spectrum showing the Zeeman splitting of the transition $^2P_{1/2} - {}^2P_{3/2}$ in Ar^{13+} at E_e = 875 eV, I_e = 50 mA and 6.82 T magnetic field. The peaks are named as $\mathrm{xc}_1(\pi^+_{3/2})$, $\mathrm{xc}_2(\pi^+_{1/2})$, $\mathrm{xc}_3(\sigma^+)$, $\mathrm{xc}_4(\sigma^+)$, $\mathrm{xc}_5(\pi^-_{1/2})$ and $\mathrm{xc}_6(\pi^-_{3/2})$. The lower scatter plot shows the fit residuals.

As is shown in Fig. 4.4, in the following, the peaks are indexed from one to six according to the order of appearance in the spectrum. The first peak on the far-left (xc_1) corresponds to the transition from the level $M_J = 3/2$ to the $M'_J = 1/2$, that means from $M_J \to M_J - 1$ (ΔM_J=1). This peak has π polarization and is named by the notation $\pi^+_{3/2}$. The next peak (xc_2) is due to the transition from the level M_J = 1/2 to the M'_J = -1/2 and, hence, also from $M_J \to M_J - 1$, thus being π polarized as well. The assigned notation is $\pi^+_{1/2}$. The third peak (xc_3) arises from the transition between the levels M_J = -1/2 and M'_J = -1/2, therefore $M_J \to M_J$ (ΔM_J=0) and it has σ polarization which leads to the notation σ^+. The fourth (xc_4) peak is labelled as σ^-, and the fifth and sixth have the same notation as xc_2 and xc_1, respectively, but with a minus, because in these cases the transitions are for $M_J \to M_J + 1$ (ΔM_J=-1) and, hence, we use $\pi^-_{1/2}$ and $\pi^-_{3/2}$ for xc_5 and xc_6, respectively (see Fig. 4.1). According to the polarizations the amplitudes of the different peaks are named as A1 for $\pi^+_{3/2}$, A2 for $\pi^+_{1/2}$, A3 for σ^+, A4 for σ^-, A5 for $\pi^-_{1/2}$ and A6 for $\pi^-_{3/2}$.

Temperature of the trapped ions

As shown in Seccion 3.5.2, the ion temperature has an effect on the width of the observed spectral lines. This width, as obtained from the fit, is used here to determine the ion temperature T_i by means of the following equation

$$k_B T_i = \frac{M_i}{2ln2}\left[\frac{\Delta W_D \lambda_0}{4\pi}\right]^2 , \tag{4.1}$$

where $\lambda_0 = 2\pi c/W_0$ corresponds to the central wavelength, with W_0 being the natural line width, and M_i is the ion's atomic mass. Neglecting W_0 as discussed before, the line width W_i observed in the raw data includes the instrumental broadening due to the spectrometer finite resolution W_r. This contribution must be deconvoluted from the total width W_i to obtain ΔW_D. Both widths can be approximately described as Gaussians, and therefore, the deconvolution is simply carried out by the following formula $\Delta W_D = \sqrt{W_i^2 - W_r^2}$.

A typical spectrum, taken with a 50 mA electron beam current at 6.82 T magnetic field, is shown in Fig. 4.5. Here, by using a polarizer, we separated both polarization directions and an independent measurement for each of them could be done. In Fig. 4.5a the four π - components are clearly resolved, while in Fig. 4.5b only the two σ - components appear. With this procedure, exploiting the polarization of the light, the emitted lines are better resolved and, therefore, they can be fitted with higher accuracy, as the residual plot shows. In Fig. 4.6 the same feature but at 20 mA electron beam current is displayed.

The results for the ion temperature obtained for two different electron beam currents I_e are collected in Table 4.2. By lowering the electron beam current the ion temperature clearly decreases, as observed in the reduction of the line width. However, the count rate also diminishes and, therefore, the statistical error becomes larger. This problem affects especially the π - components, as we cannot completely separate the four lines, and so the error in the determination of the line position and width is larger. In the σ-components case, as only two components do appear, the fits determine the line width with an error smaller than 4 % of the total width. The number of measurements made with the polarizer at low current is only one eighth of those taken at the higher current. The ion temperatures obtained here range approximately from 4×10^5 K to 0.7×10^5 K, or 6 eV to 30 eV. This temperature is a purely translational one, and the electronic excitation of the trapped ions is more or less completely decoupled from it, since the electrons are nearly monoenergetic with an energy defined by the acceleration potential.

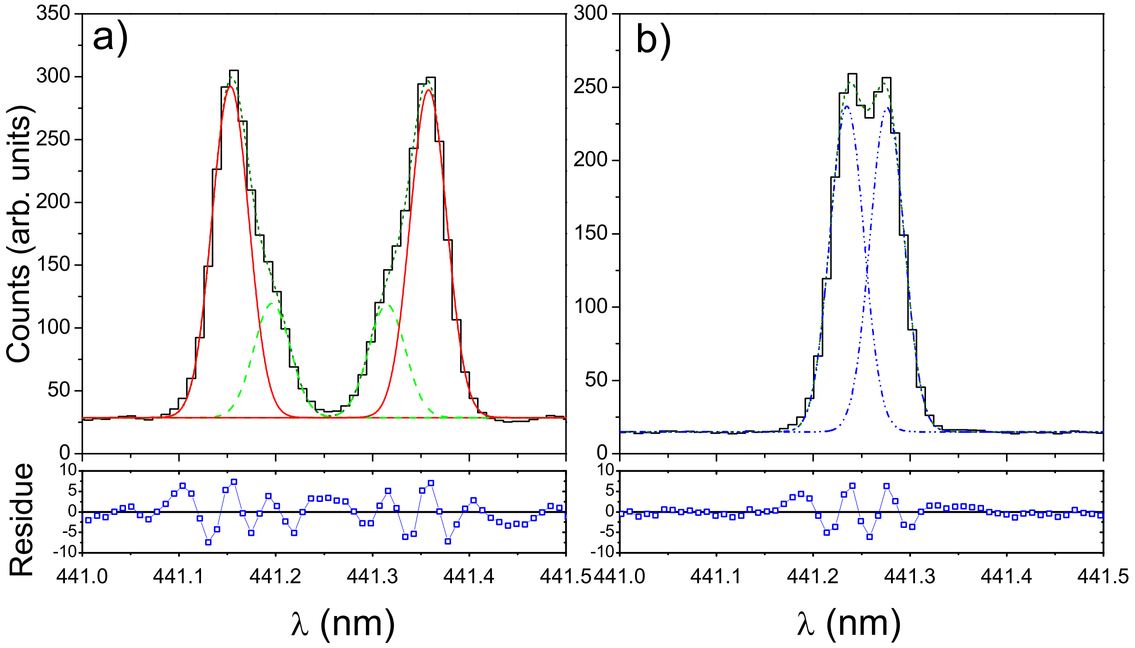

Figure 4.5: Spectra of a) π - and b) σ - Zeeman components of the M1 Ar^{13+} transition at $E_e = 875$ eV, $I_e = 50$ mA and 6.82 T, separated with a polarizer. The lower plots shows the fit residuals.

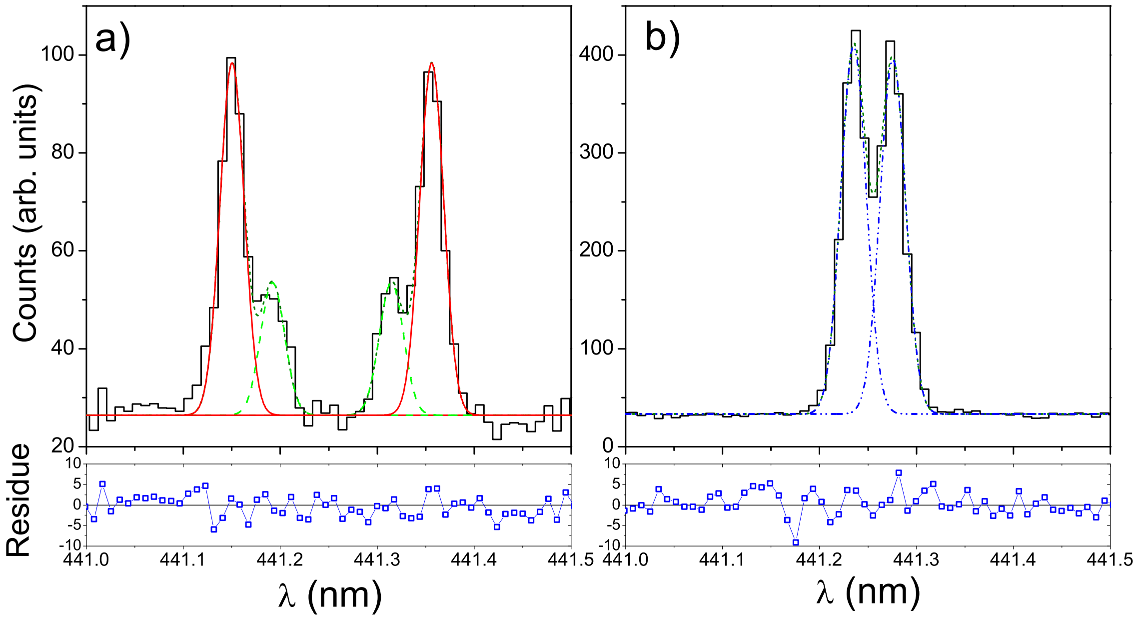

Figure 4.6: Spectra of a) π - and b) σ - Zeeman components of the M1 Ar^{13+} transition at $E_e = 875$ eV, $I_e = 20$ mA and 6.82 T, separated with a polarizer. The lower plots shows the fit residuals.

Table 4.2: Temperature of the trapped ions for different electron beam currents at 875 eV beam energy and 6.82 T

I_e[mA]	*Polarization*	ΔW_D[nm]	T_i[eV]
50	6 all components	0.024(1)	22(2)
	π	0.028(1)	30(2)
	σ	0.023(1)	20(2)
20	6 all components	0.013(1)	6(1)
	π	0.015(2)	9(2)
	σ	0.014(1)	7(1)

Magnetic field dependence

The line intensity of the emission lines is related to the transition probability A_{ik} in the following form

$$I = \hbar\omega A_{ik} = \frac{4}{3}\omega^4 c \sum_q \left|\langle J, M_J \left|\Pi_{1q}\right| J-1, M_J'\rangle\right| \quad , \tag{4.2}$$

where ω is the transition frequency, Π_{1q} the M1 decay operator (see Chapter 10 in [SM68]) and $q = M - M'$. The Wigner-Eckart theorem takes the form

$$\left|\langle J, M_J \left|\Pi_{1q}\right| J-1, M_J'\rangle\right| = (-1)^{J,M_J} \langle J||\Pi_1||J'\rangle \begin{pmatrix} J & 1 & J' \\ -M_J & q & M_J' \end{pmatrix}, \tag{4.3}$$

where $\langle J||\Pi_l||J'\rangle$ is the reduced matrix element, which does not depend on M_J and M_J' and, consequently q. Using this theorem, the relative line intensities of the different components can be calculated for an angle of observation of 90°. The results, obtained without taken into account any effect of the magnetic field strenght on the transition probabilities are given in Table 4.3.

The four upper levels (M_J), resulting from the fine structure splitting of the $J = 3/2$ level, are almost equally populated by cascades from higher levels and, therefore, they have similar intensity. In particular, the population of the M_J+ and M_J- sublevels are supposed to be identical. Using this simplifying assumption, the amplitudes for the different components were left free but fixed in pairs, *i.e.*, A_1 and A_6 amplitudes are assumed to be equal, $A_2 = A_5$ as well, and $A_3 = A_4$ during the fit in Fig. 4.4. The measured ratios, A_1/A_3 and A_2/A_3, are shown in Table 4.3. The

Table 4.3: Ratio between the amplitudes of the different transitions in Ar^{13+} ions

	Measured	***Corrected***	***Theory***
$A(\pi_{3/2})/A(\sigma)$	0.225(2)	0.484(4)	0.75
$A(\pi_{1/2})/A(\sigma)$	0.119(3)	0.256(4)	0.25

experimental results are corrected with the grating efficiency factor (obtained from Fig. 3.9) in the third column.

The intensity ratio $A(\pi_{1/2})/A(\sigma)$ does not depend on the level population being equal, since both transitions share the same upper level. Therefore, the branching ratio is purely dependent on the Clebsch-Gordon coefficients. Here, we find good agreement with theory. For the ratio $A(\pi_{3/2})/A(\sigma)$ however, the large disagreement indicates that the assumption of equal population of the M_J sublevels does not hold. This departure from equal population can arise through the excitation process, which does not only depend on electron impact from the ground state but also on cascades from higher lying levels and collisional mixing with energetically closed levels. Theoretical predictions for a particular set of experimental conditions would be very time consuming and not very reliable. Therefore, we do not have a satisfactory theoretical model for these observations. In the EBIT case, anisotropy can be a result of the preferred direction given by the magnetic field and the electron beam axis.

In Fig. 4.7 the predictions for $\Delta E_{J,M_J}(B)$ as a function of the magnetic field are shown. Here, the $g_J(B)$ were calculated using the large scale CI Dirac-Fock-Sturm method. A possible drift of the gravity center of the line which could be expected from this effect does not appear, due to the fact that the levels are split symmetrically with respect the center of gravity. Theoretically, the gravity center is shifted -0.00000324 nm, for σ- and $\pi_{1/2}$-components, and -0.00000162 nm, for the $\pi_{3/2}$-components, by increasing the magnetic field from 5 T to 8 T. Hence, no appreciable dependence on the magnetic field on the range under study is expected.

The transition probability of the different M_J levels has also been calculated using the large scale CIDFS method as a function of the magnetic field. These results are listed in Table 4.4 and show only a very weak magnetic field dependence. As the Zeeman splitting increases with rising the magnetic field strength, the changes in transition probability for the different components could cause a slight asymmetry of the Zeeman manifold, which then could result in a shift of its center of gravity. This effect, however, would be very small. At the given separation of the Zeeman

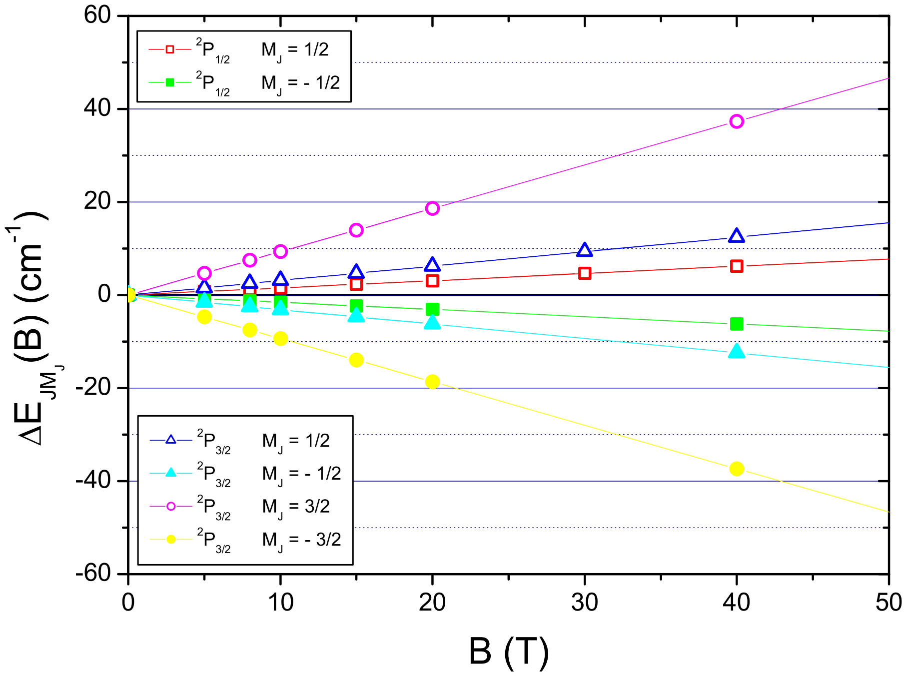

Figure 4.7: Calculated displacement of the different levels E_{J,M_J} of ${}^2P_{1/2}$ − ${}^2P_{3/2}$ transition of Ar^{13+} ions from the center of gravity E_J as a function of the magnetic field strength.

components it is estimated to be less than 10^{-4} nm. Moreover, since the intensity of the individual components its mainly determined by the excitation rate of the upper state, and not by the transition probability, the possible effect should be even smaller and thus, completely negligible at the current accuracy level.

Table 4.4: Calculated transition probabilities as a function of the magnetic field B, in s^{-1} units

$\boldsymbol{B}$(T)	$\boldsymbol{A}_{\sigma+}$	$\boldsymbol{A}_{\sigma-}$	$\boldsymbol{A}_{\pi+^{+}_{3/2}}$	$\boldsymbol{A}_{\pi+^{-}_{3/2}}$
0	104.362	104.363	104.363	104.363
5	104.366	104.359	104.445	104.280
8	104.368	104.357	104.494	104.231
10	104.370	104.355	104.527	104.198
40	104.391	104.334	105.023	103.705
100	104.434	104.291	106.021	102.725

Wavelength determination

From the six Gaussian functions used to fit the spectra three independent results for the determination of the central wavelength can be obtained. The extremely good resolution achieved allows us to determine the peak position with a very small error. To obtain the central wavelength from these six emission lines we proceeded as follows. First, for each line pair the average is built;

$$\frac{\left[\lambda(\pi^{+}_{3/2}) + \lambda(\pi^{-}_{3/2})\right]}{2} \equiv \lambda(\pi_{3/2}) \ , \tag{4.4}$$

where $\lambda(\pi^{+}_{3/2})$ and $\lambda(\pi^{-}_{3/2})$ correspond to the position of the first and last peak, respectively. Similarly, doing the same for the other two pairs of lines we get the second $\lambda(\pi_{1/2})$ and third $\lambda(\sigma)$ values of the central wavelength.

In Fig. 4.8 the resulting wavelengths are plotted for the different data sets. Here, we show an example of the CCD camera region 4 (remember that the camera is divided in 8 regions). Due to the small total number of counts and the influence of the neighboring peaks, the errors in the determination of $xc_{2,5}$ are larger than for the rest of the peaks. To obtain the overall wavelength we used the region 4, 5 and 6 and plot all the results together as shown in Fig. 4.9. By means of a constant fit, the final result for the wavelength for the $^2P_{1/2} - {}^2P_{3/2}$ transition in Ar^{13+} ions from this table is 441.2557(1) nm.

By using the polarizer, the same measurements were repeated for the π- and σ-components separately. Fig. 4.10 shows the results for the π-components and Fig. 4.12 the σ-components obtained from the CCD camera region 4. In Fig. 4.11 the results for the wavelength of the CCD camera region 4, 5 and 6 are shown for the π - components. As well, Fig. 4.13 shows the same for the σ - components. The results for $\lambda(\pi_{3/2})$ and $\lambda(\sigma)$ have always smaller error bars than the $\pi_{1/2}$ peak. Their larger error bars are due to the neighboring $\pi_{3/2}$ peak and to the fact that these peaks are weaker and, therefore, the uncertainty on the peak position is larger. From the π-components the resulting wavelength is 441.2554(1) nm and, from the σ-components 441.2556(1) nm.

An statistically weighted average is built to determine the wavelength and the corresponding statistical error. The accuracy of the calibration lines is of the order of 10^{-4} to 10^{-5} nm. Given that every single calibration uses several reference lines, the total error is mainly determined by the statistical error of the peak position determination, and possible systematics effects but not by the calibration uncertainty which is smaller. Possible sources of error coming from systematics or drifts are minimized

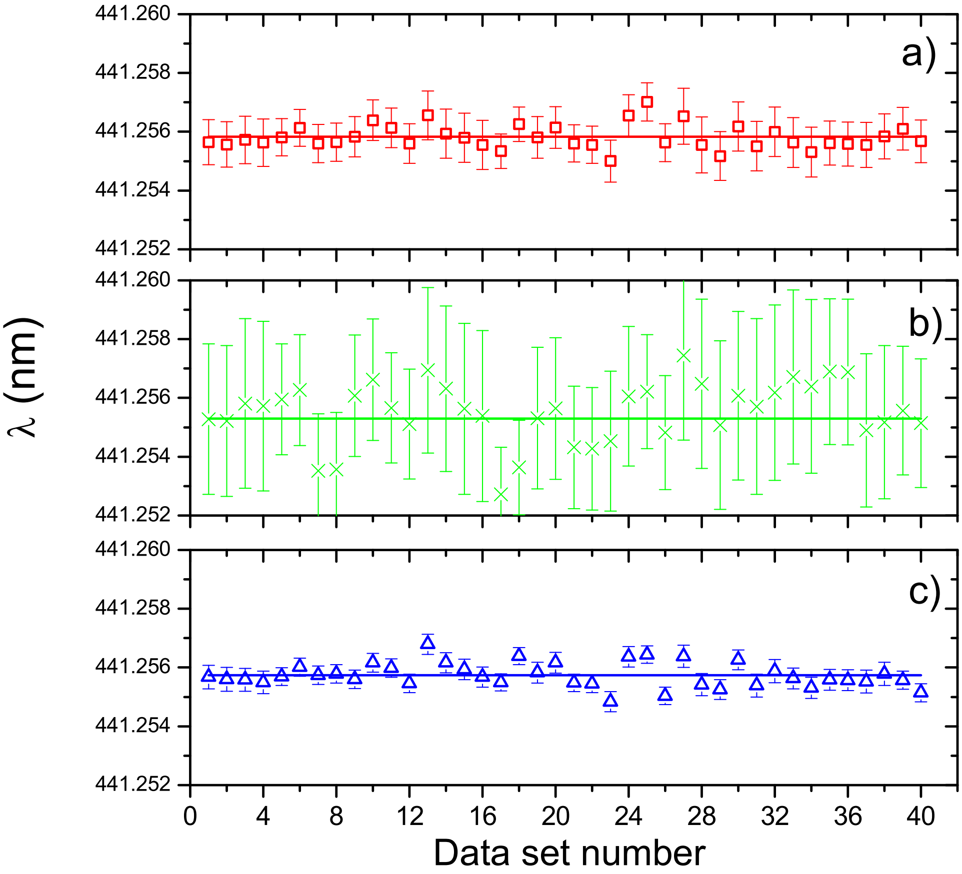

Figure 4.8: Wavelength results for a) $\lambda(\pi_{3/2})$, b) $\lambda(\pi_{1/2})$ and c) $\lambda(\sigma)$ of CCD camera region 4.

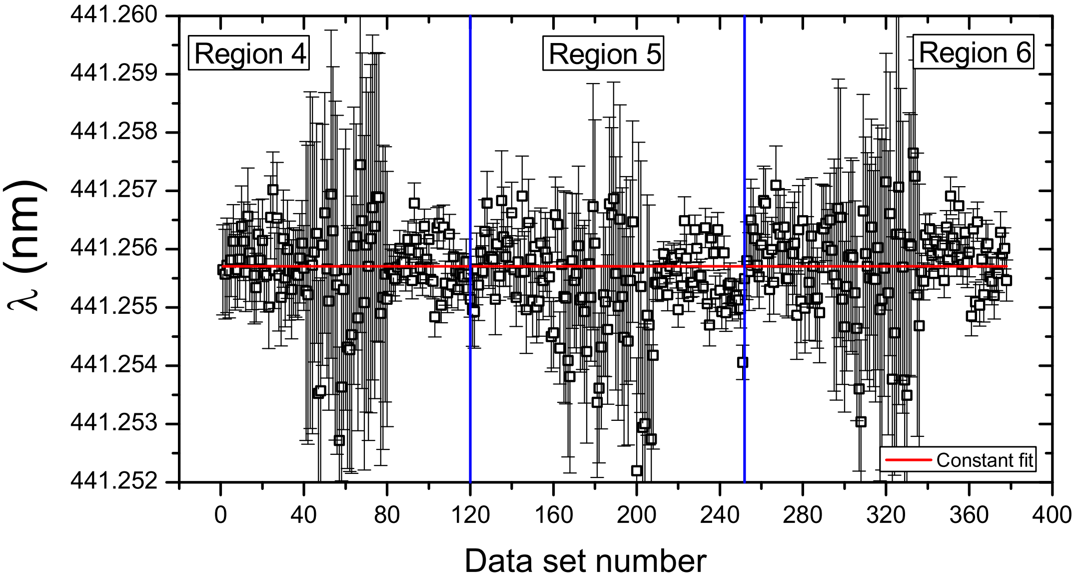

Figure 4.9: Wavelength results for the λ of CCD camera region 4,5 and 6, respectively.

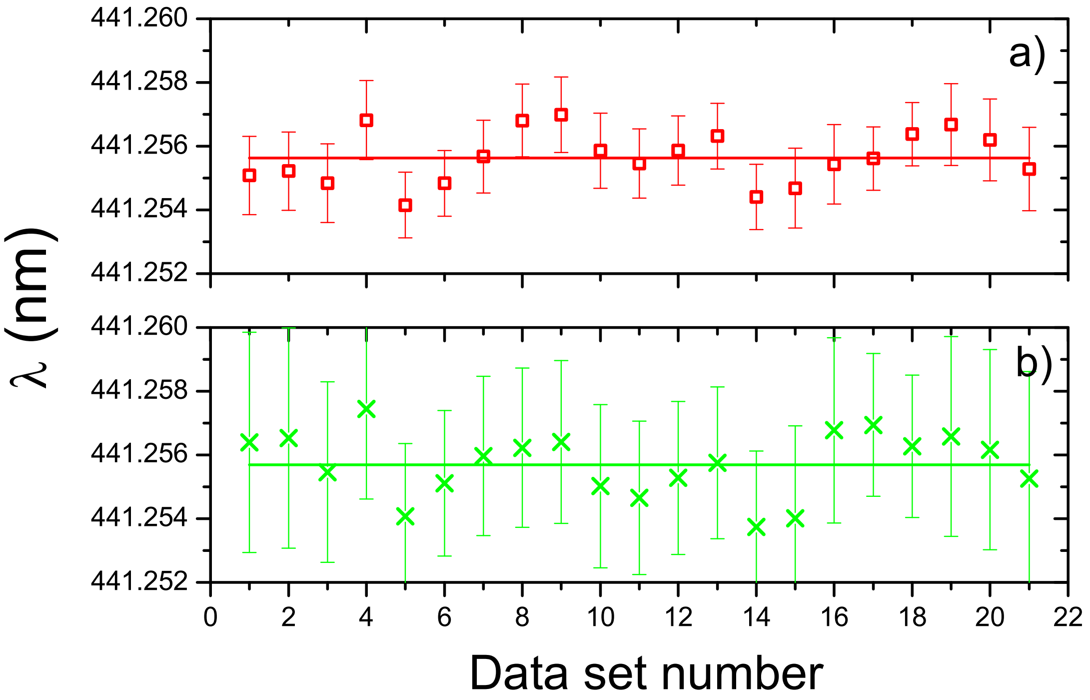

Figure 4.10: Results of the wavelength for a) $\lambda(\pi_{3/2})$, b) $\lambda(\pi_{1/2})$ of CCD camera region 4.

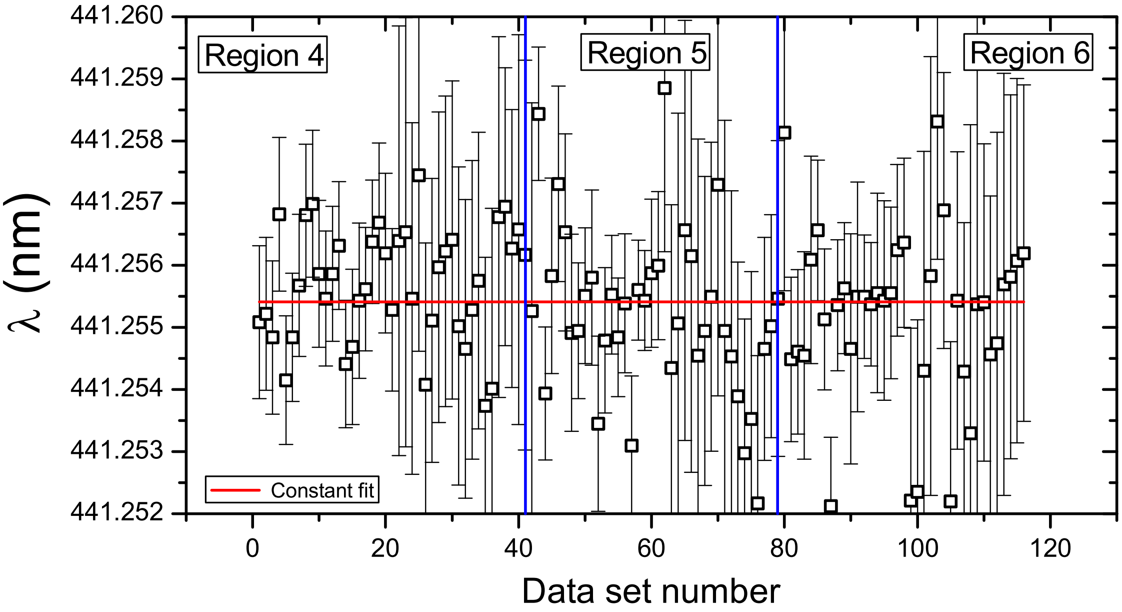

Figure 4.11: Wavelength results for the $\lambda(\pi)$ of CCD camera region 4,5 and 6, respectively.

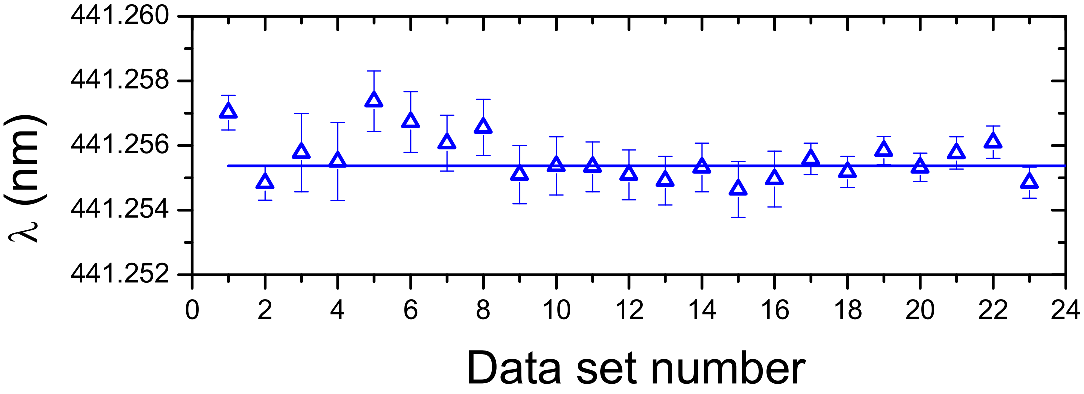

Figure 4.12: Results of the wavelength for $\lambda(\sigma)$ of CCD camera region 4.

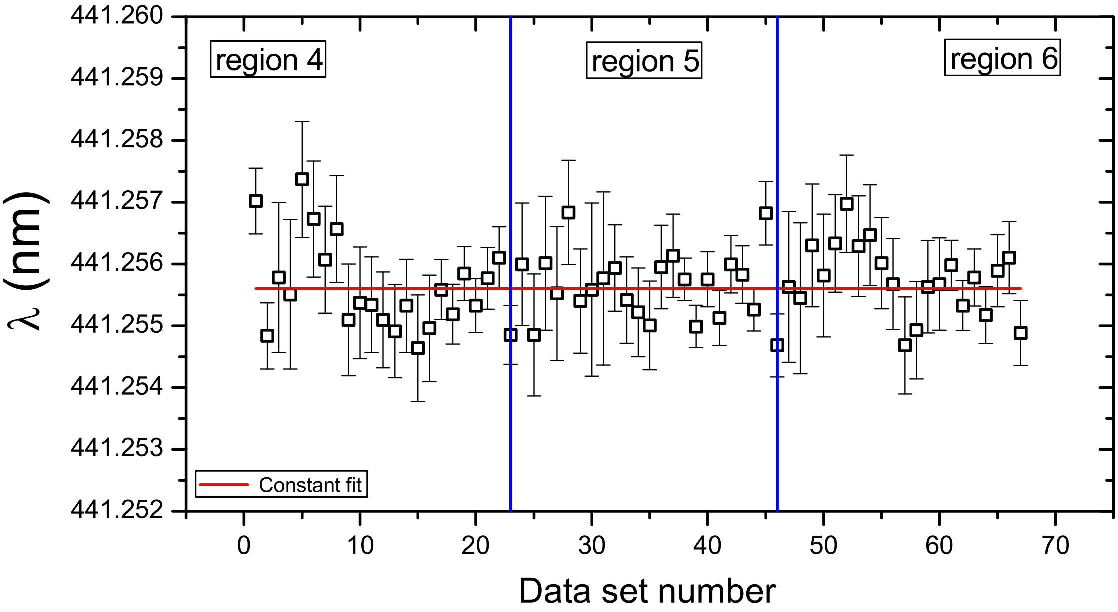

Figure 4.13: Wavelength results for the $\lambda(\sigma)$ of CCD camera region 4,5 and 6, respectively.

by the measurement procedure, which involves scanning the grating position and two calibrations for each single data point (see section 3.6). The reproducibility of the results along the 40 different points, together with the high resolution results in achieving a wavelength uncertainty for the final averaged wavelength below 0.3 ppm.

Forbidden transitions in Ar HCI have been studied in several works before. The highest experimental precision was achieved in a recent work performed by Draganić [DCD 03]. In that experiment, also carried out at the Heidelberg EBIT, the transitions of various charge states ($\mathrm{Ar}^{9+,10+,13+,14+}$) were measured with an average accuracy of better than 1 ppm. In Fig. 4.14 the results obtained in the present work are plotted and compared with previous experiments.

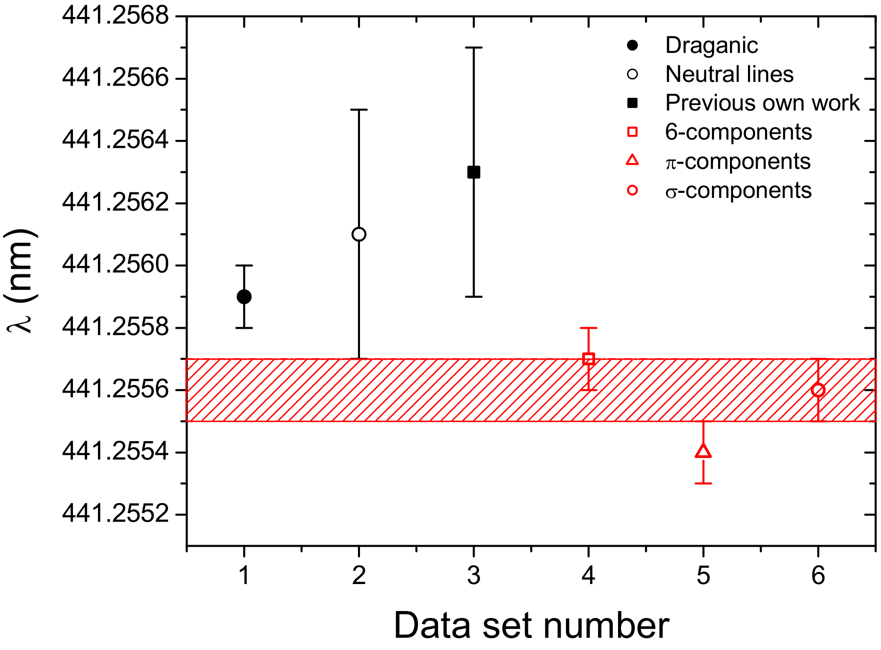

Figure 4.14: Comparison of the wavelengths obtained in previous measurements with the results of the present work. The open circle corresponds to an independent measurement with the calibration made using Ar II lines excited in the HD-EBIT. The solid square corresponds to a previous measurement were the Doppler broadening covered up the Zeeman splitting and, hence, the spectra were fitted with single Gaussian functions. These three points were obtained at 5.25 T magnetic field, while in the present experiment (red symbols) the magnetic field was 6.82 T. The shadowed area represents the average of the present experiment and its error bar.

Determination of the g_J-factor

The six emission lines observed in the spectrum for the $^2P_{1/2} - {}^2P_{3/2}$ transition of B-like argon ions are almost equally separated from each other. This splitting is used here to determine the g_J - factor. The energy splitting for the different M_J sublevels can be expressed as a function of the line separation as follows

$$\begin{aligned}
\Delta\lambda(\pi_{3/2}) &= \frac{hc}{\lambda^2}\left[\Delta E(3/2,3/2) - \Delta E(1/2,1/2)\right] \quad , \qquad (4.5)\\
\Delta\lambda(\pi_{1/2}) &= \frac{hc}{\lambda^2}\left[\Delta E(3/2,1/2) + \Delta E(1/2,1/2)\right] \quad , \qquad (4.6)\\
\Delta\lambda(\sigma) &= \frac{hc}{\lambda^2}\left[\Delta E(3/2,1/2) - \Delta E(1/2,1/2)\right] \quad , \qquad (4.7)
\end{aligned}$$

where the notation used corresponds to $\Delta E(J, M_J)$ and $\Delta\lambda(\pi_{3/2}) = \lambda(\pi^-_{3/2})$ - $\lambda(\pi^+_{3/2})$. Here we have a system of three equations with three unknowns which give us a determined system. By subtracting from the last equation the second one we obtain:

$$\Delta E(1/2,1/2) = \left[\frac{\Delta\lambda(\pi_{1/2}) - \Delta\lambda(\sigma)}{2}\right]\frac{hc}{\lambda^2} \quad , \qquad (4.8)$$

and if we substract from the last equation the second one and then we add the first one we obtain:

$$\Delta E(3/2,3/2) = \left[\frac{\Delta\lambda(\pi_{1/2}) - \Delta\lambda(\sigma)}{2} + \Delta\lambda(\pi_{3/2})\right]\frac{hc}{\lambda^2} \quad , \qquad (4.9)$$

As $\Delta\lambda(\pi_{3/2})$, $\Delta\lambda(\pi_{3/2})$ and $\Delta\lambda(\sigma)$ are obtained from the experiment, the g_J - factors can be expressed as

$$\begin{aligned}
\text{for } J = 1/2: \quad g_{1/2} &= \frac{\Delta E(1/2,1/2)}{\mu_B M_J B} \quad , \qquad (4.10)\\
\text{for } J = 3/2: \quad g_{3/2} &= \frac{\Delta E(3/2,3/2)}{\mu_B M_J B} \quad . \qquad (4.11)
\end{aligned}$$

In Fig. 4.15 the results obtained for the g_J - factors out of the spectra from three different CCD camera regions are shown along with theoretical predictions. The single data reproducibility results in a relatively small error bar for each independent region and for the averaged final value. The observed pairs of data correspond to the agreement between the two calibrations, before and after, made for each single data point. These error bars are the result of combining the uncertainties in the energy, in the magnetic field and of the Bohr-magneton, respectively. These large errors are mainly coming from the energies uncertainties since the μ_B is determine to 4×10^{-13} and the magnetic field precision (given by the company) is 5×10^{-4}. However, the experimental error still is too large to allow a critical comparison with theory, as shown in Table 4.5. Here, the g_D correspond to the one-electron Dirac g -factors, $\Delta g_{corr.}$ is the correction due to the interelectronic correlation, $\Delta g_{neg.}$ is the contribution due to the negative continuum spectrum (which were both calculated applying CI methods to the Hartree-Fock-Dirac-Sturm wave functions), and Δg_{QED} is the QED correction.

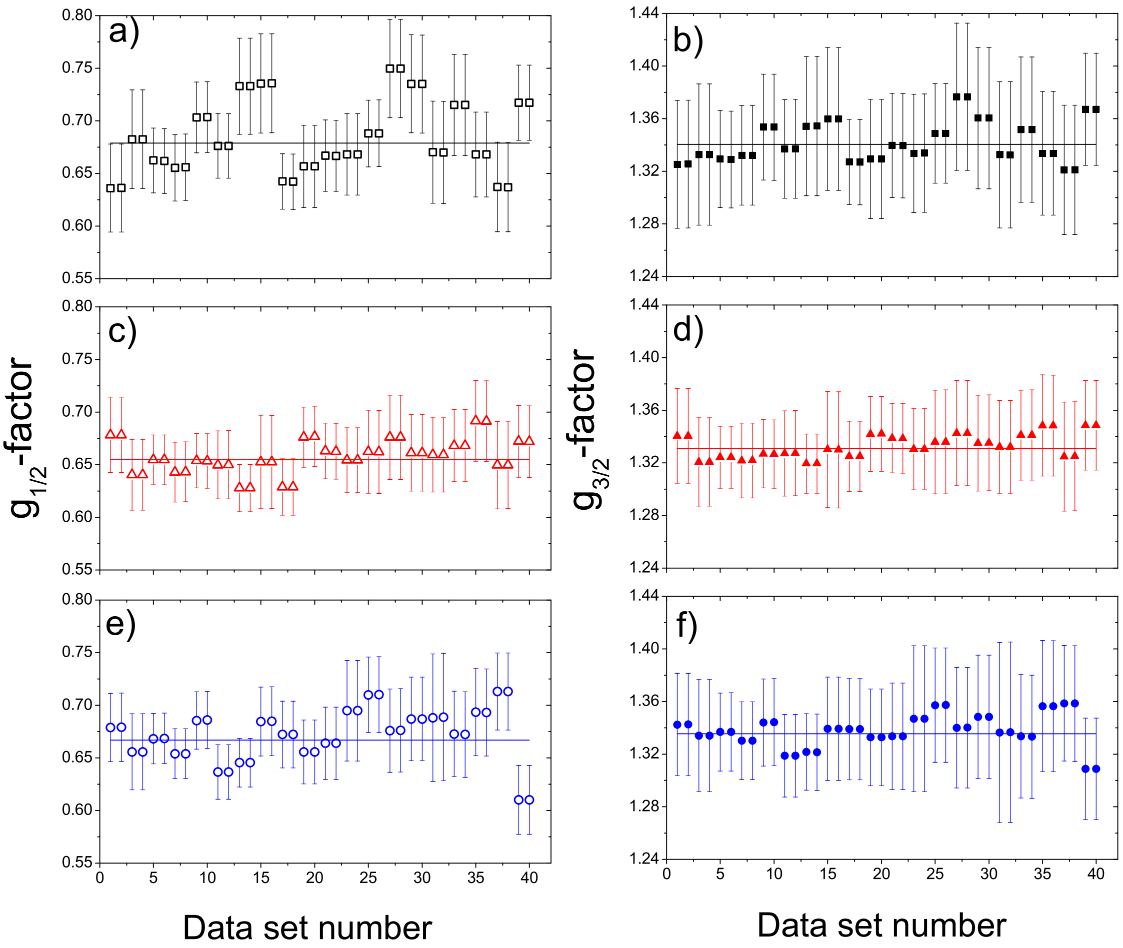

Figure 4.15: Experimental values of the g_J-factor obtained from data taken from the regions 4, 5 and 6 of the CCD camera. The left plots (open symbols) corresponds to $g_{1/2}$ and the right plots (solid symbols) are the results for $g_{3/2}$. Figs. 4.15a) and b) correspond to region 4, Figs. 4.15c) and d) to region 5 and Figs. 4.15e) and f) to region 6.

Table 4.5: Contributions to the total g-factor as calculated with the CI-HFDS method and comparison with the experiment result

State	g_D	$\Delta g_{corr.}$	$\Delta g_{neg.}$	Δg_{QED}	g_{total}	$g_{exp.}$
$^2P_{1/2}$	0.6637754	0.0006730	0.0000224	-0.00078	0.6636908	0.663(7)
$^2P_{3/2}$	1.3310304	0.0005519	0.0000687	0.00077	1.3324210	1.333(2)

4.1.2 Be-like argon

In the case of Be-like argon, the lines were fitted with a single Gaussian function using the same procedure for the error estimation as explained before. In Fig. 4.16, an average spectrum of three regions is shown. Here, it is possible to see the Zeeman splitting which in this transition corresponds to 9 emission lines. Though we see only three peaks, there are more transition lines under each peak (see Fig. 4.2). Due to the low resolution the best fit with the smallest residuals is obtained by using just only three Gaussians. The resulting wavelength is 594.3879(2) nm, in excellent agreement with the previous result 594.3880(3) nm obtained by Draganić [DCD 03].

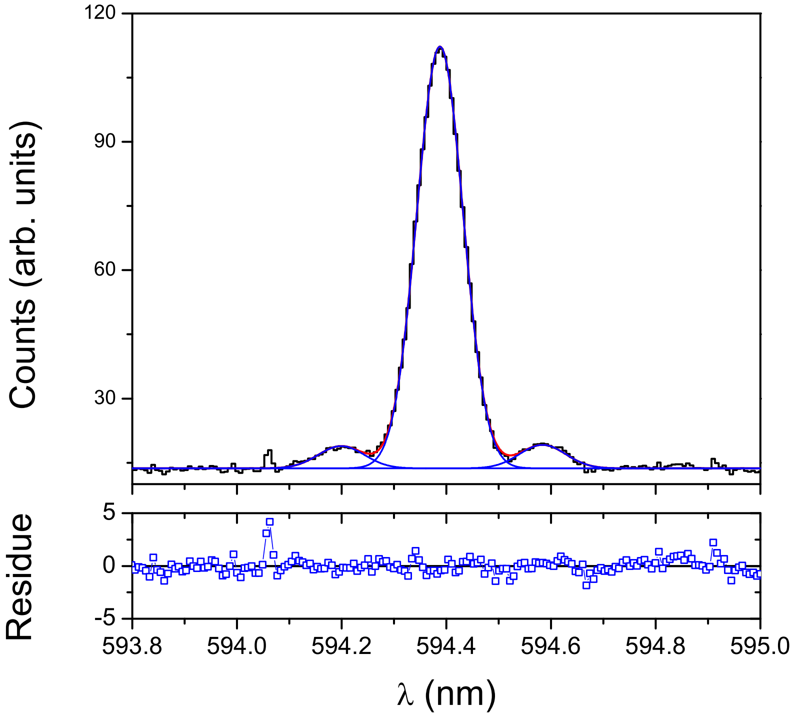

Figure 4.16: Average spectrum for the transition $^3P_2 - {}^3P_1$ in Ar^{14+} ions taken at $E_e = 1.01$ KeV, $I_e =$ 88 mA and 8 T. The lower plot shows the fit residuals.

4.2 Isotopic shift in ^{36,40}Ar

Argon was discovered by Lord Raleigh and Sir Williams Ramsay in 1894. The origin of the name comes from the Greek word *argos* meaning *inactive*. It is a colorless and odorless noble gas, *i.e.*, chemically inert. Its atomic mass is 39.948(1) and it has five stable isotopes, ^{36}Ar, ^{37}Ar, ^{38}Ar, ^{39}Ar and ^{40}Ar. The most common one is ^{40}Ar, with a relative abundance of 99.600(3) %, compared with 0.0632 (5) % for ^{38}Ar and 0.337(3) % for ^{36}Ar. For this measurement of the isotope shift, the pair ^{40}Ar/^{36}Ar was chosen. The ^{40}Ar sample used was nearly pure, with 99.998% ^{40}Ar. The ^{36}Ar gas sample mass spectroscopic analysis gave a relative composition of 99.7 atom % ^{36}Ar and, 0.3 atom % ^{40}Ar.

For the first measurement, ^{36}Ar gas was injected into the trap region. Then, before switching to the other isotope, the gas injection system was pumped out to avoid isotopic contamination. Furthermore, by extracting ions out the trap and measuring their q/m ratios by means of an analyzing magnet, it was checked that no residues of this isotope were still present in the trap before the ^{40}Ar injection started. Fig. 4.17 displays the count rate for the different charge states as a function of the voltage applied to the analyzing magnet. It can be seen that the extracted ions confirm the isotopic purity of the trapped ions to a high degree as well as the absence of other contaminants except for C^{q+} and O^{q+} ions, which have no interfering emission lines over the investigated wavelength region. These tests were carried

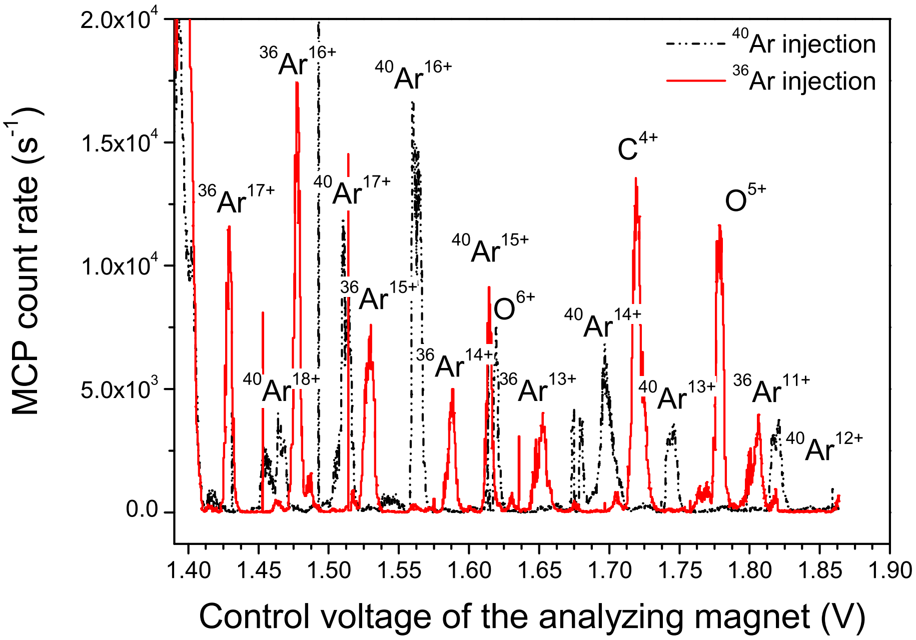

Figure 4.17: q/m analysis of the argon ions extracted from the trap region.

out at higher electron beam energies for reasons of extraction efficiency. Thus, they also show ions in charge states as high as Ar^{18+}. Note that the relative intensities of different charge states are similar in both cases. A few sharp spikes are due to the dumping of the trap.

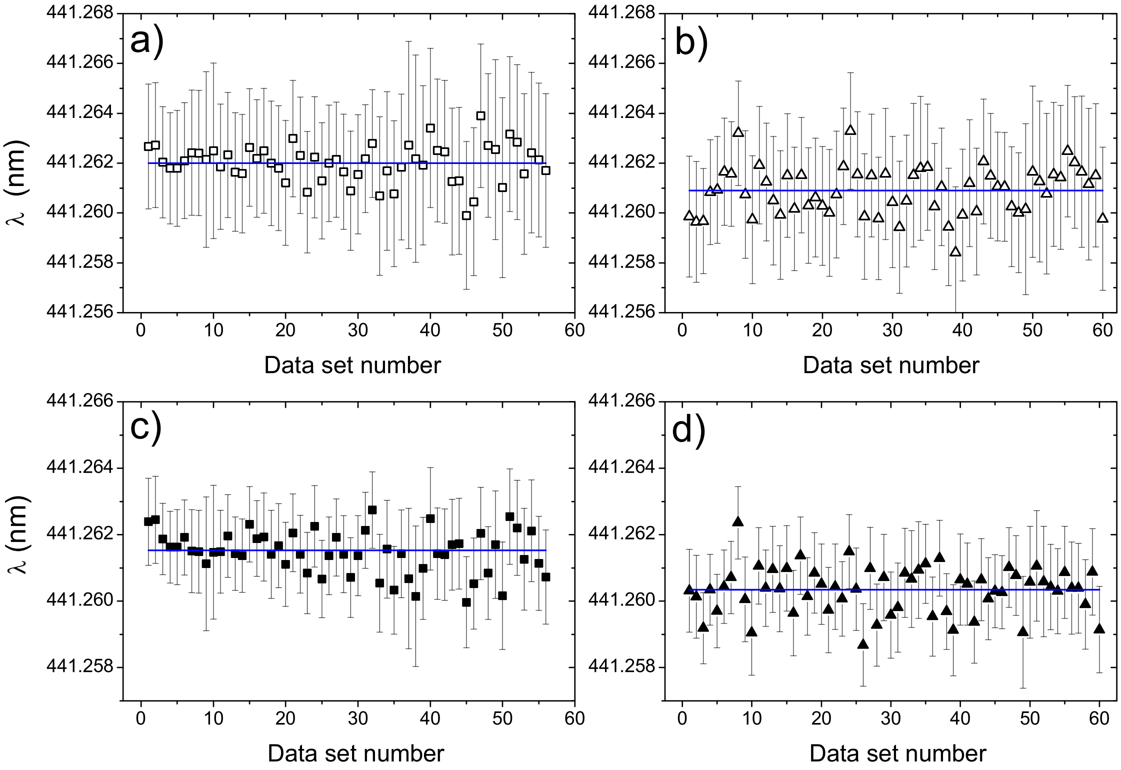

Figure 4.18: Wavelengths obtained for a) and b) $\pi_{3/2}$-components and, c) and d) σ-components for ^{36}Ar^{13+} and ^{40}Ar^{13+}, left and right column, respectively, from the CCD camera region 5.

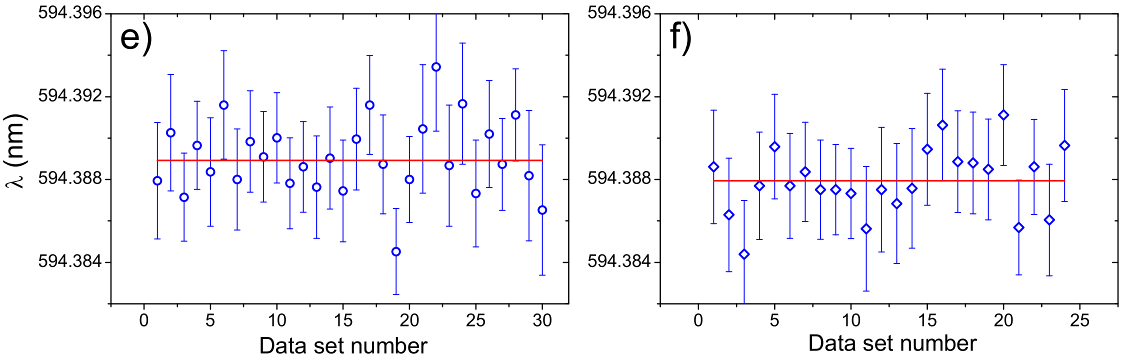

Figure 4.19: Wavelengths obtained for ^{36}Ar^{14+} and ^{40}Ar^{13+}, in Figs. e) and f), respectively, from the CCD camera region 3.

In order to determine the isotopic shift between the ^{40}Ar/^{36}Ar, all regions of the CCD camera could be used, as only the differences between wavelengths had to be measured. The notation used here corresponds to the difference between each two wavelengths as $\lambda(^{36}\mathrm{Ar})$ - $\lambda(^{40}\mathrm{Ar})$. The results obtained in the CCD camera region 5 for B-like argon ion transitions in both isotopes and polarization directions ($\pi-$ and σ-components) are plotted in Fig. 4.18 for illustration. A careful comparison of the plots reveals that the data points of the right hand figures are shifted down by a small amount, compared to the left column. The Be-like argon ion transition is shown in Fig. 4.19. Due to the width of the recorded line, which was the consequence of a higher ion temperature and the use of a wider entrance slit during that measurement, a single Gaussian function had to be used and, hence, only a single data point for the determination of the isotopic shift was obtained out of each region. Fig. 4.19e corresponds to the ^{36}Ar and Fig. 4.19f to the ^{40}Ar isotope, respectively. The isotopic shifts resulting from the differences between the wavelength measured at different CCD camera regions in B-like are shown in Fig. 4.20. The results for Be-like are shown in Fig. 4.21.

As was explained before in Sec. 1.6, the isotopic shift contains contributions of the mass and the field shift. Results of very recent relativistic calculations carried out for Be-like and B-like argon ions, with the different contributions, are shown in Table 4.6. The isotopic mass shift includes both the normal (NMS) as well as the specific mass shift (SMS), which were calculated using Dirac wave functions, and the relativistic operator correction for each of them, $RNMS$ and $RSMS$, respectively. To calculate the field isotope shift, the *rms* nuclear radii given in [FBH 95] were used. The transition energies are essentially determined by relativistic, QED and electron correlation effects. But, it can be seen clearly that relativistic recoil corrections are needed to come to a proper evaluation of the isotopic mass shift. For the ions under consideration calculations predict that this shift strongly dominates over the field shift. This results from the fact that the active electron is in a $2p$ orbital, which has only a small overlap with the nucleus, thus making the overall effect very small.

Table 4.6: Calculated individual contributions to the isotope shifts in ^{40}Ar/^{36}Ar of the forbidden lines of Ar^{13+} and Ar^{14+}. The *rms* nuclear charge radii used in the calculation are $< r^2 >^{1/2}$ = 3.390 and 3.427 (fm) [FBH 95] for ^{36}Ar and ^{40}Ar, respectively. The figures are given in cm^{-1}

Ion	***NMS***	***SMS***	***RNMS***	***RSMS***	***FS***	***Total***
Ar^{13+}	0.1053	-0.0742	-0.0822	0.1151	-0.0005	0.0635
Ar^{14+}	0.0797	-0.0698	-0.0627	0.0887	-0.0001	0.0358

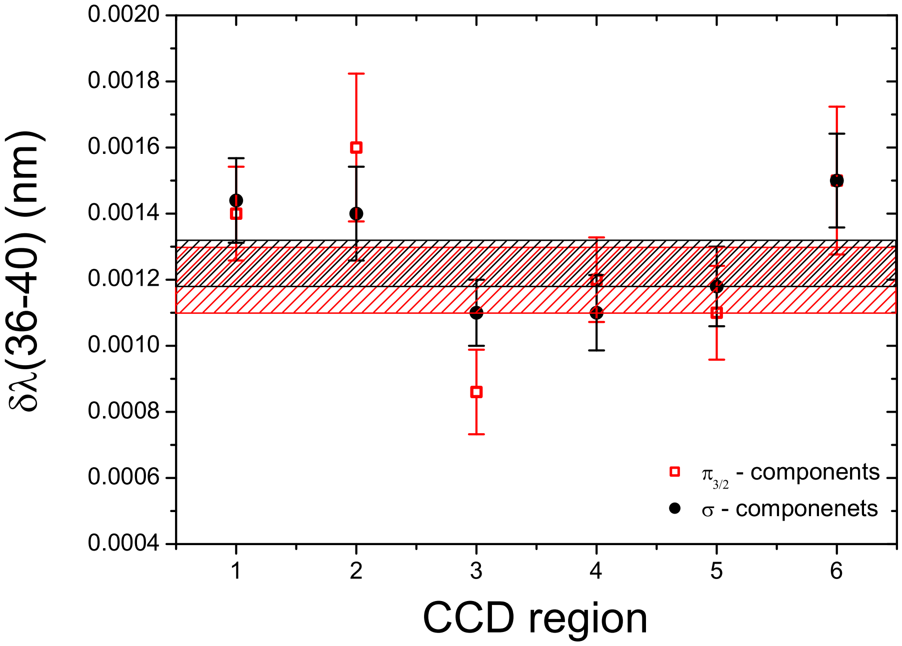

Figure 4.20: Isotopic effect in B-like argon measured at different CCD camera regions. The shadowed area in red represents the resulting average and its error, for the $\Delta\pi_{3/2}$ components and, the shadowed area in black corresponds to the average obtained for the $\Delta\sigma$ components.

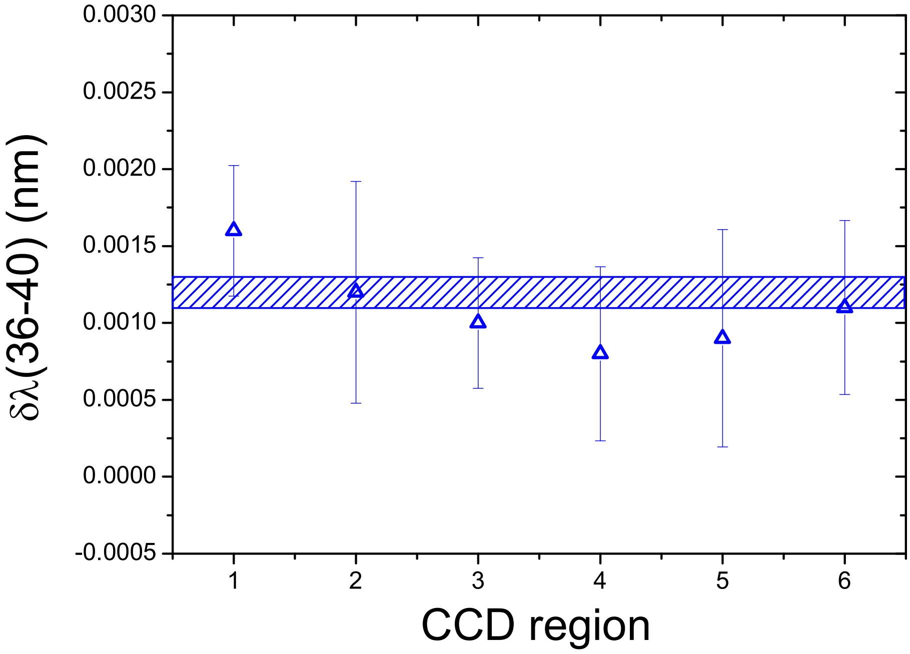

Figure 4.21: Isotopic effect in Be-like argon measured at different CCD camera regions. The shadowed area indicates the average of the 6 regions and its error bar.

Table 4.7 summarizes the present experimental and theoretical results for the wavelengths of the ^{40}Ar isotopes, as well as the isotope effects for the ^{40}Ar/^{36}Ar pair for Ar^{13+} and Ar^{14+} ions, together with other theoretical predictions of the overall wavelength [SJS96a, SJS96b]. The values shown in the second column are obtained using relativistic many-body perturbation theory. These calculations were carried out to second order in perturbation theory, including both the second-order Coulomb interaction and the second order Breit-Coulomb interaction. While the correction for the frequency-dependent Breit interaction was taken into account in lowest order, the effect of the Lamb shift was estimated from a calculation in a local central potential that approximates the core HF potential. In the third column the present theoretical results are shown. They have been calculated with the large-scale CI Dirac-Fock (DF) method used to solve the Dirac-Coulomb-Breit equation. Meanwhile, the QED corrections were evaluated using the one-electron Lamb shift data taken from [JS85]. In theory, the large uncertainties are mainly due to the uncertainty in the electronic correlation and QED corrections. The fourth column shows the present experimental results, in comparison with the far less accurate (2-3 orders of magnitude) predictions. They are in agreement with each other within their large uncertainty limits. The theoretical and experimental results for the isotope shifts are also listed. The theoretical uncertainty for the present calculations of the isotopic shift appears in the last figure and is smaller than the experimental error. The contribution to the theoretical uncertainty coming from the finite size and finite mass of the nucleus (isotopic correction) can be determined with good accuracy. The large theoretical error contributions to the total transition energy arising from the relativistic, correlation and QED corrections, respectively, are approximately the same for both isotopes and, hence, they cancel each other out.

Experimentally, in the case of Ar^{13+}, the Zeeman splitting and the excellent resolution achieved, as explained above, lead to a small error allowing, for the first time, to observe these effects in HCIs. In particular, for the σ-components, the error

Table 4.7: Transition energies for Ar$^{13+,14+}$ and isotope shifts in ^{40}Ar/^{36}Ar (in nm).

	Wavelength			***Isotope shifts***	
Ion	***Theory***		***Experiment***	***Theory***	***Experiment***
Ar^{13+}	440.99[1]	441.16(27)	441.2556(1)	0.00126	0.0012(1)* 0.00125(7)**
Ar^{14+}	593.88[2]	594.24(30)	594.3879(2)	0.00136	0.0012(1)

[1,2] [SJS96a, SJS96b]. * π-components. ** σ-components

is as small as 6 % of the total shift, and in good agreement with the current theory. Even for the weaker π-components of the Ar^{13+} line, and also in the case of the weak Ar^{14+} transition, the error bars are not much larger, namely about 8 %. The experimental values are sligthly lower than the theoretical predictions.

Conclusions

The central result of this work is the first experimental study of relativistic nuclear recoil corrections in highly charged ions by means of spectroscopic isotope shift measurements. These effects are extremely small, namely of the order of 2 ppm. Until recently, no wavelenght measurement in HCI had achieved the accuracy needed for such a study. The favourable and stable conditions of the Heidelberg EBIT, combined with the precise instrumentation used in this experiment and the sophisticated calibration procedures developed in this work, made possible to reach an accuracy at the sub ppm level, thus making the detection of such minuscule effects possible.

Relativistic bound electrons, as those responsible for the optical forbidden transitions in Be-like Ar^{14+} (Ar XV) and B-like Ar^{13+} (Ar XIV), display a behaviour in their dynamic interaction with the nucleus which is completely different from the one found in neutral atoms and low-charge ions. To the extensively investigated normal mass shift and specific mass shift, large corrections due to relativity have to be added. In fact, the corrections are as large as the non-relativistic effects by themselves, and have even opposite signs, at least for the cases here investigated. Calculations for these relativistic contributions in many-electron systems are far from trivial, and only very recently systematic problems in the customarily applied algorithms have been eliminated. On the other side, no experimental results were available to compare with. This work has delivered, for the first time, measurements of the isotope shift with an accuracy allowing a critical comparison with these newest calculations.

Moreover, the low ion temperature achieved in the present experiment, allowed us to observe the Zeeman splitting of the investigated fine structure $^2P_{3/2}$ - $^2P_{1/2}$ M1 transition in the B-like argon ions also for the first time.

Such for HCI untypically low translational temperatures of few eV, and the fact that these ions can be produced with relative ease in an EBIT makes this device the best target for high precision optical measurements with HCI, in particular when interactions with radiation are planned, as the case in the evolving experiments at the VUV FEL (DESY) or the laser spectroscopic experiments in Heidelberg.

Regarding the study of QED contributions to the g-factor of the bound electron, and although the present experimental wavelength data have the highest accuracy reported for HCI, they do not yet allow to determine the g-factors with an accuracy enabling to evaluate the quality of theoretical predictions. The reason for that is the fact that their values are obtained as a combination of the differences between the energy transitions (splitting) for the different σ- and π-components, respectively, yielding uncertainties of 1 % for $g_{1/2}$ and 0.2 % for $g_{3/2}$. Nonetheless, the remark must be made that theoretical predicitions show 0.12 % and 0.06 % QED contributions for the $g_{1/2}$, $g_{3/2}$-factors, respectively, and hence, experimental improvements which can be attained realistically in the near future will provide new results relevant to the QED calculations.

From the Zeeman splitting in B-like argon we also obtained three new independent values for the transition energy, which due to the good resolution were determined with high accuracy.

The values measured here are in good agreement, but slightly below the previous experimental results by Draganić [DCD 03]. However, our results have achieved a reduction of the experimental error as a consequence of the increased resolution. The experimental uncertainty is, presently, mainly limited by the spectrometer resolution. In order to improve it, an immediate option is to use a spectrometer with a larger focal length and also improved CCD detectors with an smaller pixel size and larger array. However, the best outlook on the long run will be laser spectroscopy. By exciting trapped, cooled ions with extremely monoenergetic beams, the resolution can be improved, in theory, tremendously, since the lifetimes of the forbidden transitions in HCI are very long [LJC 05], several milliseconds typically, in comparison with the allowed transitions of neutral atoms and low charged ions, and natural line widths of few tens of Hz can be expected. Additionally, highly charged ions are very insensitive to external fields, since their electronic structure is dominated by the strong Coulomb field of the nucleus, which results in a very low polarizability. Eventually, an optical transition of an HCI could be used as an extremely stable frequency standard. Meanwhile, HCI provide unique opportunities for the study of the QED contributions to the transition energy, the Lamb shift, the g-factor, the dynamics of complex relativistic systems, and the nuclear size effects, as this work has shown.

Appendix A

Optical aberrations

An optical aberration is a distortion in the image formed by an optical system compared to the original. They arise due to the limitations of lenses and mirrors in optical setups. There are six aberration: Chromatic, spherical, astigmatism, field curvature, distortion and coma aberration.

A.1 Chromatic aberration

A lens has different index of refraction for different wavelengths. This causes the light rays to pass through different focal points according to the wavelength.

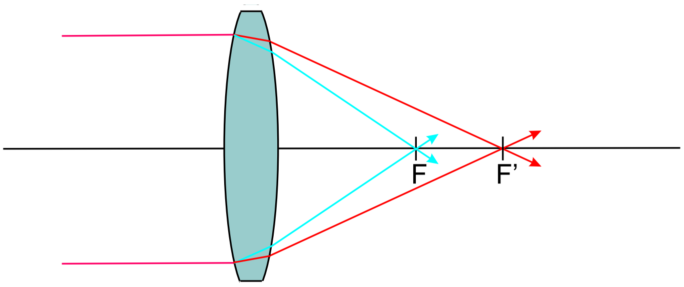

Figure A.1: Illustration of the chromatic aberration of a lens. The F and F’ represent the different focal points.

A.2 Spherical aberration

Spherical aberration occurs in spherical lenses or mirrors because rays on the edges of the lens or mirror are brought to a focus slightly before that of rays hitting the center of the optical element, as shown in Fig. A.2. Due to the CT spectrometer configuration this type of aberration is largely reduced.

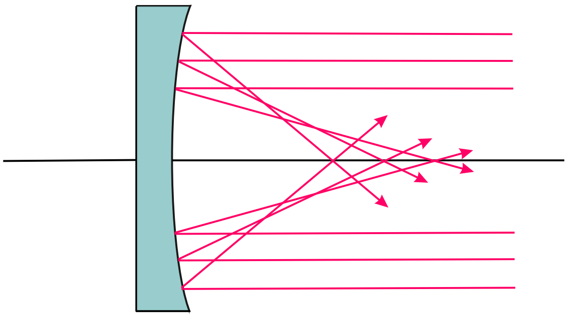

Figure A.2: Illustration of the spherical aberration caused by a concave mirror.

A.3 Astigmatism aberration

This is caused because the focal length along one diameter differs from that along another, resulting in a distortion of the image. In particular, rays of light from horizontal and vertical lines in a plane on the object are not focused to the same plane on the edges of the image.

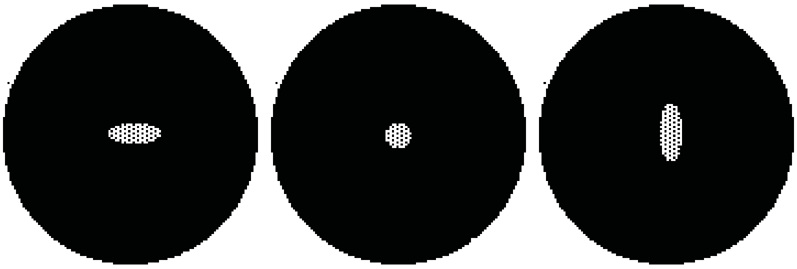

Figure A.3: Astigmatism aberration, from left to right : inside focus (sagittal), best focus, outside focus (tangential).

Appendix B

LabVIEW program

B.1 Analysis program

Due to the amount of spectra needed to be analyze a program using LabVIEW 7 Express was made by Bruhns [Bru05]. In Fig. B.1 the front panel of the program is shown. The program block diagram of this front panel is shown in Fig. B.2. The main program is shown in Fig. B.3. This library file is composed of several subprograms which main block diagrams are shown in Figs. B.4, B.5, B.6 and B.7, respectively.

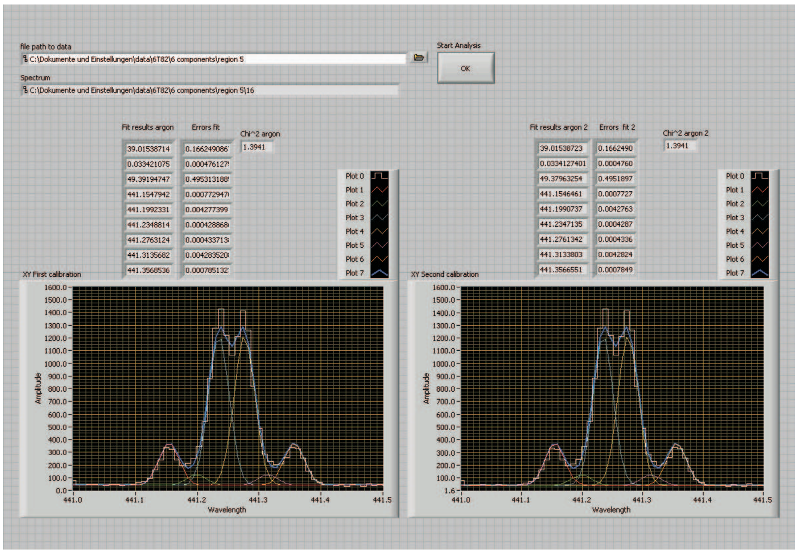

file path to data: C:\Dokumente und Einstellungen\data\6T82\6 components\region 5

Spectrum: C:\Dokumente und Einstellungen\data\6T82\6 components\region 5\16

Fit results argon	Errors fit
39.01538714	0.166249086
0.033421075	0.000476127
49.39194747	0.495313188
441.1547942	0.000772947
441.1992331	0.004277399
441.2348814	0.000428868
441.2763124	0.000433713
441.3135682	0.004283520
441.3568536	0.000785132

Chi^2 argon: 1.3941

Fit results argon 2	Errors fit 2
39.01538723	0.1662490
0.0334127401	0.0004760
49.37963254	0.4951897
441.1546461	0.0007727
441.1990737	0.0042763
441.2347135	0.0004287
441.2761342	0.0004336
441.3133803	0.0042824
441.3566551	0.0007849

Chi^2 argon 2: 1.3941

Figure B.1: Front panel program showing the two calibration spectra, before and after, respectively, made for each single point. In the worksheets, the results of the fitted curves together with their corresponding error bars are listed.

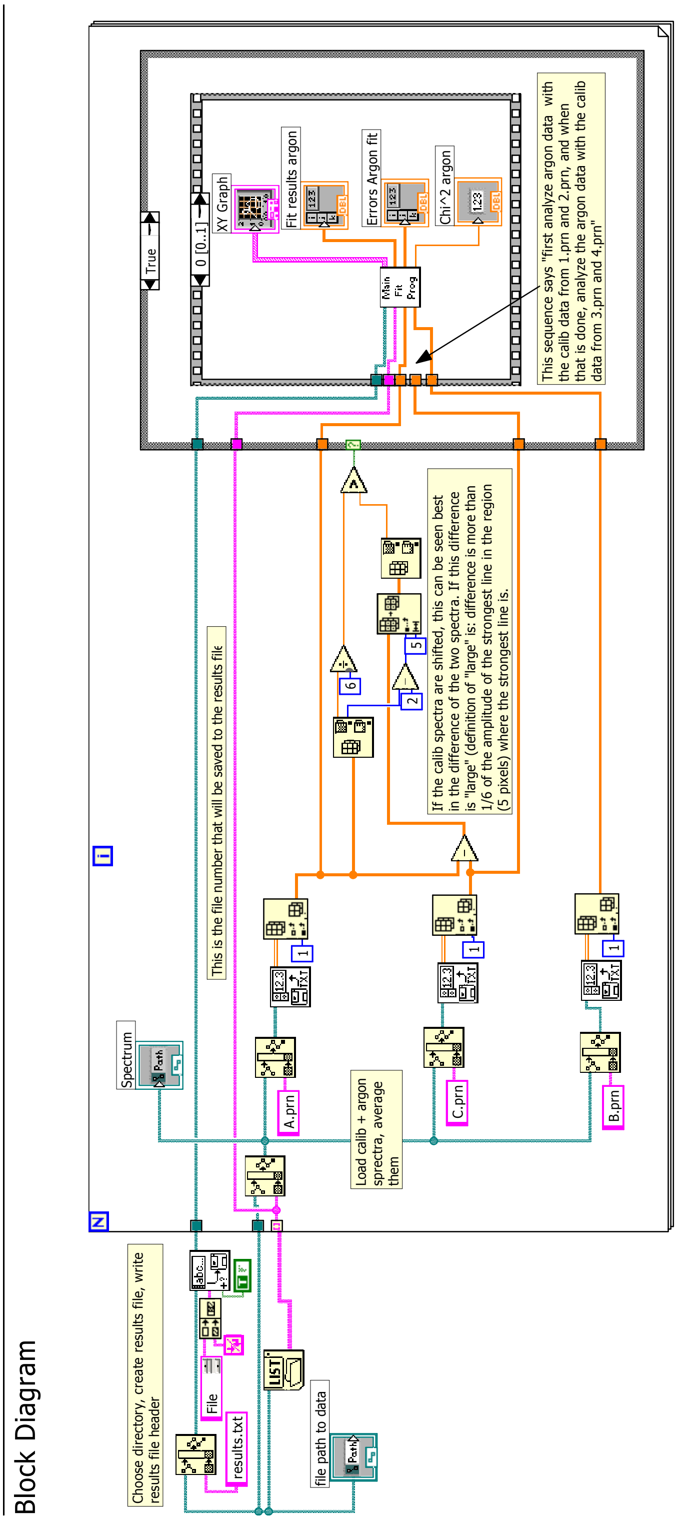

Figure B.2: Program block diagram for the loading data process from a file to be analyze. The calibrations are named A and C, before and after, respectively, and the ion spectrum corresponds to the named file B.

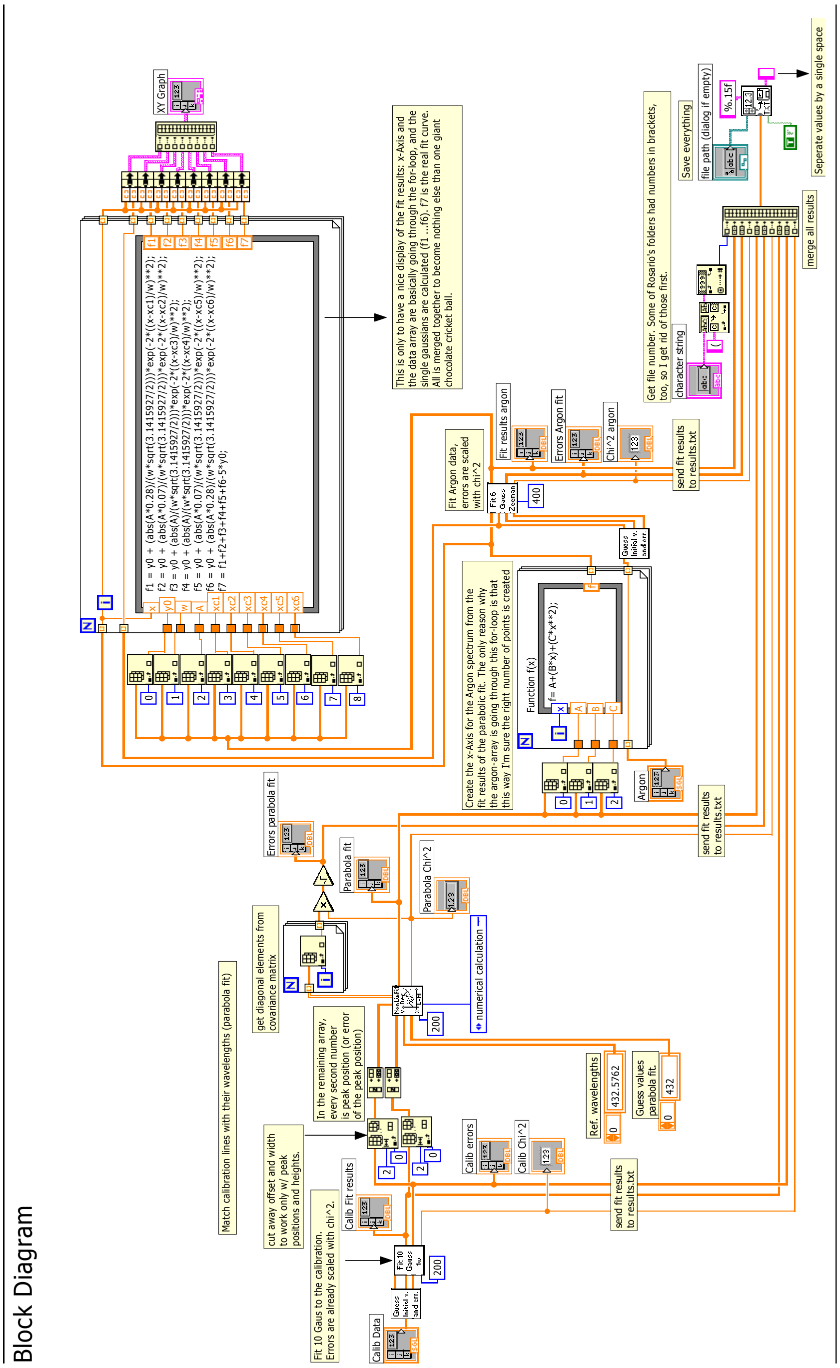

Figure B.3: Main program block diagram. The calibration spectra are fitted to 10 Gaussian function and a preliminary guess values for the offset, width, amplitude and peak position, are given. After the parabola fit made to obtain the spectrometer dispersion function, a 6 Gaussian function is fitted to the ion spectrum, with a preliminary guessing of the offset, width, amplitude and peak position values. All the results are recollected and save under the name result.txt on the same folder where the data are store.

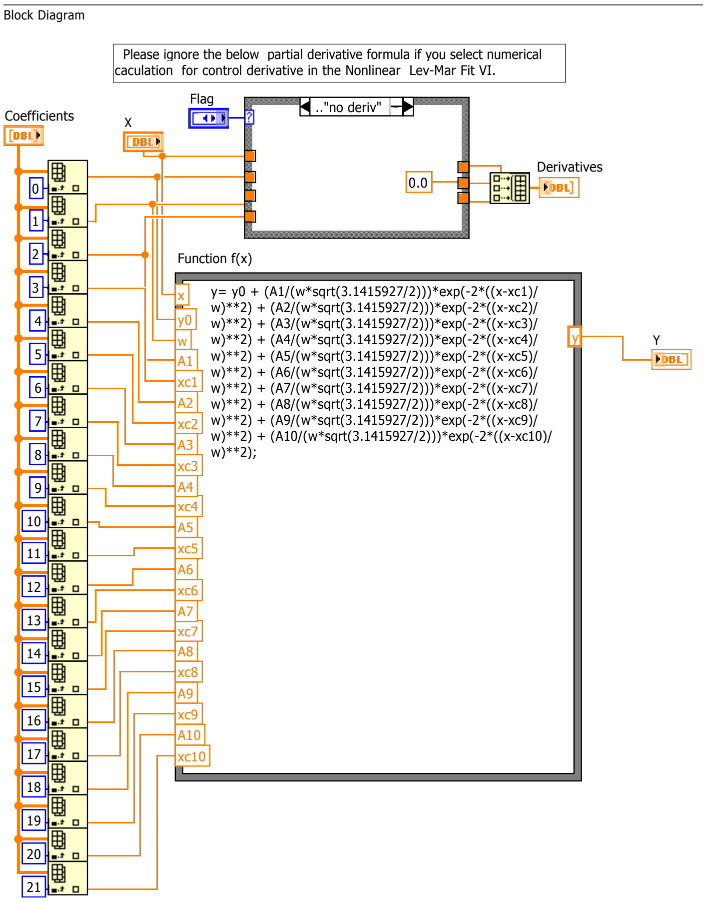

Please ignore the below partial derivative formula if you select numerical caculation for control derivative in the Nonlinear Lev-Mar Fit VI.

```
y= y0 + (A1/(w*sqrt(3.1415927/2)))*exp(-2*((x-xc1)/
w)**2) + (A2/(w*sqrt(3.1415927/2)))*exp(-2*((x-xc2)/
w)**2) + (A3/(w*sqrt(3.1415927/2)))*exp(-2*((x-xc3)/
w)**2) + (A4/(w*sqrt(3.1415927/2)))*exp(-2*((x-xc4)/
w)**2) + (A5/(w*sqrt(3.1415927/2)))*exp(-2*((x-xc5)/
w)**2) + (A6/(w*sqrt(3.1415927/2)))*exp(-2*((x-xc6)/
w)**2) + (A7/(w*sqrt(3.1415927/2)))*exp(-2*((x-xc7)/
w)**2) + (A8/(w*sqrt(3.1415927/2)))*exp(-2*((x-xc8)/
w)**2) + (A9/(w*sqrt(3.1415927/2)))*exp(-2*((x-xc9)/
w)**2) + (A10/(w*sqrt(3.1415927/2)))*exp(-2*((x-xc10)/
w)**2);
```

Figure B.4: Block diagram used to fit 10 Gaussian function to the calibration spectrum.

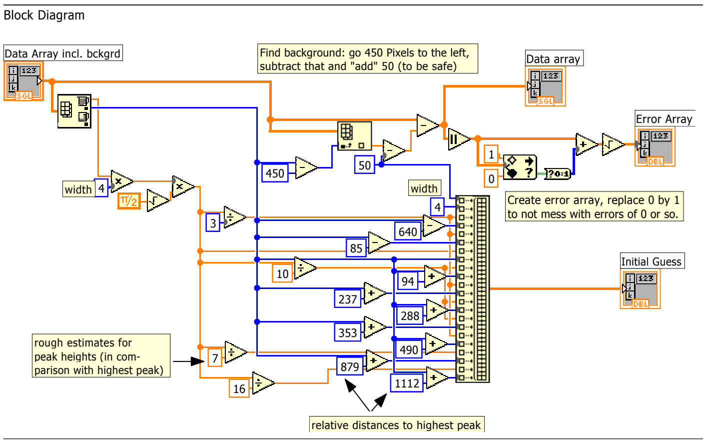

Find background: go 450 Pixels to the left, subtract that and "add" 50 (to be safe)

Create error array, replace 0 by 1 to not mess with errors of 0 or so.

rough estimates for peak heights (in comparison with highest peak)

relative distances to highest peak

Figure B.5: Block diagram used for the offset, width, amplitude and peak positions guess values, for the calibration spectrum fitting.

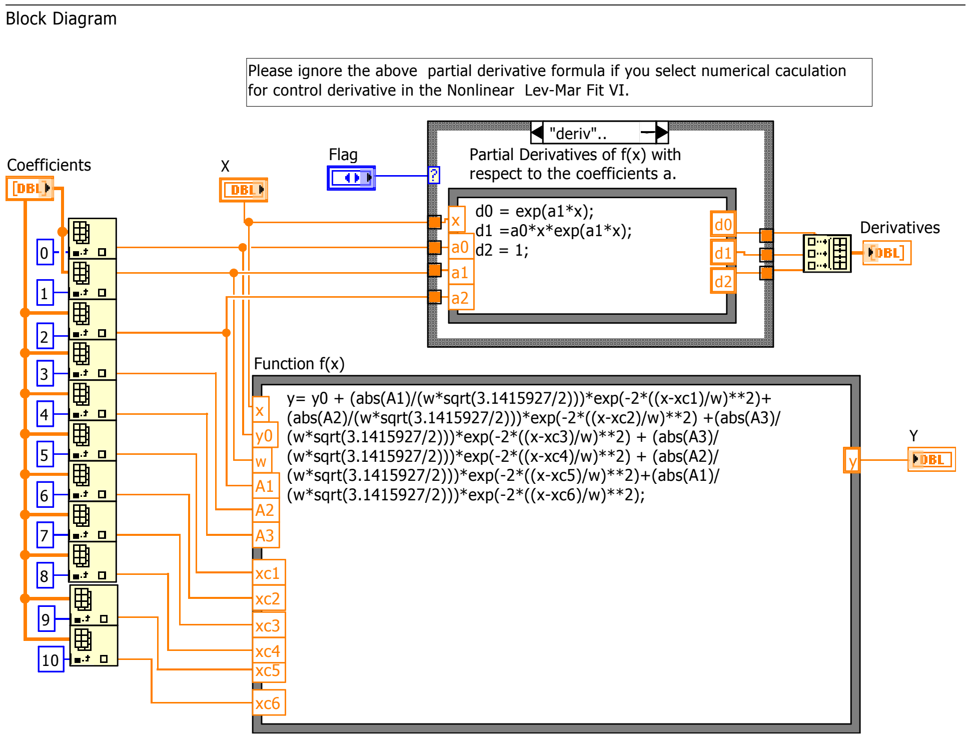

Please ignore the above partial derivative formula if you select numerical caculation for control derivative in the Nonlinear Lev-Mar Fit VI.

Partial Derivatives of f(x) with respect to the coefficients a.

```
d0 = exp(a1*x);
d1 =a0*x*exp(a1*x);
d2 = 1;
```

```
y= y0 + (abs(A1)/(w*sqrt(3.1415927/2)))*exp(-2*((x-xc1)/w)**2)+
(abs(A2)/(w*sqrt(3.1415927/2)))*exp(-2*((x-xc2)/w)**2) +(abs(A3)/
(w*sqrt(3.1415927/2)))*exp(-2*((x-xc3)/w)**2) + (abs(A3)/
(w*sqrt(3.1415927/2)))*exp(-2*((x-xc4)/w)**2) + (abs(A2)/
(w*sqrt(3.1415927/2)))*exp(-2*((x-xc5)/w)**2)+(abs(A1)/
(w*sqrt(3.1415927/2)))*exp(-2*((x-xc6)/w)**2);
```

Figure B.6: Block diagram used to fit 6 Gaussian function to the ion spectrum.

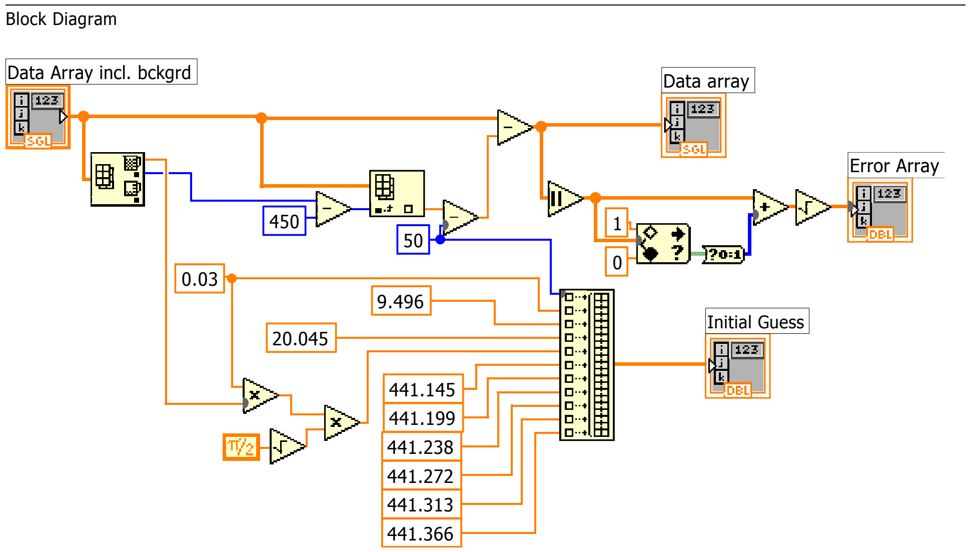

Figure B.7: Block diagram used for the offset, width, amplitude and peak positions guess values, for the ion spectrum fitting.

Bibliography

[BAC50] Breit G., Arfken G. B. and Clendenin W. W.: Spectroscopic isotope shift and nuclear polarization. *Phys. Rev.* **78**, 390 (1950).

[BB97] Bouchiat M. A. and Bouchiat C.: Parity violation in atoms. *Rep. Prog. Phys.* **60**, 1351 (1997).

[BC52] Breit G. and Clendenin W. W.: Effect of intrinsic moment of electron on spectroscopic isotope shift. *Phys. Rev.* **85**, 689 (1952).

[BDF03] Berengut J. C., Dzuba V. A. and Flambaum V. V.: Isotope-shift calculations for atoms with one valence electron. *Phys. Rev. A* **68**, 022502 (2003).

[BFF 97] Biedermann C., Förster A., Füss Mann G. and Radtke R.: First results from the Berlin EBIT. *Phys. Scr. T* **73**, 360 (1997).

[BGH 98] Beutelspacher M., Grieser M., v. Hahn R., Repnow R., Schwalm D., Wissler G. and Wolf A.: Electron cooling experiments at the Heidelberg heavy ion storage ring TSR. *Proc. EPAC* (1998).

[BL55] Brueckner K. A. and Levinson C. A.: Approximate reduction of the many-body problem for strongly interacting particles to a problem of self-consistent fields. *Phys. Rev.* **97**, 1344 (1955).

[BOD 96] Beiersdorfer P., Osterheld A. L., Declaux V. and Widmann K.: Observation of lifetime-limited x-ray linewidths in cold highly charged ions. *Phys. Rev. Lett.* **27**, 5353 (1996).

[Bow36] Bowen I. S.: Forbidden lines. *Rev. Mod. Phys.* **8**, 55 (1936).

[Bra67] Brandow B. H.: Linked-cluster expansions for the nuclear many-body problem. *Rev. Mod. Phys.* **39**, 771 (1967).

[Bre29] Breit G.: The effect of retardation of the interaction of two electrons. *Phys. Rev.* **34**, 553 (1929).

[Bri45] Brillouin L.: A theorem of Larmor and its importance for electrons in magnetic fields. *Phys. Rev.* **67**, 260 (1945).

[Bru55] Brueckner K. A.: Many-body problem for strongly interacting particles. II. Linked cluster expansion. *Phys. Rev.* **100**, 36 (1955).

[Bru05] Bruhns H.: *High precision x-ray spectroscopy on highly charged argon ions*, Ruprecht-Karls-Universität Heidelberg, (2005).

[BS57] Bethe H. A. and Salpeter E. E.: *Quantum mechanics of one- and two-electrons atoms.* New York : Plenum Publishing Corporation (1957).

[BS03] Beyer H. F. and Shevelko V. P.: *Itroduction to the physics of highly charged ions.* Bristol and Philadelphia : Institute of Physics Publishing (2003).

[BSB 02] Banaś D., Stöhlker Th., Beyer H. F., Bosch F., Bräuning-Demian A., Gumberidze A., Hagmann S., C.Kozhuharov, Ma X., Mokler P. H., Mann R., Orsic Muthing A., Sierpowski D., Spillmann U., Tachenov S., Stachura Z. and Warczak A.: Exclusive production of the n=2 S-states in He-like uranium. *GSI Scientific Report* (2002).

[BW36] Breit G. and Wigner E.: Capture of slow neutrons. *Phys. Rev.* **49**, 519 (1936).

[BW99] Bennett S. C. and Wieman C. E.: Measurements of the 6S → 7S transition polarizability in atomic Cesium and an improved test of the standard model. *Phys. Rev. Lett.* **82**, 2484 (1999).

[CAI 96] Currell F. J., Asada J., Ishii K., Minoh A., Motohashi K., Nakamura N., Nishizawa K., Ohtani S., Okazaki K., Sakurai M., Shiraishi H., Tsurubuchi S. and Watanabe H.: A new versatile Electron-Beam Ion Trap. *J. Phys. Soc. Jpn.* **65**, 3186 (1996).

[CBM 04] Caron M., Bombardier F., Merle E., Noël Ch., Pierret O., Rosol R. and Vermare C.: Comparison of 2 cathode geometries for high current (2KA) diodes. *Proc. of LINAC* (2004).

[CLFM01] Charro E., Lopez-Ferrero S. and Martin I.: Forbidden emission coefficients for intraconfiguration transitions $^2P_{3/2}$-$^2P_{1/2}$ along the boron sequence. *J. Phys. B: At. Mol. Phys.* **34**, 4243 (2001).

[CS59] Condon E. U. and Shortley G.: *The theory of atomic spectra.* Cambridge : Cambridge Univ. Pr. (1959).

[DCD 03] Draganić I., Crespo López-Urrutia J. R., DuBois R., Fritzsche S., Shabaev V. M., Soria Orts R., Tupitsyn I. I., Zou Y. and Ullrich J.: High precision wavelength measurements of QED-sensitive forbidden transitions in highly charged argon ions. *Phys. Rev. Lett.* **91**, 183001 (2003).

[DDD 02] Donets E. D., Donets D. E., Donets E. E., Salnikov V. V., Shutov V. B. and *et all*: Status report on studies of EBIS in the string mode of operation. *Rev. Sci. Instrum.* **73**, 679 (2002).

[Des75] Desclaux J. P.: A multiconfiguration relativistic Dirac-Fock program. *Comput. Phys. Commun.* **21**, 207 (1975).

[Doy69] Doyle H. T.: *Advances in Atomic and Molecular Physics.* New York : Academic (1969).

[Edl55] Edlén B.: On the identification of Ca XIV and A XIV in the solar corona. *Mon. Not. Roy. Astron. Soc.* **114**, 700 (1955).

[Edl82] Edlén B.: Accurate values of the energy intervals in the configurations $1s^2 2s^2 2p^k$ (k=1-5). *Phys. Scr. T* **26**, 71 (1982).

[END 04] Ewald G., Nörtershäuser W., Dax A., Götte S., Kirchner R., Kluge H.-J., Hühl Th., Sanchez R., Wojtaszek A., Bushaw B. A., Drake G. W., Yan Z.-C. and Zimmermann C.: Nuclear charge radii of ^{8,9}Li determined by laser spectroscopy. *Phys. Rev. Lett.* **93**, 113001 (2004).

[Faw70] Fawcett B. C.: Clasification of highly ionized emission lines due to transitions from singly and doubly excited levels in sodium, magnesium, aluminium, silicon, phosphorous, sulphur and chlorine. *J. Phys. B: At. Mol. Phys.* **3**, 1152 (1970).

[FBH 95] Fricke G., Bernhardt C., Heilig K., Schaller L. A., Schellenberg L., Shera E. B. and de Jager C. W.: Nuclear ground state charge radii from electromagnetic interactions. *At. Data Nucl. Data Tables* **60**, 177 (1995).

[FGP 66] Fawcett B. C., Gabriel A. H., Peacock F. E. and Saunders P. A. H.: Extreme ultra-violet spectra from laser-produced plasmas. *Proc. Phys. Soc.* **88**, 1051 (1966).

[FH55] Fock K. W. and Hill D. L.: The distribution of charge in the nucleus. *Ann. Rev. Nuclear Sci.* **5**, 25 (1955).

[FJW61] Fawcett B. C., Jones B. B. and Wilson R.: Vacuum ultra-violet spectra of multiply ionized inert gases. *Proc. Phys. Soc.* **78**, 1223 (1961).

[FR53] Fitch V. L. and Rainwater J.: Studies of x-rays from mu-mesonic atoms. *Phys. Rev.* **92**, 789 (1953).

[FR76] Fullerton L. W. and Rinker G. A.: Accurate and efficient methods for evaluation of vacuum-polarization potentials of order $Z\alpha$ and $Z\alpha^2$. *Phys. Rev. A* **13**, 1283 (1976).

[FS83] Fischer C. F. and Saha H. P.: Multiconfiguration Hartree-Fock results with Breit-Pauli corrections for forbidden transitions in the $2p^4$ configuration. *Phys. Rev. A* **28**, 3169 (1983).

[GGR 03] Gwinner G., Grieser M., Repnow R., Saathoff G., Schwalm D., Wolf A., Müller A., Schippers S., Zavodszky P. A., Gorczyca T. W., Zatsarinny O. and Gu M. F.: Dielectronic recombination of Fe XXI and Fe XXII via n=2 → n'=2 core excitations. *Ap. J. S.* **147**, 421 (2003).

[Gil97] Gillaspy J. D.: First results from the EBIT at NIST. *Phys. Scr. T* **71**, 99 (1997).

[Gil01] Gillaspy J.: *Trapping highly charged ions: fundamentals and applications.* New York : Nova Science Publishers, Inc. (2001).

[GMN 80] Grant I. P., McKenzie B., Norrington P., Mayers D. and Pyper N.: An atomic multiconfigurational Dirac-Fock package. *Comput. Phys. Commun.* **21**, 207 (1980).

[GMP76] Grant I. P., Mayers D. and Pyper N.: Studies in multiconfiguration Dirac-Fock theory I. The low-lying spectrum of Hf III. *J. Phys. B: At. Mol. Phys.* **9**, 2777 (1976).

[Gol57] Goldstone J.: Derivation of the Brueckner many-body theory. *Proc. R. Soc. A* **239**, 267 (1957).

[Gon05] González Martínez A. J.: *Quantum interference in the dielectronic recombination of heavy highly charged ions*, Ruprecht-Karls-Universität Heidelberg, (2005).

[Gra61] Grant I. P.: Relativistic self-consistent fields. *Proc. R. Soc. A* **262**, 555 (1961).

[Gra70] Grant I. P.: Relativistic calculation of atomic structure. *Adv. Phys.* **19**, 747 (1970).

[Gri97] Griem H. R.: *Principle of Plasma Spectroscopy.* New York : Cambridge University Press (1997).

[GvR03] Grieser M., von Hahn R. and Repnow R.: The MPI-K accelarators. *Progress Report* (2003).

[Har34] Hartree D. R.: Approximate wave functions and atomic field for mercury. *Phys. Rev.* **46**, 738 (1934).

[HE30] Hughes D. S. and Eckart C.: The effect of the motion of the nucleus on the spectra of Li I and Li II. *Phys. Rev.* **36**, 694 (1930).

[Her58] Herrmann G.: Optical theory of thermal velocity effects in cylindrical electrons beams. *J. Appl. Phys.* **29**, 127 (1958).

[HFM53] Hofstadter R., Fechter H. R. and McIntyre J. A.: High-energy electron scattering and nuclear structure determinations. *Phys. Rev.* **92**, 978 (1953).

[Hin76] Hinnov E.: Highly ionized atoms in tokamak discharges. *Phys. Rev. A* **14**, 1533 (1976).

[JBS88a] Johnson W. R., Blundell S. A. and Sapirstein J.: Many-body perturbation theory calculations of energy levels along the lithium isoelectronic sequence. *Phys. Rev. A* **37**, 2764 (1988).

[JBS88b] Johnson W. R., Blundell S. A. and Sapirstein J.: Many-body perturbation theory calculations of energy levels along the sodium isoelectronic sequence. *Phys. Rev. A* **38**, 2699 (1988).

[JLQ 60] Jahoda F. C., Little E. M., Quinn W. E., Sawyer G. A. and Stratton T. F.: Continuum radiation in the X-ray and visible regions from a magnetically compressed plasma (Scylla). *Phys. Rev.* **119**, 843 (1960).

[JS85] Johnson W. R. and Soff G.: The Lamb shift in hydrogen-like atoms, $1 \leq Z \leq 100$. *At. Data Nucl. Data Tables* **33**, 405 (1985).

[JW57] Jenkins F. A. and White H. E.: *Fundamentals of Optics.* New York : McGraw-Hill Book Company (1957).

[JW81] Jenkins F. and White H.: *Fundamentals of Optics.* New York : McGraw-Hill (1981).

[KCO99] Kinugawa T., Currell F. J. and Ohtani S.: Pulsed eavporative cooling for trapped highly charged ions. *J. Phys. Soc. Jpn.* **65**, 3186 (1999).

[KF48] Kusch P. and Foley H. M.: The magnetic moment of the electron. *Phys. Rev.* **74**, 250 (1948).

[KHJ 92] Kristensen M., Hangst J. S., Jessen P. S., Nielsen J. S., Poulsen O. and Shi P.: Laser-rf double-resonance spectroscopy in a storage ring. *Phys. Rev. A* **46**, 4100 (1992).

[Kim97] Kim Y. K.: Strengths and weaknesses of relativistic atomic structure. *Phys. Scr. T* **73**, 19 (1997).

[KP32] Kemble E. C. and Present R. D.: On the breakdown of the Coulomb law for the Hydrogen atom. *Phys. Rev.* **44**, 1031 (1932).

[KSM 97] Kollmus H., Schmitt W., Moshammer R., Unverzagt M. and Ullrich J.: A high resolution 4π multi-electron spectrometer for soft electrons. *Nucl. Instrum. and Methods B* **124**, 377 (1997).

[Lin85] Lindgren I.: Accurate many-body calculations on the lowest ^{2}S and ^{2}P states of the lithium atom. *Phys. Rev. A* **31**, 1273 (1985).

[LJC 05] Lapierre A., Jentschura U. D., Crespo López-Urrutia J. R., Braun J., Brenner G., Bruhns H., Fischer D., Gónzalez Martínez A. J., Harman Z., Johnson W. R., Keitel C. H., Mironov V., Osborne C., Sikler G., Soria Orts R., Tawara H., Tupitsyn I. I., Ullrich J. and Volotka A.: Relativistic electron correlation, quantum electrodynamics and the lifetime of the $1s^22s^22p\ ^2P^0_{3/2}$ level in Boronlike argon. *Phys. Rev. Lett.* **95**, 183001 (2005).

[LMH 88] Levine M. A., Marrs R. E., Henderson J. R., Knapp D. A. and Schneider M. B.: The electron beam ion trap: A new instrument for atomicphysics measurements. *Phys. Scr. T* **22**, 157 (1988).

[Low37] Lowen I. S.: The effect of nuclear motion in the Dirac equation. *Phys. Rev.* **51**, 190 (1937).

[LR47] Lamb W. E. and Retherford R. C.: Fine structure of the hydrogen atom by a microwave method. *Phys. Rev.* **72**, 241 (1947).

[LWW80] Langenberg A., Watson R. L. and White J. R.: Foil excited K x-ray transitions in few-electron sulphur ions. *J. Phys. B: At. Mol. Phys.* **13**, 4193 (1980).

[Lyo39] Lyot M. B.: A study of the solar corona and prominences without eclipses. *MNRAS* **99**, 580 (1939).

[MEK94] Marrs R. E., Elliott S. R. and Knapp D. A.: Production and trapping of hydrogenlike and bare uranium ions in an Electron Beam Ion Trap. *Phys. Rev. Lett.* **72**, 4082 (1994).

[MFR 01] Modugno G., Ferrari G., Roati G., Brecha R. J., Simoni A. and Inguscio M.: Bose-Einstein condensation of potassium atoms by sympathetic cooling. *Science.* **294**, 1320 (2001).

[MLK 88] Marrs R. E., Levine M. A., Knapp D. A. and Henderson J. R.: Measurement of electron-impact-excitation cross section for very highly charged ions. *Phys. Rev. Lett.* **60**, 1715 (1988).

[Moh75] Mohr P. J.: Lamb shift in a strong Coulomb potential. *Phys. Rev. Lett.* **34**, 1050 (1975).

[MPS98] Mohr P. J., Plunin G. and Soff G.: QED correction in heavy atoms. *Phys. Rep.* **293**, 227 (1998).

[MSB 01] Ma X., Stöhlker Th., Bosch F., Brinzanescu O., Fritzsche S., Kozhuharov C., Ludziejewski T., Mokler P. H., Stachura Z. and Warczak A.: State-selective electron capture into He-like U^{90+} ions in collisions with gaseous targets. *Phys. Rev. A* **64**, 012704 (2001).

[NLP 96] Nefiodov A. V., Labzowsky L. N., Plunien G. and Soff G.: Nuclear polarization effects in spectra of multicharged ions. *Phys. Lett. A* **222**, 227 (1996).

[Opp30] Oppenheimer J. R.: Note on the theory of the interaction of field and matter. *Phys. Rev.* **35**, 461 (1930).

[Opp31] Oppenheimer J. R.: Note on light quanta and the electromagnetic field. *Phys. Rev.* **38**, 725 (1931).

[Opp35] Oppenheimer J. R.: Note on charge and field fluctuations. *Phys. Rev.* **47**, 144 (1935).

[Opt05] *http://www.optometrics.com/prod/spectra/gratings* (2005).

[Pac94] Pachucki K.: Complete two-loop binding correction to the Lamb shift. *Phys. Rev. Lett.* **72**, 3154 (1994).

[Pas38] Pasternack S.: Note in the fine structure of Hα and Dα. *Phys. Rev.* **54**, 1113 (1938).

[PB12] Paschen F. and Back E.: Normale und anomale Zeemaneffekte. *Ann. Physik* **39**, 897 (1912).

[PBD 91] Penetrante B. M., Bardsley J. N., DeWitt D., Clark M. and Schneider D.: Evolution of ion-charge-state distributions in an electron-beam ion trap. *Phys. Rev. A* **43**, 4861 (1991).

[PG30] Pauling L. C. and Goudsmit S.: *The structure of line spectra.* New York : McGraw-Hill (1930).

[PG95] Pachucki K. and Grotch H.: Pure recoil corrections to hydrogen energy levels. *Phys. Rev. A* **51**, 1854 (1995).

[Phi49] Phillips M.: The effect of the nuclear motion on atomic magnetic moments. *Phys. Rev.* **76**, 1803 (1949).

[PMG 89] Plunien G., Müller B., Greiner W. and Soff G.: Nuclear polarization contribution to the Lamb shift in heavy atoms. *Phys. Rev. A* **39**, 5428 (1989).

[Pry64] Pryce M. H. L.: the origin of coronal emission lines. *Astrophys. J.* **140**, 1192 (1964).

[PTF92] Parpia F. A., Tong M. and Fischer C. F.: Relativistic calculations of nuclear motion effects in many-electron atoms. *Phys. Rev. A* **46**, 3717 (1992).

[PWH94] Pachucki K., Weitz M. and Hänsch T. W.: Theory of the hydrogen-deuterium isotope shift. *Phys. Rev. A* **49**, 2255 (1994).

[Sal52] Salpeter E. E.: Mass corrections to the fine structure of hydrogen-like atoms. *Phys. Rev.* **87**, 328 (1952).

[Sal98] Salzmann D.: *Atomic Physics in Hot Plasmas.* New York : Oxford University Press (1998).

[SBH 63] Sawyer G. A., Bearden A. J., Henins I., Jahoda F. C. and Ribe F. L.: X-ray spectroscopy of a theta-pinch plasma in the region 15-25 Å. *Phys. Rev. Lett.* **131**, 1891 (1963).

[Sch48] Schwinger J.: On quantum-electrodynamics and the magnetic moment of the electron. *Phys. Rev.* **73**, 416 (1948).

[Sch49] Schwinger J.: Quantum electrodynamics. II. Vacuum polarization and self-energy. *Phys. Rev.* **75**, 651 (1949).

[Sha85] Shabaev V. M.: Mass corrections in a strong nuclear field. *Theor. Math. Phys.* **63**, 588 (1985).

[SJS96a] Safronova M. S., Johnson W. R. and Safronova U. I.: Realtivistic many-body calculations of the energies of $n = 2$ states for the berylliumlike isoelectronic sequence. *Phys. Rev. A* **53**, 4036 (1996).

[SJS96b] Safronova M. S., Johnson W. R. and Safronova U. I.: Realtivistic many-body calculations of the energies of $n = 2$ states for the boronlike ions. *Phys. Rev. A* **54**, 2850 (1996).

[Sla29] Slater J. C.: The theory of complex spectra. *Phys. Rev.* **34**, 1293 (1929).

[SM68] Shore B. W. and Menzel D. H.: *Principles of Atomic Spectra.* New York : John Wiley and Sons (1968).

[SVM 94] Silver J. D., Varney A. J., Margolis H. S., Baird P. E. G., Grant I. P., Groves P. D., Hallett W. A., Handford A. T., Hirst P. J., Holmes A. R., Howie D. J. H., Hunt R. A., Nobbs K. A., Roberts M., Studholme W., Wark J. S. and Williams M. T.: The Oxford electron-beam ion trap: A device for spectroscopy of highly charged ions. *Rev. Sci. Inst.* **65**, 1072 (1994).

[Swi35] Swirles B.: The relativistic self-consistent field. *Proc. R. Soc. A* **152**, 625 (1935).

[TBB 01] Träbert E., Beiersdorfer P., Brown G. V., Chen H., Thorn D. B. and Biémont E.: Experimental M1 transition rates in highly charged Kr ions. *Phys. Rev. A* **64**, 04251 (2001).

[TSC 03] Tupitsyn I. I., Shabaev V. M., Crespo López-Urrutia J. R., Draganić I., Soria Orts R. and Ullrich J.: Relativistic calculations of isotope shifts in highly charged ions. *Phys. Rev. A* **68**, 022511 (2003).

[UBC 99] Utter S. B., Beiersdorfer P., Crespo López-Urrutia J. R. and Widmann K.: Position and size of the electron beam in the high-energy electron beam ion trap. *Nucl. Instrum. and Methods A* **428**, 276 (1999).

[Ueh35] Uehling E. A.: Polarization effects in the positron theory. *Phys. Rev.* **48**, 55 (1935).

[UMD 03] Ullrich J., Moshammer R., Dörner R., Schmidt L. Ph. H. and Schmidt-Böcking H.: Recoil-ion and electron momentum spectroscopy: Reaction-Microscope. *Rep. Prog. Phys.* **66**, 1463 (2003).

[Uni05] University Stockholm: *Private communication* (2005).

[Wei39] Weisskopf V. F.: On the self-energy and the electromagnetic field of the electron. *Phys. Rev.* **56**, 72 (1939).

[Wel48] Welton T. A.: Some observable effects of the quantum-mechanical fluctuations of the electromagnetic field. *Phys. Rev.* **74**, 1157 (1948).

[WG34] Williams R. C. and Gibbs R. C.: Fine-structure analysis of $H^1\alpha$ and $H^2\alpha$. *Phys. Rev.* **45**, 475 (1934).

[WHF53] Wilets L., Hill D. L. and Ford K. W.: Isotope shift anomalies and nuclear structure. *Phys. Rev.* **91**, 1488 (1953).

[WHK 95] Weits M., Huber A., Kaler F. S., Leibfried D., Vassen W., Zimmermann C., Pachucki K., Haensch T. W., Julien L. and Biraben F.: Precision measurement of the $1S$ ground-state Lamb shift in atomic hydrogen and deuterium by frequency comparison. *Phys. Rev. A* **52**, 2664 (1995).

[Wid98] Widmann K.: *High resolution spectroscopic diagnostics of very high-temperature plasmas in the hard x-ray regime.*, Technische Universität Graz, (1998).

[Wil40] Williams A. O.: A relativistic self-consistent field for Cu^+. *Phys. Rev.* **58**, 723 (1940).

[Woo35] Wood R. W.: Anomalous diffraction gratings. *Phys. Rev.* **48**, 928 (1935).

[Xie98] Xie Z. Q.: Production of highly charged ion beams from electron cyclotron resonance ion sources (invited). *Rev. Sci. Inst.* **69**, 625 (1998).

[Zee97] Zeeman P.: On the influence of magnetism on the nature of the light emitted by a substance. *Phil. Mag.* **43**, 226 (1897).

[ZSW 04] Zimmermann B., Schartner K.H., Wilhelmi O., Kammer S., Liebel H., Ehresmann A. and Schmoranzer H.: Experimental high resolution study of the photoproduction of Ne^+ 3p satellites in the threshold energy range. *J. Phys. B: At. Mol. Phys.* **37**, 511 (2004).